Institute for Research in Fundamental Science
Institute for Studies in Theoretical Physics and Mathematics (IPM)

School of Particles and Accelerators

Ph.D. Thesis

Stabilization Strategies for Drift Tube Linacs

By: Mohammad Reza Khalvati

Supervisors:
Dr. Suitbert Ramberger
Prof. Mohammad Lamehi Rashti

June 2016

To my parents,
for their endless love, support and encouragement.

To my wife, Adeleh,
who has been a constant source of support and encouragement
during the challenges of studying and life.

Acknowledgements

Special mention goes to my enthusiastic supervisors, Suitbert Ramberger and Mohammad Lamehi Rashti. My PhD has been an amazing experience with them and I appreciate their tremendous academic support, guidance and encouragement. Their advice on both research as well as on my career have been invaluable.
Similar, profound gratitude goes to Maurizio Vretenar, Frank Gerigk, Hessameddin Arfaei, Yves Cuvet, Jean-Michel Giguet and Giovanni De Michele for their kind support, comment and what I learned from their experience. I would like to extend thanks to IPM and CERN for providing me the opportunity of working on Linac4 project.

Abstract

The average axial electric fields in drift tube linac cavities are known to be sensitive with respect to the perturbation errors. Postcoupler is a powerful stabilizer devices that is used to reduce this sensitivity of average axial field. Postcouplers are the cylindrical rod which is extended from cavity wall toward the drift tube without touching the drift tube surface. Postcouplers need to be adjusted to the right length to stabilize the average axial field. Although postcouplers are used successfully in many projects, there is no straightforward procedure for postcouplers adjustment and it has been done almost based on trial and errors. In this thesis, the physics and characteristics of postcouplers has been studied by using an equivalent circuit model and 3D finite element method calculations. Finally, a straightforward and accurate method to adjust postcouplers has been concluded. The method has been verified by using experimental measurements on CERN Linac4 drift tube linac cavities.

Keyword: Drift tube linacs, Stabilization of average axial field, Postcouplers, Equivalent circuit models, Linac4

Contents

List of Figures

List of Tables

Chapter 1

Linear accelerators

Particle accelerators are powerful tools with a wide range of applications, including fundamental research in particle physics, medical applications and industrial applications. The European Organization for Nuclear Research (CERN) is one of the largest physics laboratory in the world. In this laboratory, physicists use the energetic particle beam for different research experiments.

The accelerator complex at CERN is a succession of particle accelerators that accelerate charged particles to the higher energy. Each accelerator boosts the energy of a beam of particles, before injecting the beam into the next stage of acceleration in the sequence. A Linear accelerator is the first stage of proton acceleration in the CERN complex. This linac is called Linac2. Linac2 inject 50 MeV proton beam to a circular accelerator called the Proton-Synchrotron Booster (PSB). The Linac4 is the current project of CERN for replacing Linac2. Linac4 is composed of an ion source, a Radio Frequency Quadrupole (RFQ), an Alvarez Drift Tube Linac (DTL), a Cell-Coupled Drift Tube Linac (CCDTL) and a Pi-Mode structure (PIMS).

This chapter provides a short review of the proton accelerators. The history of CERN and different sections of this scientific center is also reviewed.

1.1 Brief history of linear accelerators

The idea of linear acceleration of charged particles was proposed in an article by G. Ising in 1924. In this article, he suggested a method to accelerate ions using a pulsed voltage between gaps of two drift tubes (Fig 1.1). Ising proposed to generate the pulsed voltage by capacitor discharges. He could not make this accelerator at that time due to the limitation in the fabrication of the electronic device that he needed to extract pulsed voltage for this experiment [1].

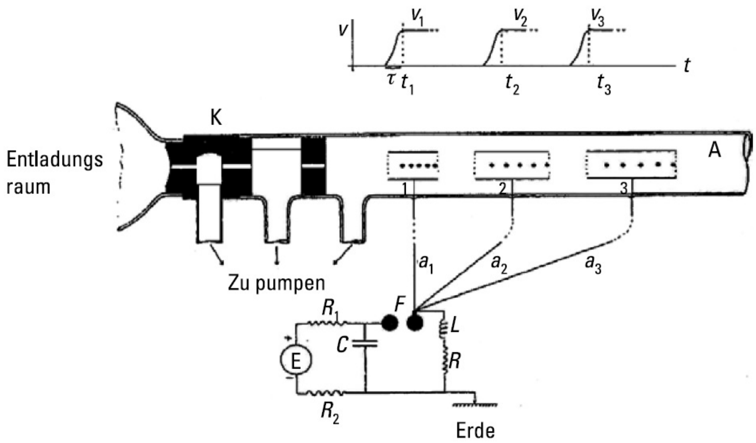

Figure 1.1: The proposal of Ising for a linear particle accelerator. The high-frequency field is supplied by a discharge across the electrods.

In 1928, Wideroe proposed a new strategy to accelerate charged particles along a series of drift tubes. In this method, he suggested producing an alternating electric field between drift tubes by applying an alternating voltage to every second drift tube. The drift tube length increases with particle velocity, such that particles always experience an accelerating field when passing through the gaps. Wideroe built a machine with a single drift tube to test the validity of his principle using an alternating voltage of 25 kV between two grounded electrodes. Using this machine, he could accelerate Na and K ions to 50 keV.

Sloan and Lawrence at Berkeley proposed to test the Wideroe method on a large device. The alternating voltage of 42 kV with the frequency of 10 MHz was applied to a sequence of 30 drift tubes. They could accelerate mercury up to 1.25 MeV. Later in 1934, by upgrading the structure with 36 drift tubes and using a voltage of 79 kV, they could achieve 2.8 MeV. A schematic view of the structure of Sloan-Lawrence is shown in Fig. 1.2.

In the mid-thirties, it was not possible to accelerate electrons and protons using Wideroe structures. The Wideroe structure which is needed to accelerate protons, to an energy of about 1.25 MeV, would have been too long. There were not any oscillator which produces enough power between gaps of such long structure, at that time. In consequence, the method was not practical for proton acceleration and cyclotrons were more efficient [2].

The first idea that led to linear proton acceleration from 4 MeV to 32 MeV was proposed by Luis Alvarez (Fig. 1.3). The initial 4 MeV beam was injected from a Van de Graaff accelerator. The tank was 12.2 meter long and radius of 1 meter. The total

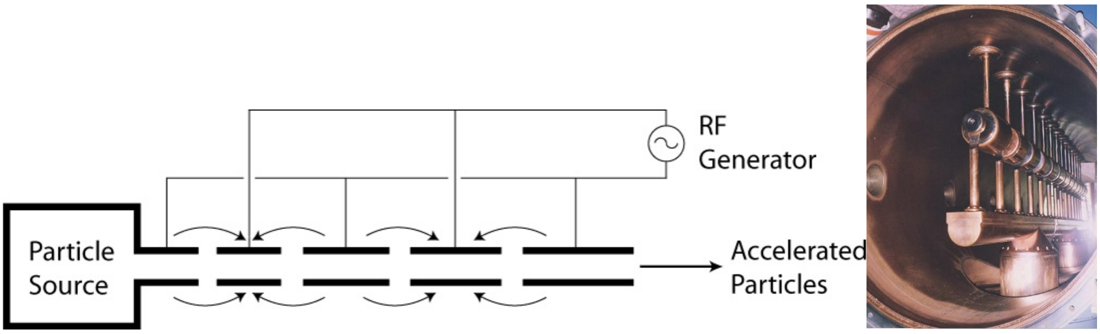

Figure 1.2: Left: A schematic view of Sloan-Lawrence. Right: The Sloan-Lawrence structure at Berkeley national laboratory.

46 drift tubes were installed in the Tank. The manufacturing this accelerator was started at 1945 and took just two years until the first beam was accelerated. Before this achievement, particle acceleration was accomplished by a series of separated cavities, but the major problem was the considerable power loss on the two end walls of each cavity. Alvarez solved the problem of power loss by putting a bunch of drift tubes inside a big and long cavity. The whole structure is called Alvarez structure or DTL. For this cavity, the power was supplied by nine high-power oscillators fed from a pulse generator of the artificial transmission line type [2].

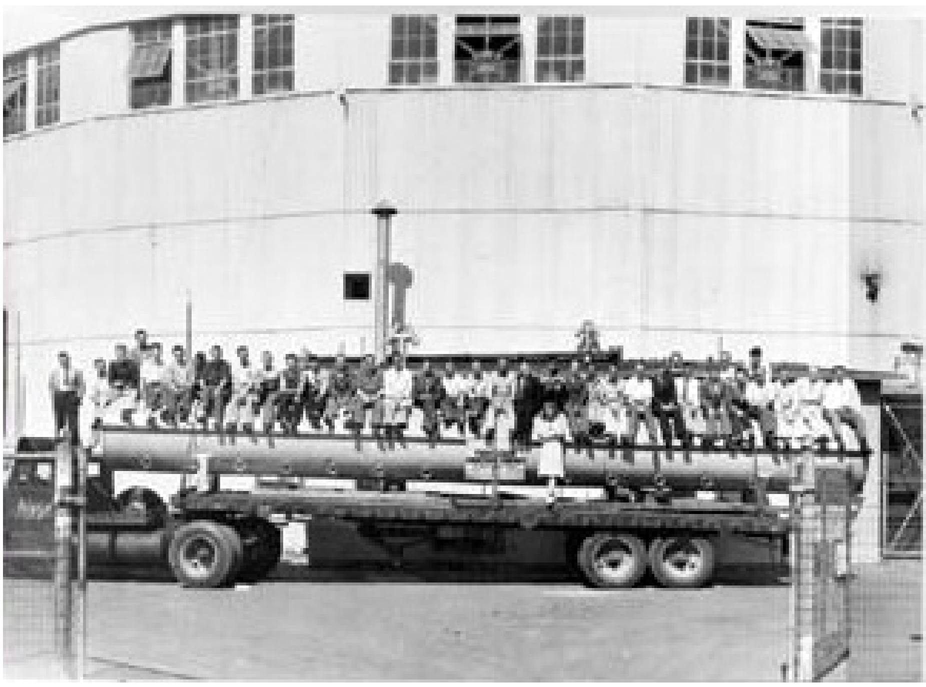

Figure 1.3: The first DTL tank with all of the people connected with the building of the accelerator, the secretaries and everybody on the tank as it came into Berkeley.

The second attempt to accelerate protons using a DTL was made at the University of Minnesota in 1953. This machine was very similar to the first one except it accelerated a proton beam from 500 keV to 68 MeV. The Bevatron injector was the third one which was a 20 MeV Alvarez structure. During the second half of the 1950's, two other machines were built simultaneously. The first one was built at Brookhaven (50 MeV AGS Injector). The other one was the injector of the proton synchrotron at CERN [3].

After these successful experiences in proton acceleration using DTLs, the particular attention has been focused on the manufacturing of DTLs in modern proton acceleration. Nowadays, DTLs are used for acceleration of the charged particle beam in the velocity range of $0.05< \beta <0.4$ [4].

1.2 The CERN accelerator complex

The first official proposal of creating a European atomic physics laboratory had been presented at the European Cultural Conference on 9 December 1949. In June of 1950, the American physicist, Isidor Rabi had presented the proposal to the member states of the United Nations Educational, Scientific and Cultural Organization (UNESCO) at a meeting in Florence, Italy. In December 1951, the first resolution concerning the establishment of CERN was adopted and in two months, the agreement was signed by 11 countries. Geneva was selected as the place of CERN's laboratories in the next session of the CERN council on June of 1952 [5].

Five years later, the first 600 MeV Synchrocyclotron (SC) was built and it provided beams for CERN's first experiments in particle and nuclear physics (Fig. 1.4). In 1967, it started supplying beams for a dedicated unstable-ion facility called Isotope Separator on Line (ISOLDE), which carried out research ranging from pure nuclear physics to astrophysics and medical physics [6].

In the next accelerating stage, a Proton Synchrotron (PS) could accelerate the proton beam up to 28 GeV [7]. Because of this achievement, the PS became host to CERN's particle physics program and provided beams for experiments. In 1965, an article of CERN [8], reported one of the first observation of anti-deuteron and it answered to many fundamental questions in nuclear physics.

In 1968, Georges Charpak reported his revolutionary invention of multi-wire gas particle detector which led to detect particles thousand times faster than ordinary detectors of that time (Bubble chamber). This patent was awarded by Nobel prize in physics in 1993 [9].

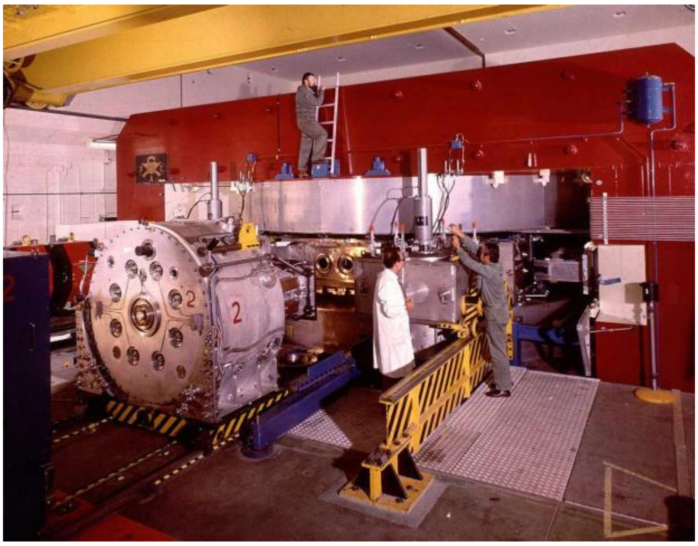

Figure 1.4: The 600 MeV Synchrocyclotron accelerator machine at CERN.

The physicists knew that a huge gain in collision energy would be released from colliding particle beams head on, rather than by using a single beam and a stationary target. This idea leads to construction of the world's first proton-antiproton collider, called Intersecting Storage Rings (ISR) [10]. The ISR produced proton-antiproton collisions on 4 April 1981 which led to the discovery of the field particles W and Z boson (communicators of weak interaction). The Nobel prize was dedicated to Simon van der Meer and Carlo Rubbia for this discovery [11, 12]. The ISR proved to be an excellent instrument for particle physics. Finally, the ISR was closed on 1984.

After the ISR, the Super Proton Synchrotron (SPS) was the first of CERN's giant underground rings which was built with seven kilometers in circumference. It was also the first accelerator to cross the France-Swiss border(Fig. 1.5). The construction of this ring was started in 1971 and a 450 GeV proton beam was produced by this ring five years later [13].

With the recent discovery of the weak neutral interaction and the intermediate bosons, CERN has led the field of elementary particle physics to the next step, the large electron-positron collider (LEP) operating at the laboratory since 1989 [14]. The initial energy of the collider was chosen to be around 91 GeV so that Z bosons could be produced. Observing the creation and decay of the short-lived Z boson was a critical test of the Standard Model of elementary particles. Although the W and Z were discovered with the ISR, the construction of LEP had the advantage that particles would be produced in collisions far cleaner than those obtained with protons and antiprotons. In consequence, it is possible to measure the mass of Z and W more precisely than ISR [14]. In the seven years that LEP operated at around 100 GeV, it produced around 17 million Z particles. LEP was upgraded in 1995 with as many as 288 superconducting accelerating cavities added to double the energy so that the collisions could produce pairs of W bosons. Finally, LEP was closed down on 2nd of November 2000 to make way for the construction of the Large Hadron Collider in the same tunnel [15].

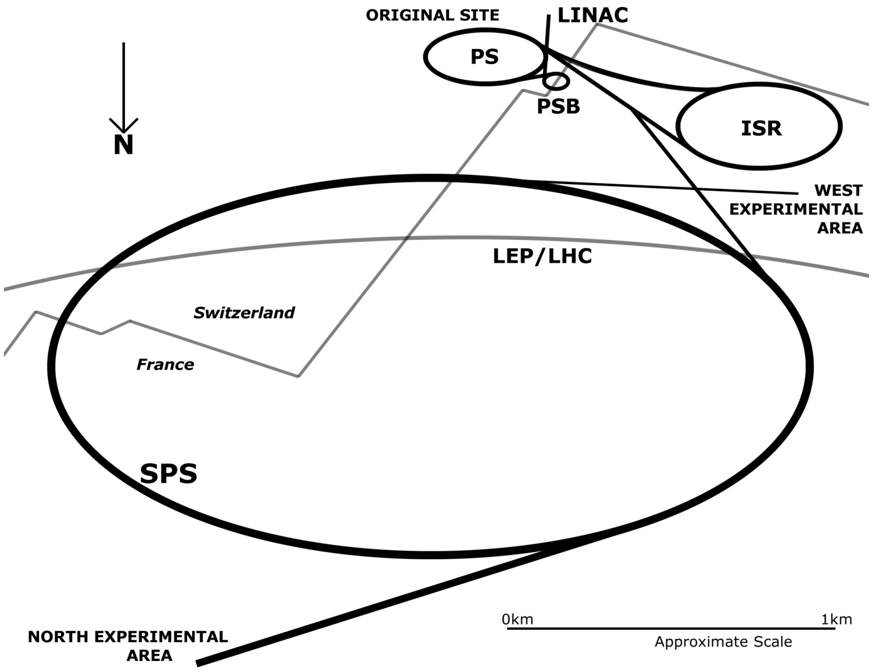

Figure 1.5: A layout of CERN's facilities at 1965. As is seen, the SPS is the first CERN's accelerator which is cross the France-Swiss border.

The Large Hadron Collider (LHC) is the world's largest and most powerful particle accelerator (Fig. 1.6). It first started up on 10 September 2008 and remains the latest addition to CERNs accelerator complex. The LHC is a 27-kilometer ring of superconducting magnets. Inside the accelerator, two high-energy proton beams travel at close to the speed of light before they are made to collide. The proton and anti-proton beams move in opposite directions in separate beam pipes. These pipes are kept at ultrahigh vacuum. The beams of these two pipes are made to collide at four locations around the accelerator ring, corresponding to the positions of four particle detectors: ATLAS, CMS, ALICE and LHCb. A schematic diagram of the CERN complex accelerator, considering the recent upgrades [16], is shown in Fig. 1.7.

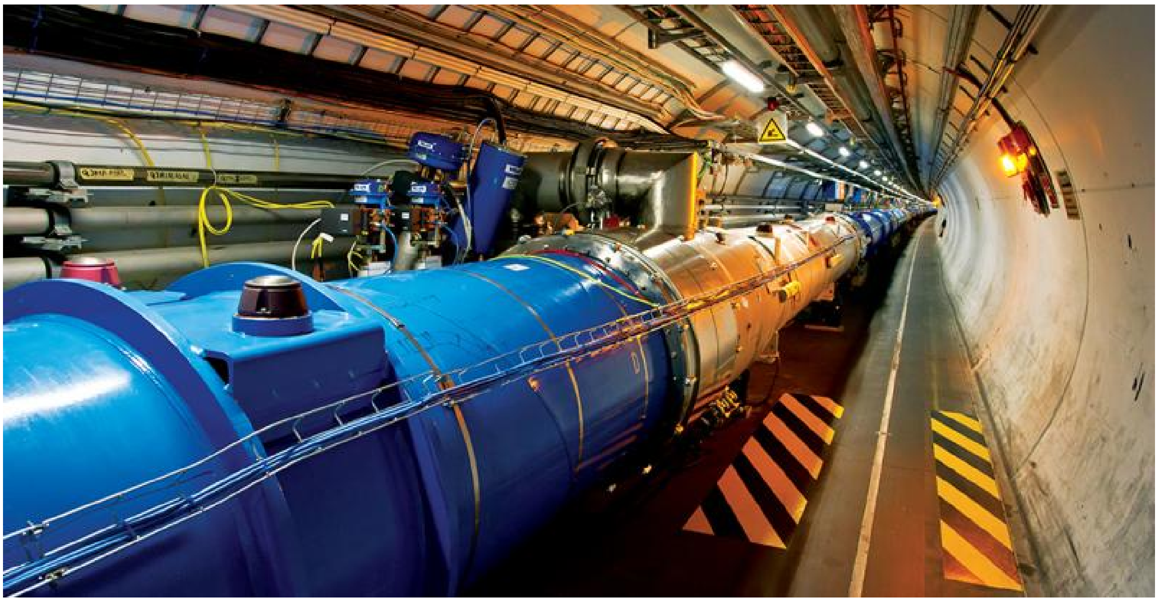

Figure 1.6: The LHC tunnel.

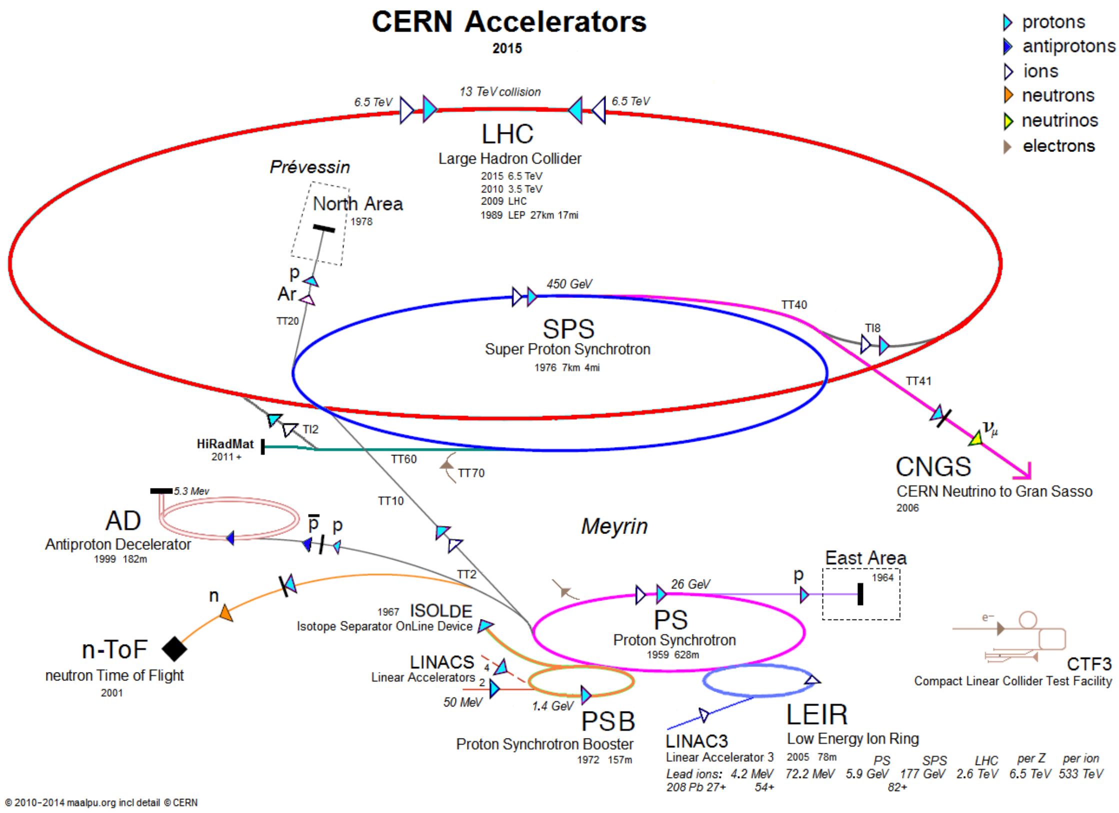

Figure 1.7: A layout of accelerator complex at CERN.

1.3 Linear accelerators at CERN

Historically at CERN, the pioneering 50 MeV Linac1 started operation in 1959, injecting a beam of a few milliamperes into the PS. Soon after commissioning, several hardware upgrades were accomplished in mid of the seventies because of demand for increasing of the linac current, which resulted in the current of 50 mA.

In the next commissioning in 1972, a limit of Linac1 current leads to replace the Linac1 with a modern one called Linac2. In the beginning, Linac2 was designed to accelerate a 150 mA proton beam up to 50 MeV. During the next upgrade of Linac2, this output current was even further increased, up to 180 mA, in 1993, by replacement of 750 keV radio-frequency quadrupole (RFQ). Important vacuum leaks have been progressively appearing on the large 202 MHz accelerating DTL tanks of Linac2, requiring important repair interventions during the shutdown periods and being a constant cause of concern for future operation [17]. Moreover, the RF tubes used in the Linac2 RF system will go out of production because of their obsolete design, dating back to the times of Linac1. The consequence is that to keep Linac2 running, CERN had to decide between buying and stocking a large amount of RF tubes or rebuilding the RF system with more modern devices [17]. In addition, the Linac2 was designed around 40 years ago and the accelerator technology has been significantly developed during this time. One of these important improvements is to accelerate H^- ions-beam in Linac and charge-exchange of H^- ions using a stripping foil. This allows accumulating protons in booster without blowing up the emittance. The possibility of using higher frequencies was the other improvement of linac which leads to compact accelerating structures with higher efficiency. These improvements are mostly due to the huge improvement of modern simulation codes and by a better understanding of halo formation phenomena, a particular concern in high space-charge systems like linear accelerators. Because of these considerations and advantages of using a modern injector, CERN had decided to develop its modern and up-to-date H^- injector called Linac4.

1.4 Upgrade to Linac4

In elementary particle physics experiments, the energy of particles which collide with each other is an important parameter. Besides the energy of particles, the number of useful events at the place of interaction is also of important(Fig. 1.8). Increasing the event number is particularly important when rare events with a small production cross section σ_p are studied. The quantity that measures the ability of a particle accelerator to produce the required number of interactions is called the luminosity. The luminosity is the proportionality factor between the number of events per second dR/dt and the cross-section σ_p

$$\frac{dR}{dt} = \mathcal{L} \cdot \sigma_p \tag{1.1}$$

The unit of the luminosity is therefore $\mathrm{m}^{-2}\mathrm{s}^{-1}$.

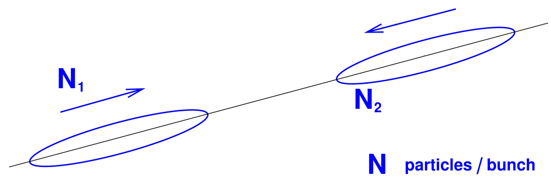

Figure 1.8: A schematic plot of two beams collision. By increasing the number of particles per transverse cross-section of each bunch, the rate of collision increases.

It is possible to generate more events using higher luminosity colliders. For a bunch of total N_b charged particles and with transverse cross-section area of A working at frequency of f_{rev} and n_b bunches per revolution, the luminosity is defined as

$$\mathcal{L} \propto \frac{n_b f_{rev} N_b^2}{A(\epsilon_x^*, \epsilon_y^*)}. \tag{1.2}$$

Here, the beam cross-section is a function of normalized emittance i.e., ϵ_x^* and ϵ_y^*. The N_b and emittance are the only parameters in this formula that can be regulated and the other parameters are fixed [18].

The demand for higher beam intensity mentioned earlier. The move to a more robust and modern proton injector, lead to start a new program which is known as Linac4. The goal of this upgrade is to increase the current LHC luminosity. Therefore, the plan is to increase the number of particles per bunch up to 1.7×10^{11} [19]. In addition, such a modern injector has other advantages, for instance, long-term reliability, a modern and powerful control system and easier maintenance.

The Linac4 is a normal conducting linear accelerator which accelerates H^- ions up to 160 MeV. Although the Linac4 provides beam to the PS booster at the beginning of its operation, it is the preliminary part of a 50-GeV injector. Linac4 is supposed to operate in different stages. In the first stage, Linac4 will operate with low duty cycle of 0.1% as an injector to the PSB. In the second stage, Linac4 will be the front-end for a Low-Power Superconducting Proton Linac (LP-SPL) with a modest duty cycle. The LP-SPL is followed by a new Proton Synchrotron (PS2) to accelerate H^- ions up to 50 GeV. In the third stage, it is foreseen to operate with a high duty cycle for a High-Power version of the SPL (HP-SPL) [20, 21]. The architecture of the old and new injection structures are shown in Fig. 1.9.

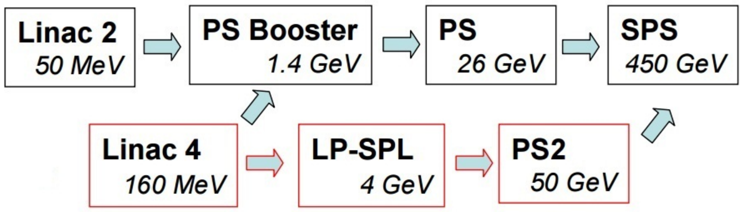

Figure 1.9: The architecture of the old and new injection system of CERN accelerator complex. In preliminary stage, Linac4 provide beam for PS booster but in the future plans, it is part of a longer Linac which accelerates proton up to the 50 GeV.

A model of Linac4 building is shown in Fig. 1.10. The accelerator is supposed to settle in a 12 m deep underground tunnel and tunnel ends to the Linac2-PSB line. In the ground floor of this building, the klystrons and other equipment are installed. The Linac4 RF system configuration is shown in Fig. 1.11. Also, the general parameters of Linac4 are listed in table 1.1 [17]. In the following, each of these structures is introduced briefly.

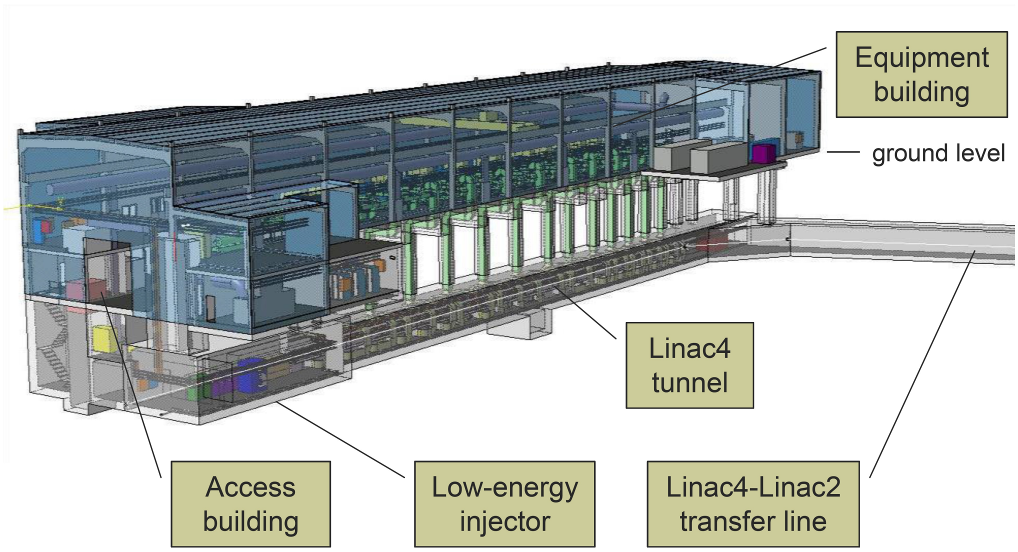

Figure 1.10: A layout of Linac4 building. The klystrons and other equipment are installed on the ground floor and accelerating structure are installed in a tunnel 12 m underground.

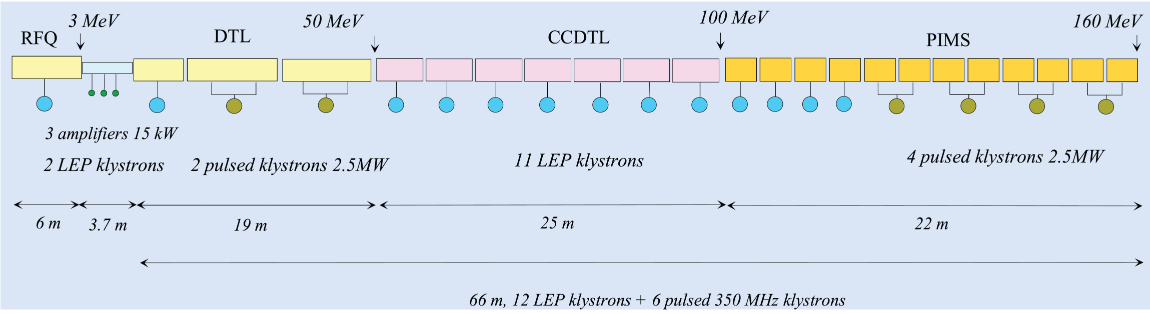

Figure 1.11: Linac4 RF system configuration.

Parameter	Value
Ion species	H^-
Output energy	160 MeV
Bunch frequency	352.2 MHz
Overall linac length	76.33 m
Source current (during pulse)	80 mA
Linac current (average during pulse)	40 mA
No. particles per pulse	1.00×10^{14}
No. particles per bunch	1.14×10^{9}

Table 1.1: The Linac4 output beam parameters.

1.4.1 Ion source

The ion source is the first part of the linac which provides H^- ions beam of 45 keV and maximum beam current of 80 mA for the linac. The ion source is built in collaboration with DESY [22].

1.4.2 The low energy beam transport

The Low Energy Beam Transport (LEBT) is the second part of Linac4. The LEBT is vital to control the current and emittance delivered to the next stage of acceleration. The LEBT is a 1.8 m structure consisting two solenoids, two steerers, a Beam-Current-Transformer (BCT) and a special diagnostics vessel. In the diagnostic vessel, the beam parameters are measured using various equipment such as a Faraday cup, a profile monitor and a movable iris device. A pre-chopper is installed in the machine to cut away the rising and falling edge of the beam. Two solenoids are used to focus and to match the beam to the RFQ. Steerers are foreseen to optimize transmission in the presence of alignment errors [23].

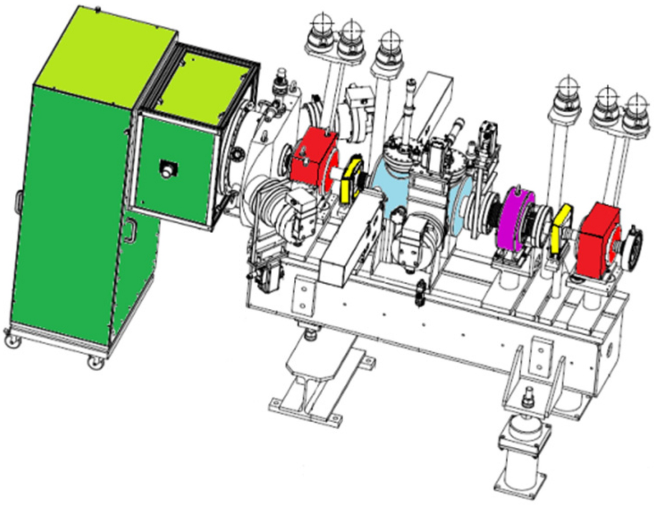

Figure 1.12: Sketch of the LEBT. In this scheme the solenoids (red), steerers (yellow), BCT (purple) and diagnostic tank (blue) are shown.

1.4.3 Radio frequency quadruple

After the LEBT, 45 keV beam is delivered to a 3 meter long RFQ and accelerated up to 3 MeV (Fig. 1.13) [24]. The RFQ is an ion accelerator in which both acceleration and transverse focusing are performed by RF fields. The other advantage of the RFQ is that it can combine the functions of acceleration and bunching.

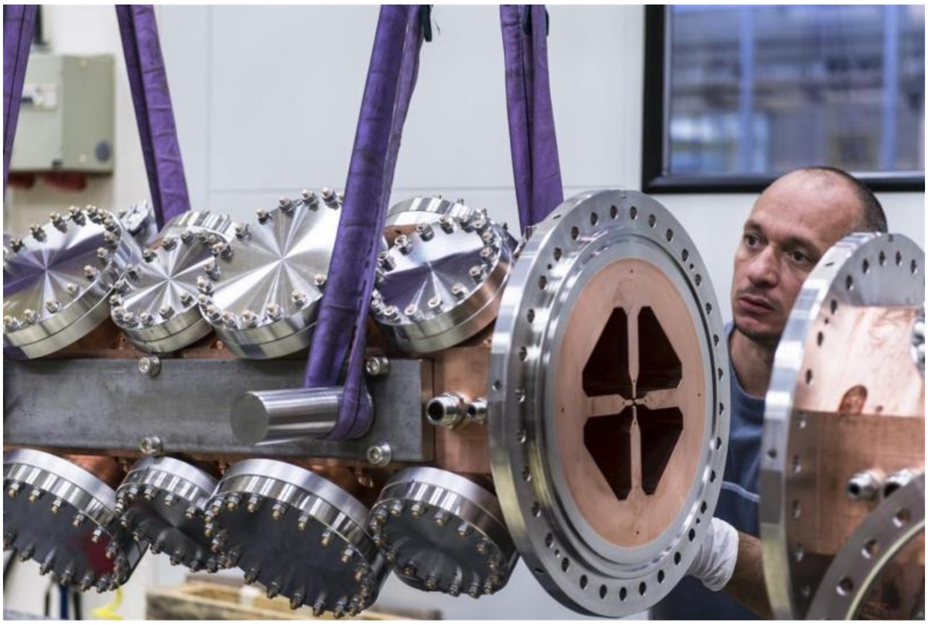

Figure 1.13: The CERN's Linac4 RFQ installation at accelerator test-stand.

1.4.4 Drift tube linac

After the RFQ, the 3 MeV beam is accelerated by using 3 DTL cavities. The H^- ion-beam is accelerated up to 11.88 MeV in DTL Tank1. Then, the output beam of the Tank1 is directed to the DTL Tank2 and is accelerated up to 31.45 MeV. Finally the beam is accelerated up to 50.27 MeV by using DTL Tank3. A typical DTL structure is shown in Fig. 1.14.

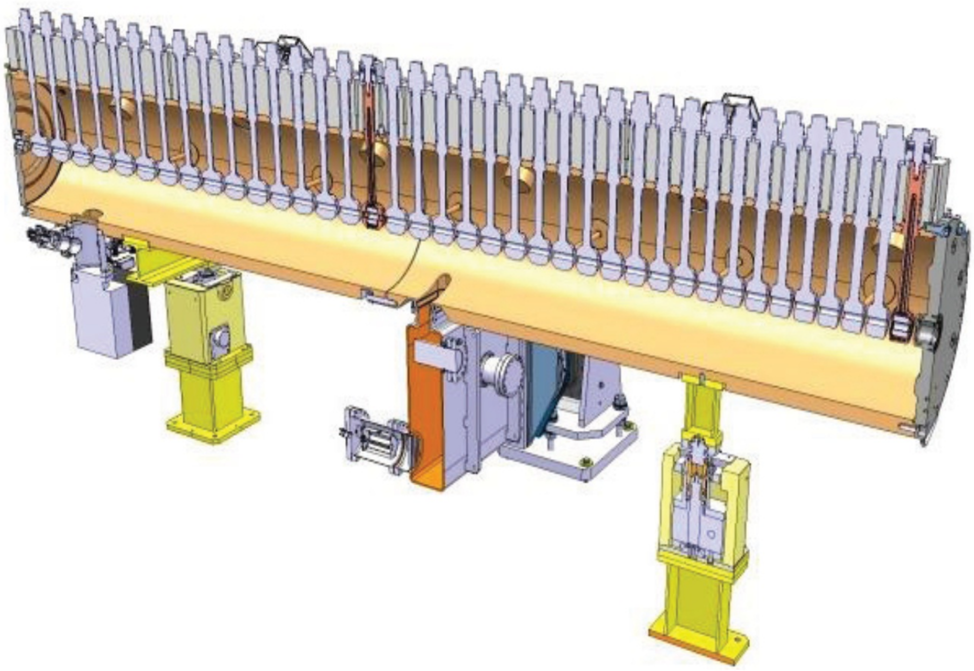

Figure 1.14: A cross-section view of CERN's Linac4 DTL Tank1.

1.4.5 Cell-coupled drift tube linac

The Cell-coupled drift tube linac (CCDTL) is developed at Los Alamos National Laboratory (LANL) for two reason: providing high shunt impedance and good field stability for particle velocities $0.1 < \beta < 0.5$. The CCDTL is the fourth structure in the chain of Linac4 normal conducting structures. The Linac4 CCDTL operates at 352.2 MHz and the beam of 50 MeV is accelerated to the 102 MeV. In Linac4 CCDTL consists of 7 modules and each module is made of three short DTL-type tanks (Fig. 1.15) [25].

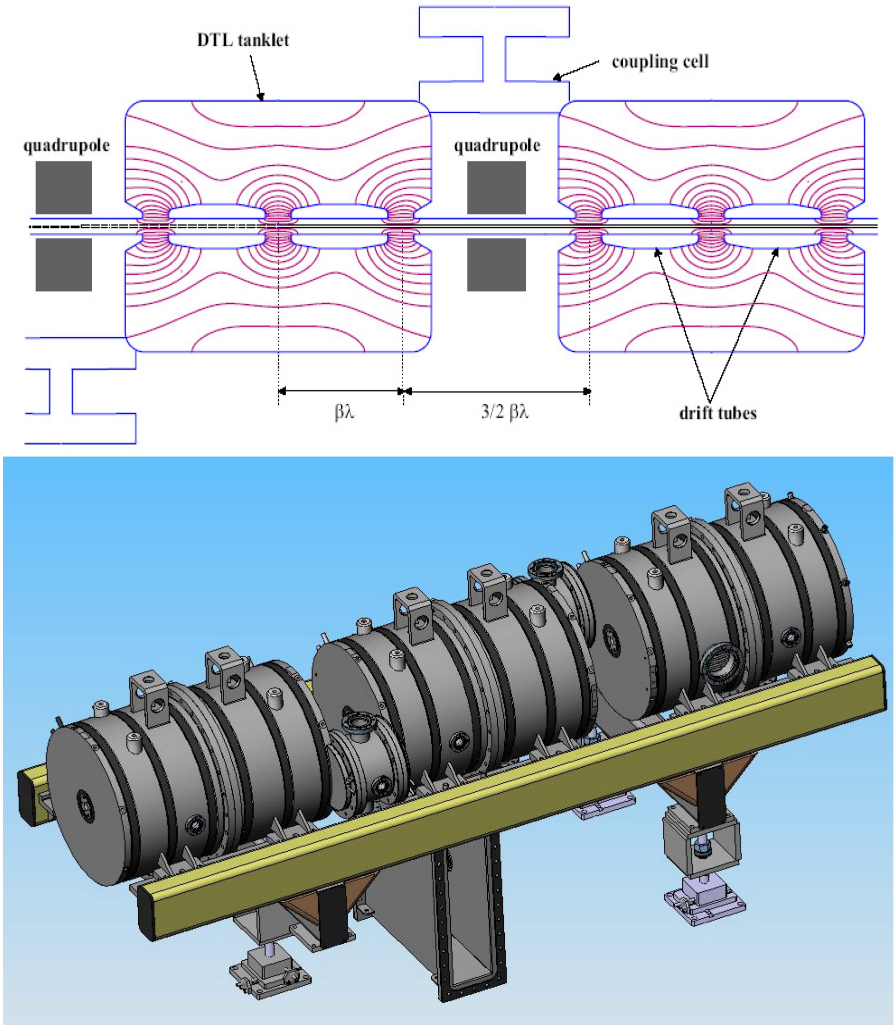

Figure 1.15: The CERN Linac4 CCDTL.

1.4.6 Pi-mode structure

The PIMS is the last accelerating structure which is used to accelerate 102 MeV H^- ion-beams to 160 MeV. The PIMS is made of a sequence of 12 seven-cell accelerating cavities, resonating at 352.2 MHz (Fig. 1.16). The cell length is the same within a cavity but changes from one cavity to the other according to the beam velocity. The advantage of PIMS compared to the other structures in this range of energy is simple construction and tuning [26,27]. The parameters of CERN Linac4 DTL, CCDTL and PIMS are listed in table 1.2.

Figure 1.16: Left: Discs and rings before welding. Right: CERN's Linac4 hot prototype of PIMS

	DTL	CCDTL	PIMS
Frequency (MHz)	352.2	352.2	352.2
$E_{in/out}$ (MeV)	3-50.3	50.3-102.9	102.9-160
$N_{cavities}$	3	21	12
$N_{cavities/module}$	-	3	-
$N_{gaps/cavity}$	39/42/30	3	7
Cavity length (m)	3.9/7.3/7.3	0.7-1.04	1.3-1.54

Table 1.2: The parameters of the CERN Linac4 DTL, CCDTL and PIMS.

Chapter 2

Drift tube linac cavities

It has been discussed that the H^- ion-beams are accelerated by using RF cavities. In CERN Linac4 linear accelerator, the DTL is one of the accelerating structure. In this chapter, the fundamental of charged particle acceleration in RF cavities and special case of Alvarez DTL structure will be reviewed.

2.1 Fundamentals of RF cavities

Classical electrodynamics is the foundation for the principles of charged particle acceleration and it will be reviewed briefly in the following. Let us assume a particle of charge q, associated with the position, velocity and particle mass of $\overrightarrow{R}$, $\overrightarrow{v}$ and m. Therefore, the mechanical momentum is given by $\overrightarrow{P} = m\gamma\overrightarrow{v}$. γ is the Lorentz factor

$$\gamma = \left(1 - \frac{|\overrightarrow{v}|^2}{c_0^2}\right)^{-1/2}, \tag{2.1}$$

where c_0 is the speed of light. The kinetic energy of particle is

$$T = mc_0^2(\gamma - 1), \tag{2.2}$$

The particle motion can be written using Lorentz equation

$$\overrightarrow{F} = \frac{d\overrightarrow{P}}{dt} = q(\overrightarrow{E} + \overrightarrow{v} \times \overrightarrow{B}), \tag{2.3}$$

where $\overrightarrow{E}$ is the electric field in the unit of Vm^{-1} and $\overrightarrow{B}$ is the magnetic induction or flux density in unit of T. According to equation 2.3, the effect of magnetic fields is more appreciable as particle velocity increases. By introducing the permittivity of vacuum ϵ_0 and permeability of vacuum μ_0, the electric displacement is $\overrightarrow{D} = \epsilon_0\overrightarrow{E}$ and the magnetic field is $\overrightarrow{H} = \overrightarrow{B}/\mu_0$, these fields are governed by Maxwell's equations

$$\nabla \cdot \overrightarrow{D} = \rho, \tag{2.4}$$

$$\nabla \cdot \overrightarrow{B} = 0, \tag{2.5}$$

$$\nabla \times \overrightarrow{E} = -\frac{\partial \overrightarrow{B}}{\partial t}, \tag{2.6}$$

$$\nabla \times \overrightarrow{H} = \frac{\partial \overrightarrow{D}}{\partial t} + \overrightarrow{J}, \tag{2.7}$$

where $\overrightarrow{J}$ and ρ are the external current density and external charge density respectively. The energy density is

$$u = \frac{1}{2}\left(\epsilon_0|\overrightarrow{E}|^2 + \mu_0|\overrightarrow{H}|^2\right). \tag{2.8}$$

According to Maxwell's equations, the electric and magnetic fields are coupled and it is not convenient to work with these equations. Hence, one can merge equations 2.6 and 2.7 yielding two equations that describe $\overrightarrow{E}$ and $\overrightarrow{B}$ independently. These equations are known as wave equation

$$\nabla^2 \overrightarrow{E} - \epsilon_0\mu_0 \frac{\partial^2}{\partial t^2}\overrightarrow{E} = 0, \tag{2.9}$$

$$\nabla^2 \overrightarrow{B} - \epsilon_0\mu_0 \frac{\partial^2}{\partial t^2}\overrightarrow{B} = 0. \tag{2.10}$$

2.1.1 Pillbox cavities

A possible case to accelerate charged particles is to use a pillbox cavity which is excited in a TM_{010}-mode. Let us assume a pillbox cavity of radius a and length of l (Fig. 2.1). The analytical calculation of the wave equation for the TM_{mnq} mode shows that the amplitude of electric and magnetic fields are given by

$$\begin{aligned}
E_z &= \frac{\nu_{mn}^2}{a^2} J_m(\frac{\nu_{mn}}{a} r) \cos\frac{\pi q z}{l} \cos m\phi, \\
E_r &= -\frac{a}{\nu_{mn}} J'_m(\frac{\nu_{mn}}{a} r) \sin\frac{\pi q z}{l} \cos m\phi, \\
E_\phi &= \frac{a^2}{\nu_{mn}^2} \frac{\pi q m}{l r} J_m(\frac{\nu_{mn}}{a} r) \sin\frac{\pi q z}{l} \sin m\phi, \\
H_z &= 0, \\
H_r &= -j \frac{a^2}{\nu_{mn}^2} \frac{mk}{Z_0 r} J'_m(\frac{\nu_{mn}}{a} r) \sin\frac{\pi q z}{l} \sin m\phi, \\
H_\phi &= -j \frac{a}{\nu_{mn}} \frac{k}{Z_0} J'_m(\frac{\nu_{mn}}{a} r) \cos\frac{\pi q z}{l} \cos m\phi, \\
k &= \frac{4\pi^2}{\lambda^2} = \sqrt{(\frac{\pi q}{l})^2 + (\frac{\nu_{mn}}{a})^2},
\end{aligned} \tag{2.11}$$

where ν_{mn} represent the n^{th} root of Bessel function of J, Z_0 is the free space wave impedance and λ is the free-space wavelength [28]. Using the equations 2.11, the excited electromagnetic field in a TM$_{010}$-mode are

$$\begin{aligned}
&E_z = \frac{\nu_{01}^2}{a^2} J_0(\frac{\nu_{01}}{a} r), \\
&H_\phi = -j\frac{1}{Z_0} J_1(\frac{\nu_{01}}{a} r), \\
&\lambda = \frac{2\pi}{\nu_{01}}, \quad \omega = c\frac{\nu_{01}}{a},
\end{aligned} \tag{2.12}$$

From the equation 2.19 the magnetic field is negligible around the axis. The electric field amplitude varies with time according to the equation $E = E_z(r)\cos(\omega t)$. For a charged particle with constant velocity of v, the total energy gain is

$$\Delta W = qE_z \int_{-l/2}^{+l/2} \cos(\omega \frac{z}{v}) dz = \frac{qE_z}{l} \frac{\sin(\theta/2)}{\theta/2} = qUT, \tag{2.13}$$

where $\theta = \omega l/v$, $U = E_z/l$ is the maximum voltage per length and $T = 2\sin(\theta/2)/\theta$ is the transient time factor. The transient time factor describes how much energy is gained by particle which is traveling in a time varying electric field amplitude. Since electric fields have a time dependency of $\cos(\omega t)$, the electric field direction changes every π/ω seconds.

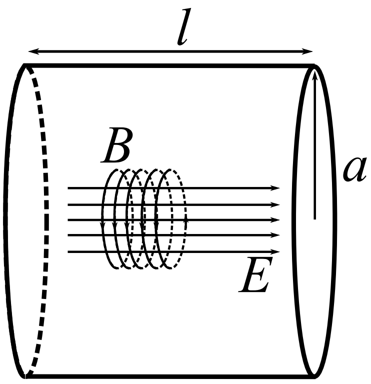

Figure 2.1: A simple pillbox cavity excited on TM$_{010}$. The electric field has only longitudinal component along the axis and is interesting for charged particle acceleration.

The quality factor (Q) is also another figure-of-merit of an accelerating cavity. The Q is defined as

$$Q = \omega \frac{\text{average stored energy}}{\text{energy loss/second}}. \tag{2.14}$$

The shunt impedance (R_{shunt}) is the other important parameters of an accelerating structure which describes the acceleration efficiency of a cavity,

$$R_{\text{shunt}} = \frac{V_{RF}^2}{2P_d}. \tag{2.15}$$

Where V_{RF} is the peak voltage across the cavity and P_d is the average power loss in the cavity walls. The power loss is obtained from

$$P_d = \int_s R_s |\overrightarrow{H}|^2 ds, \tag{2.16}$$

where R_s is the surface resistance, $R_s = \sqrt{\mu\omega/2\sigma}$, where σ is the material conductivity. For a given RF input power, the larger value of R_{shunt} means a higher V_{RF} across the gap. The ratio $[R_{\text{shunt}}/Q]$ is determined by the geometry of the cavity, regardless of the material or input power. It describes the relation between the total energy stored in the cavity and the energy distributed around the accelerating gap in the form of V_{RF}. The average axial electric field of an accelerating structure is defined as follows

$$E_0 = \frac{\int_l E_z(z)dz}{l}. \tag{2.17}$$

So far, the electromagnetic field in a simple pillbox cavity was studied. Particles should enter inside of cavity by means of a beam-port as is shown in Fig. 2.2. Cutting the port causes electric field lines to extend into the beam-port, and develop transverse components. This reduces the integrated longitudinal field, and therefore $[\mathrm{R_{shunt}/Q}]$ is reduced. A practical solution to compensate this reduction is to define "nose cones" or "Drift tubes" to concentrate field inside the cavity and reduce the cavity diameter to compensate the frequency shift caused by DT.

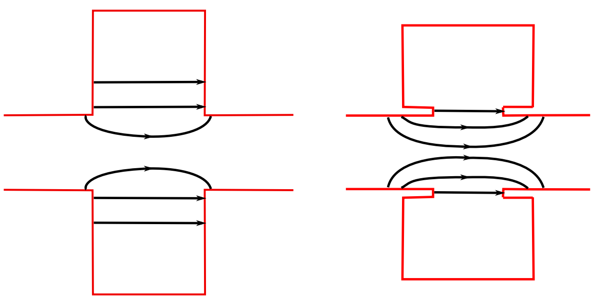

Figure 2.2: Left: A pill-box cavity with a beam port. Right: Introducing drift tube in cavity to increase the shunt impedance.

Let us assume a cavity with two half DTs as depicted in Fig. 2.3. If the inner radius of drift tube and the gap distance l_1 get smaller, then the cavity can be considered as a coaxial cable. The capacitance of the gap can be approximated by a two plates capacitor formula, i.e. $C_g = \epsilon_0 \pi a^2/l_1$. The inductance of a simple coaxial cable is equal to $L_c = (\mu_0/2\pi) l_2 \ln(b/a)$. In consequence one can approximate the cavity resonance frequency by $\omega = (L_c C_g)^{-1/2}$ and the $[R_{\text{shunt}}/Q]$ is

$$\left[\frac{R_{\text{shunt}}}{Q}\right] = \frac{V_{RF}^2}{U\omega} \approx \frac{2}{\omega C_g}. \tag{2.18}$$

Subsituting C_g and ω in to the equation 2.18 yields

$$\frac{R_{\text{shunt}}}{T^2 Q} = 2\pi\eta_0 \sqrt{\frac{l_1 l_2}{2a^2} \ln\left(\frac{b}{a}\right)}. \tag{2.19}$$

where $\eta_0 = 120\pi$ [29]. Although this is a rough approximation but it gives a good understanding of different parameters involved in an RF cavity design.

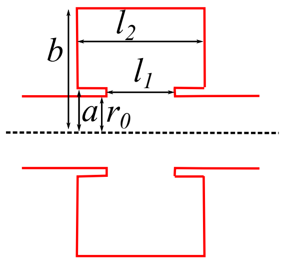

Figure 2.3: Different parameters of a single accelerating cavity with drift tubes.

Nowadays the $[\mathrm{R}_{\text{shunt}}/\mathrm{Q}]$ or ω of cavities are calculated by the simulation means. POISSON/SUPERFISH is one of the simulation packages to simulate the static magnetic and electric fields and radio-frequency electromagnetic fields in either 2-D Cartesian coordinates or axially symmetric cylindrical coordinates. The original version of POISSON/SUPERFISH was written in the early 1970s by R. F. Holsinger from the theory developed by Klaus Halbach. The program solves the Maxwell equations using Finite-Element method (FEM) and to do this, it generates triangular meshes fitted to the boundaries of different materials in the problem geometry [30].

In Fig. 2.4, the simulated electric field and the resonance frequency of a simple cavity with two drift tubes is shown. As is discussed, it is possible to approximate different parameters of such a cavity using the coaxial approximation. The calculated value of this cavity for two different gaps length of 2.5 and 5 mm is listed in table 2.1. The calculated and simulated resonance frequency are 4% and 7% different for gap lengths of 2.5 and 5 mm , respectively.

Gap (mm)	2.5	5
Simulated frequency (MHz)	95	130
Calculated frequency (MHz)	99	140
Calculated capacitance (nF)	0.09	0.045
Calculated inductance (nH)	28.60	28.60
Simulated [$R_{\text{shunt}}/(QTT)$]	43.19	57.08
Calculated [$R_{\text{shunt}}/(QTT)$]	35.63	50.39

Table 2.1: Comparison of simulated and approximated results of a single accelerating cell (Fig. 2.4).

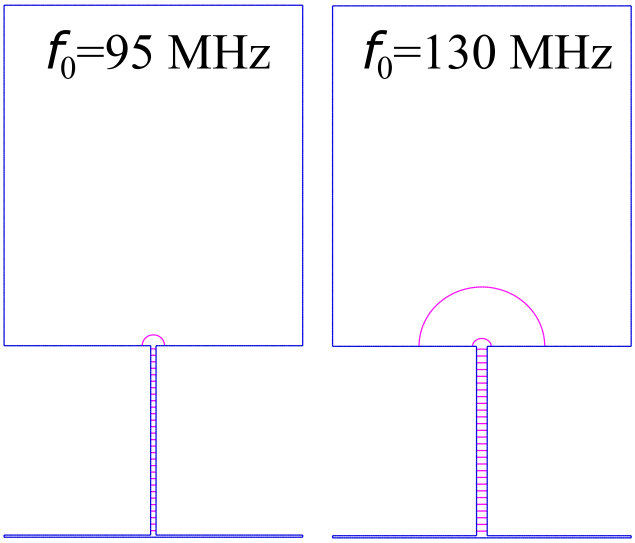

Figure 2.4: The simulated electric fields in a simple accelerating cell.

2.2 Alvarez Drift tube linac

In the first step, the DTL is designed cell by cell. The geometry of a typical half cell is shown in Fig. 2.5. In order to optimize this unit cell, several parameters are taken into the account. First of all, the geometry of the drift tube is chosen so that it can accommodate quadrupole magnets. Then the gap length and the drift tube shape are optimized in order to maximize the [R_{shunt}/Q] and to keep the Kilpatrick factor within reasonable limits. Finally, the overall geometry is adjusted in order to maximize the quality factor, while re-tuning the cavity to the nominal resonant frequency. Note that the aperture radius has a strong influence on the shunt impedance but its choice is usually dictated by beam dynamics considerations and in Linac4 a constant ratio between the beam pipe and the RMS beam size of 7 was kept throughout the whole linac [31].

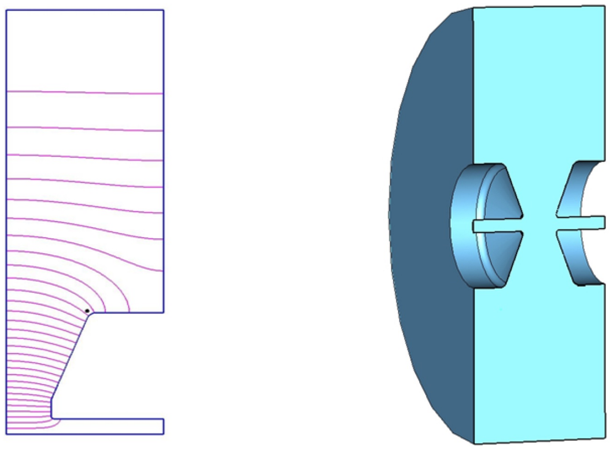

Figure 2.5: Left: A cross section of a half DTL's cell with axial symmetric. Right: An equatorial view of a 3D DTL cell.

After optimizing of single cells, the entire structure is assembled by putting these individual cells together and the wall between cells are removed. All cells are excited in the same polarity which corresponds to the 0-mode. The direction of axial field are altered every π/ω seconds. The drift tube creates field-free regions and the RF electric field decays to zero, as in a waveguide below the cutoff frequency. The drift tube shields the particles when the polarity of the axial electric field is opposite to the beam direction (Fig. 2.6).

In the following chapters, the RF characteristic of DTL cavities will be studied. These investigations have been performed with the aim of analytical equivalent circuit model, numerical simulation and low power RF measurements. The stabilization and tuning of the axial fields in the DTL structures will be discussed in detail.

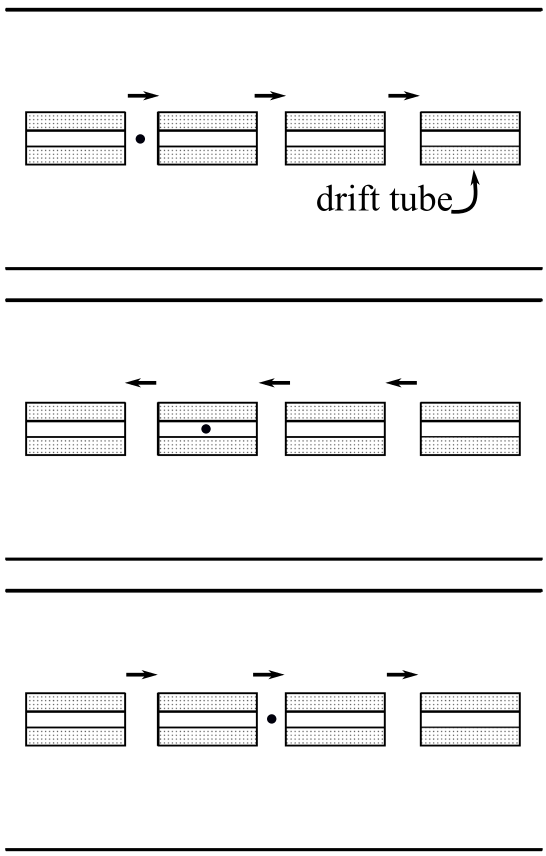

Figure 2.6: A particle moving in a drift tube linac structure. The arrows represent the direction of electric field in gaps. The drift tubes shield the particle when the polarity of the axial electric field is opposite to the beam direction.

Chapter 3

RF measurements

After fabrication of an accelerating cavity, the axial electric fields and resonance frequency are not exactly matched to the design values. RF measurements are essential to measure and tune these parameters. The difference of axial fields with respect to design values affects the longitudinal emittance and in the case of strong variations, the transmission of the beam. For the three CERN Linac4 DTL cavities, the beam dynamics study of randomly distributed axial field amplitude errors shows that the beam quality is acceptable up to a field flatness of $\pm 2\%$. From $\pm 2\%$ to $\pm 5\%$ halos start forming [20]; Halos develop when a fraction of particles acquire enough transverse energy from repulsive space-charge forces, and this leads to uncontrolled beam loss [32]; All Linac4 DTL cavities thus need to be tuned to below $\pm 2\%$ variation in flatness to avoid beam loss and deterioration in beam quality.

A precise and reliable measurement technique is essential for measuring field flatness. In the present section, a practical technique for electric field measurements and the errors in this measurement technique will be discussed in detail. Since field flatness of less than $\pm 2\%$ should be achieved, the effect of errors on reproducibility of E_0 measurements should be several times smaller than $\pm 2\%$. It will be discussed how the errors can be handled and how to improve the E_0 measurement precision and accuracy.

3.1 Slater perturbation theorem

The axial electric field can be measured on the basis of the Slater perturbation theorem. According to this theorem, for any particular cavity resonator, any perturbation such as changing the volume or inserting an external object inside the resonator causes a resonance frequency shift as [33]

$$\frac{\Delta f_r}{f_r} = \frac{\Delta W_m - \Delta W_e}{W_t}, \tag{3.1}$$

where ΔW_e and ΔW_m are the changes in stored electric and magnetic field energies, respectively. W_t is the total stored energy in the cavity. Consider a small metallic object which is located somewhere on the cavity axis. This object is called a "bead". Since the bead dimensions are small compared to the cavity dimensions, the variation of W_t due to the bead perturbation is negligible. For an arbitrary bead of volume ΔV, the equation 3.1 can be written as

$$\frac{\Delta f_r}{f_r} = \frac{\int_{\Delta V} \overrightarrow{P}.\overrightarrow{E} dV - \int_{\Delta V} \overrightarrow{M}.\overrightarrow{H} dV}{2W_t}, \tag{3.2}$$

where $\overrightarrow{P}$ and $\overrightarrow{M}$ are the polarization and magnetization of the bead, respectively [34]. Also, $\overrightarrow{E}$ represents the electric field and $\overrightarrow{H}$ represents the magnetic field.

Since the bead dimensions are point-like, it is sensible to assume that the bead is located in uniform electric and magnetic fields. Therefore, the magnitude and direction of the electromagnetic field are approximately the same, everywhere around the bead (Fig. 3.1).

Using Maxwell's equations, one can calculate the polarization and magnetization of a spherical bead located in a uniform electromagnetic field analytically as [35, 36]

$$\overrightarrow{P} = 3\epsilon_0 \frac{\epsilon_r - 1}{\epsilon_r + 2} \overrightarrow{E}, \tag{3.3}$$

$$\overrightarrow{M} = 3\mu_0 \frac{\mu_r - 1}{\mu_r + 2} \overrightarrow{H}, \tag{3.4}$$

where ϵ_r and μ_r are the relative permittivity and permeability constants of the bead, respectively. Substituting equations 3.3 and 3.4 into equation 3.2 and integrating over a spherical bead of volume ΔV [34] yields

$$\frac{\Delta f_r}{f_r} = \frac{3\Delta V}{4W_t} \left[\frac{\epsilon_r - 1}{\epsilon_r + 2} \epsilon_0 E^2 + \frac{\mu_r - 1}{\mu_r + 2} \mu_0 H^2 \right]. \tag{3.5}$$

For a DTL, electric fields along the longitudinal axis are of interest. Simulation results show that along the longitudinal axis, the magnitude of the magnetic field is zero; therefore the frequency shift is

$$\frac{\Delta f_r}{f_r} = \frac{3\Delta V}{4W_t} \left[\frac{\epsilon_r - 1}{\epsilon_r + 2} \epsilon_0 E^2 \right]. \tag{3.6}$$

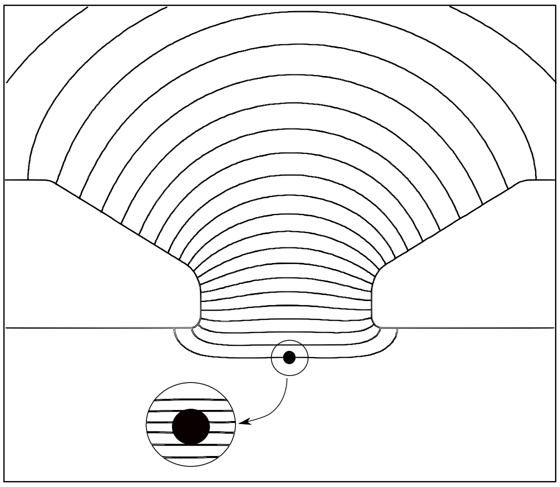

Figure 3.1: Because of the point-like dimensions of the bead, one can calculate the polarization and magnetization approximately as a dielectric sphere or cylinder located in uniform electric fields.

Similarly, the resonance frequency shift created by a cylindrical bead of length l_{bead} and diameter of d_{bead} along the axis is

$$\frac{\Delta f_r}{f_r} = -\frac{\Delta V}{2W_t}\frac{\epsilon_r - 1}{1-(\gamma(\epsilon_r - 1))}\epsilon_0 E^2, \tag{3.7}$$

where

$$\gamma = \frac{e^2}{1-e^2}\left[\frac{1}{2\sqrt{1-e^2}}\ln\left(\frac{1+\sqrt{1-e^2}}{1-\sqrt{1-e^2}}\right) - 1\right] \text{and} \quad e = \frac{l_{bead}}{d_{bead}}.$$

For the special case of using a perfectly conducting bead, the frequency shift is proportional to

$$\frac{\Delta f_r}{f_r} \propto \frac{\Delta V}{W_t}\epsilon_0 E^2$$
$$\frac{\Delta f_r}{f_r} = \alpha_{bead} E^2. \tag{3.8}$$

Where α_{bead} is the proportionality constant.

3.2 Resonance frequency measurements

In the previous section, we see that the electric field can be measured by measuring the resonance frequency shift created by a bead. In following, two common techniques to measure the frequency shift, will be discussed.

3.2.1 Measurement using phase-locked loop

The frequency shift can be measured by driving a cavity by a phase-locked loop (PLL) that locked the driving frequency to the resonant frequency of the cavity. The architecture of the electronic setup to measure the resonance frequency of a cavity is plotted in Fig. 3.2. A signal generator produces an RF signal with known frequency of f_0, then the signal is divided into two branches. The signal of the first branch drives the cavity. The second branch and the reflected signal from the cavity enter to RF and LO input of a frequency mixer, respectively. The mixer takes an RF input signal at a frequency f_1, mixes it with an LO signal at a frequency f_2, and produces an intermediate frequency (IF) output signal that consists of the sum and difference frequencies, $f_1 \pm f_2$. Then using a low pass filter, the high-frequency part of the signal is filtered and the output is measured with a voltmeter. When the frequency difference is non-zero, a feedback is sent to the signal generator in a PLL and depend on the difference of frequencies, the generator provides a signal with the frequency of $f_1 + \Delta f$. This process repeats until the $f_1 = f_2$ and then frequency from the counter will be the cavity resonance frequency [37, 38].

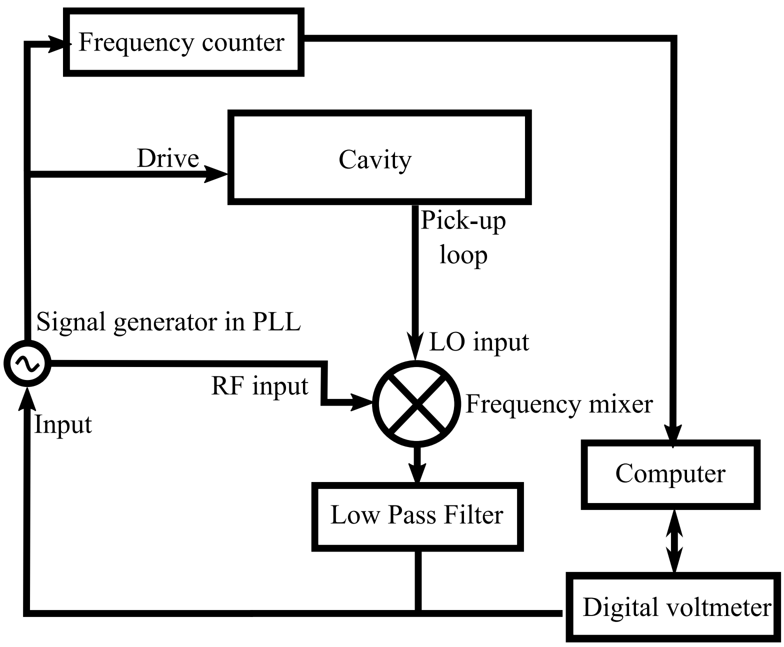

Figure 3.2: Basis of resonance frequency measurement using a phase-locked loop.

3.2.2 Measurements using vector network analyzers

In the section 3.2.1, a method to measure the resonance frequency shift of a cavity using a PLL was discussed. In following, an alternative method to measure the resonance frequency shift will be presented. In this method, the frequency response of a network is measured using a vector network analyzers (VNA). The principle of a typical VNA is plotted in Fig. 3.3. Here a known RF wave is generated by a precise generator and then it is split in two parts. The first part of generated wave is sent to the network that is studied, also referred to as the “Device Under Test (DUT)”. The reflected wave from the DUT and the second part of the generated wave are sent to an amplitude and phase detector. By comparing the two signals, the VNA returns the amplitude and phase of the S parameters [39].

The VNAs are made to measure S-parameters, not the resonance frequency. Hence, the resonance frequency measurement of a DUT using a VNA is performed indirectly. For instance, the S_{11} can be measured as frequency sweeps in a relatively wide range around resonance. Then, the resonance frequency of the network is the frequency at which S_{11} is minimum. In this measurements, many measurements shall be performed just for one resonance frequency measurement.

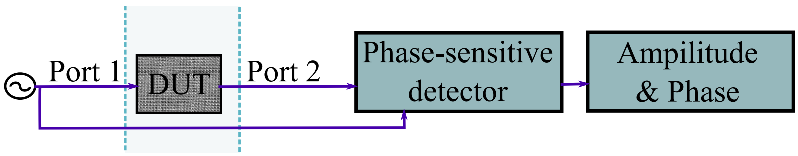

Figure 3.3: The principle of a vector network analyzer.

3.2.2.1 Phase shift measurements

Instead of looking at a DUT as a linear two ports network, let us represent it by an RLC equivalent circuit (Fig. 3.4). The equivalent admittance of DUT can be written as

$$Y_{in} = \frac{1}{R}\left[1 + j\omega_r CR\left(\frac{\omega}{\omega_r} - \frac{\omega_r}{\omega}\right)\right]. \tag{3.9}$$

In this equation, the $\omega_r CR$ is the circuit quality factor (Q). The admittance in the vicinity of resonance is

$$Y_{in} \approx \frac{1}{R}\left[1 + j2Q\frac{\omega - \omega_r}{\omega_r}\right] = \frac{1}{R}\left[1 + j2Q\frac{\Delta\omega}{\omega_r}\right], \tag{3.10}$$

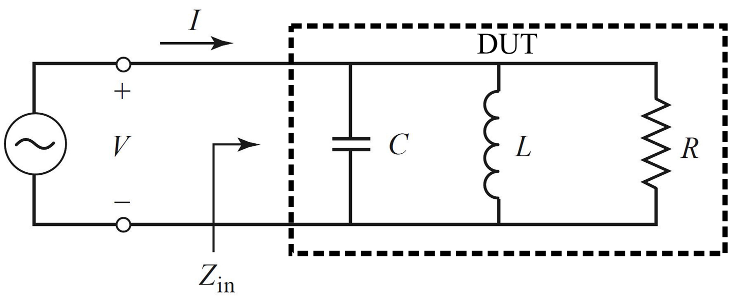

Figure 3.4: A parallel RLC equivalent circuit representation of a DUT.

Consequently the phase of admittance is

$$\varphi = \arctan\left(2Q\frac{\Delta\omega}{\omega_r}\right) \rightarrow 2Q\frac{\Delta\omega}{\omega_r} = \tan(\varphi). \tag{3.11}$$

The unperturbed phase φ_u at the resonance frequency of the circuit ($\omega = \omega_r$) is

$$\tan(\varphi) = 0 \rightarrow \varphi_u = 0. \tag{3.12}$$

For small perturbation, the change in Q is negligible and the resonance frequency of the perturbed circuit changes to ω_p. The phase of perturbed circuit φ_p at the frequency of ω_r is

$$2Q\frac{\omega_r - \omega_p}{\omega_p} = \frac{\Delta\omega}{\omega_p} = \tan(\varphi_p). \tag{3.13}$$

For a small perturbation, ω_p in the denominator can be replaced by ω_r. Therefore

$$\frac{\Delta\omega}{\omega_r} \approx \frac{\tan(\varphi_p)}{2Q}. \tag{3.14}$$

Therefore, instead of measuring the frequency shift, it is possible to measure the phase shift at the frequency of ω_r using a VNA and then to convert the phase shift to a frequency shift using the equation 3.14 [40]. Finally applying the last equation into the equation 3.8 yields

$$E^2 \propto \frac{\tan(\varphi_p)}{2Q}. \tag{3.15}$$

3.3 Bead-pull measurements

The bead-pull measurement technique (BM) is a well-known technique that is used widely for measuring the electromagnetic field inside RF cavities. The measurement techniques is on the basis of Slater perturbation theorem and the fact that the bead perturbs the field at its position. The perturbation changes the resonance frequency of structure. According to the equation 3.8, the frequency shift Δf_r is proportional to the square of the electric field at the bead position. This allows measuring the field distribution in the accelerating structure while a bead is pulling inside the structure. A schematic view of the bead-pull measurement bench is plotted in Fig 3.5. The bead is pulled smoothly along the cavity axis using a motor and the resonance frequency shift can be measured by the use of different means such as VNA or PLL. The higher sampling rate of resonance frequency measurement lead to measure with higher resolution at a certain amount of time. The proportionality constant (α_{bead}) in the equation 3.8 is not important for DTL tuning and stabilization because the purpose of tuning is to reduce the relative average axial field variation along the cavity axis. In order to measure the exact value of axial fields, the α_{bead} can be determined by a bead calibration with a pillbox cavity where the exact value of electric fields are known from analytical studies [41]. More details about BM system can be found in [41–45]. The Linac4 bead-pull measurements bench and data acquisition system are also discussed in the Appendix: A.

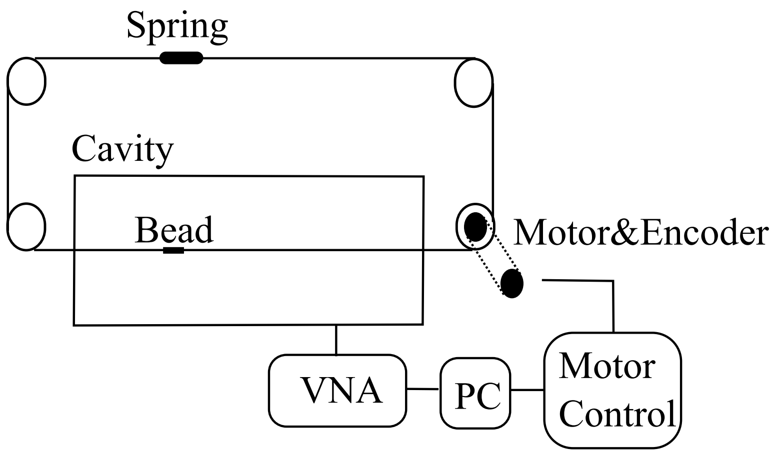

Figure 3.5: A layout of a bead-pull measurements bench.

3.4 Errors in bead-pull measurement

The goal of bead-pull measurement is to know the electric field distribution on axis of a cavity. Then, the average axial fields and the field flatness of the cavity are extracted from the measured field distribution. In order to measure a reliable field flatness values, the measurement errors should be minimized.

The errors can be classified in two types of static and dynamic. The static error is defined as the difference between the true value of the measured variable and the value indicated by the instrument. Static errors are caused due to limitations of the instruments as well as due to certain shortcoming in the measurement process. The static errors are divided into gross errors, systematic errors and random errors [46].

The systematic errors cause a constant or in a regular fashion changes of a same quantity in successive measurements (Fig 3.6). The systematic errors can be eliminated from measurements by introducing corrections. Systematic errors are normally estimated by theoretical analysis of the measurement conditions, based on the known properties of measurement and of measuring instruments. Sources of systematic error may be imperfect calibration of measurement instruments or changes in the environment which interfere with the measurement process. In contrast to the systematic errors, the effect of random errors on the results of separate measurements of same quantity cannot be predicted [47]. In consequence, the measured values are scattered around the true number (Fig 3.6). The random error can be decreased by using more precise instrument. The gross errors mainly occur due to carelessness or lack of experience of human being. This type of errors is also known as personal error. This error can be minimized by paying great attention while reading and recording results or adjusting parameters of measurement system. The other effective way to reduce this kind of errors is to repeat measurement by different person [46].

The quality of measurements that reflects the closeness of the results of the same quantity measurements performed under the same conditions is called the repeatability of measurements. Good repeatability indicates that the random errors are small. The quality of measurements that reflects the closeness of the results of measurements of the same quantity performed under different conditions, i.e., in different laboratories (at different locations) and using different equipment, is called the reproducibility of measurements. Good reproducibility indicates that both the random and systematic errors are small [47]

The relative standard deviation (RSD) or coefficient of variation is a parameter to describe the measurement precision. For an array of measured data x of the same quantity with the standard deviation of σ and average of $\bar{x}$, the RSD is defined as RSD=$100 \times \sigma/\bar{x}\%$. The lower RSD indicates the higher precision in measurements [48].

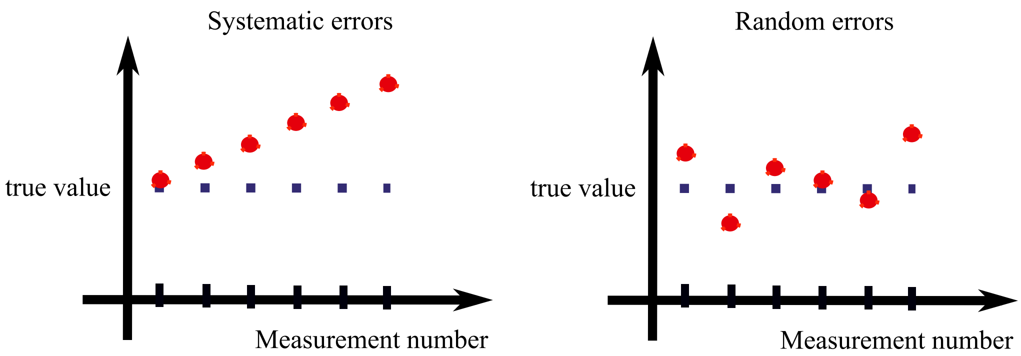

Figure 3.6: A representation of a typical systematic and random errors on measurements. Left: The systematic errors causes a regular fashion changes of a same quantity in successive measurements. Right: The measured values of same quantity are scattered around its true number because of random errors.

3.4.1 The vector network analyzer uncertainties

The measurements with VNA is subject to measurement uncertainty, which causes to statistical deviation of the measured value from its true value. In the measurement domain, one distinguishes two types of uncertainties: random and systematic. Random errors may be caused by instrument noise, repeatability of switches, cables and connectors. This kind of error cannot be removed through calibration and must be reduced by taking care of different factors that may affect measurements. For example, using high quality cables, providing thermal equilibrium condition around VNA and connectors. In addition, the proper choice of IF-bandwidth (IF-BW) and averaging factor is a way to reduce the effect of random errors. These parameters control the built-in functions in VNA which are performing the digital filtering and the post-processing on the measured signal. However, the lower IF-BW and higher averaging factor lead to lower noise. On the other side, these processing requires a longer sweep time [49, 50].

VNA needs calibration to ensure it is operating within manufacturer specifications. To achieve high accuracy, a user calibration is performed more frequently. This is accomplished with a set of calibration standards from a network analyzer calibration kit. By comparing known values, stored in the VNA, against measured values of the calibration standards, a set of correction factors is created [51]. A reflection measurement is shown in Fig. 3.7 with and without one-port calibration. The results are reported by Agilent [52]. Because of systematic errors interfering with the test signal, the ripple pattern appears in the results. By calibration, the return loss trace is much smoother and better represents the actual reflection performance of device.

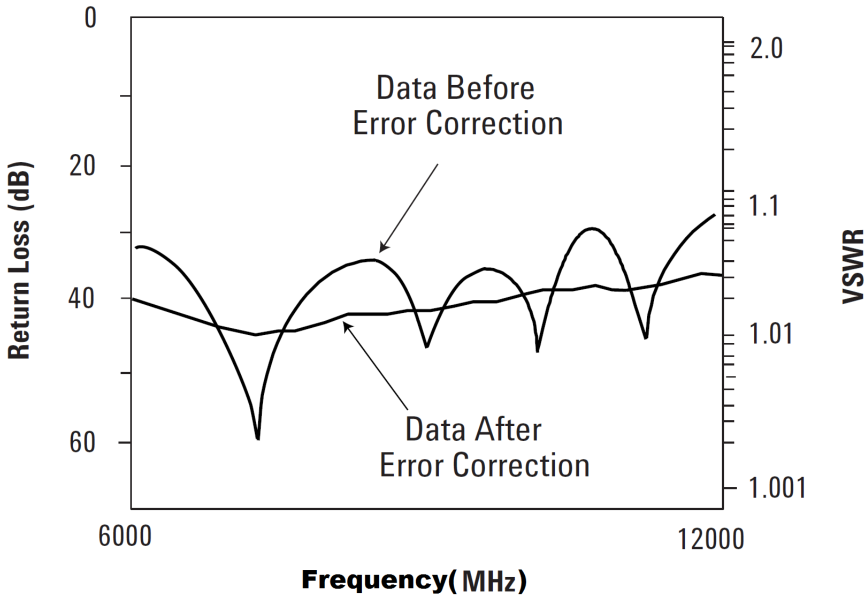

Figure 3.7: A reflection measurement with and without one-port calibration.

3.4.2 Relative permittivity variation

The axial field in DTL cavities are measured when the cavity is not under vacuum; therefore, the air inside the cavity acts as a dielectric material during the measurements. In consequence, the resonance frequency of the cavity is slightly different from what it is expected to be under vacuum. In the vacuum, the resonance frequency is

$$f_{vac} = \frac{c}{\lambda} = \frac{1}{\sqrt{\epsilon_0 \mu_0}\lambda}. \tag{3.16}$$

The presence of air changes the dielectric constant of the medium $\epsilon = \epsilon_r \epsilon_0$ so the resonance frequency in air is

$$f_{air} = \frac{1}{\sqrt{\epsilon \mu_0}\lambda} = \frac{f_{vac}}{\sqrt{\epsilon_r}}. \tag{3.17}$$

The dielectric constant of air depends on ambient temperature T (°K), air pressure P_{air} (hPa), the vapor water pressure P_{water} (hPa) and relative humidity (RH) in percent. It has been shown in the previous works [53,54] that the relative permittivity can be written as follows

$$\epsilon_r = 1 + \left(\frac{157.9}{T} P_{air} + \frac{180\left(1 + \frac{5580}{T}\right)}{T} P_{water} RH \right) \times 10^{-6}, \tag{3.18}$$

where the vapor pressure of water can be approximated using

$$P_{water} = 0.75 \exp\left(20.386 - \frac{5132}{T}\right) \text{hPa}. \tag{3.19}$$

By considering T= 297 K, RH=30% and P_{air} = 999.9 hPa into equation 3.18, the resonant frequency with air is around 120 kHz less than in vacuum; i.e. 352.08 MHz instead of 352.2 MHz.

The relative humidity, the temperature and the air pressure are not fixed and these parameters are changed during measurement. Consequently according to equation 3.18, the dielectric constant changes. As a result, the measurement condition changes during the measurement.

3.4.3 Errors of Bead-pull measurements bench

In section 3.4.2, the effect of different environmental factors on the bead-pull measurement has been discussed. Another kind of error belongs to the measurement system itself. These errors will be discussed in the following.

3.4.3.1 Wire slippage

The mechanical setup of the bead-pull measurement system contains a wire and pulleys. In our system, the wire slips randomly on plastic pulleys. It is possible to reduce the number of wire slippage in measurements by equipping pulleys with rubber rings and controlling the motor speed.

The effect of a typical bead slippage on measured phase shift is shown in Fig. 3.8. When the wire is slipped, the measured phase shift changes suddenly because of a sudden displacement of the bead. Consequently due to bead displacement, information of the measured phase in the interval of slippage is missing. In consequence, the integration of electric field in the cell is lesser than the actual value.

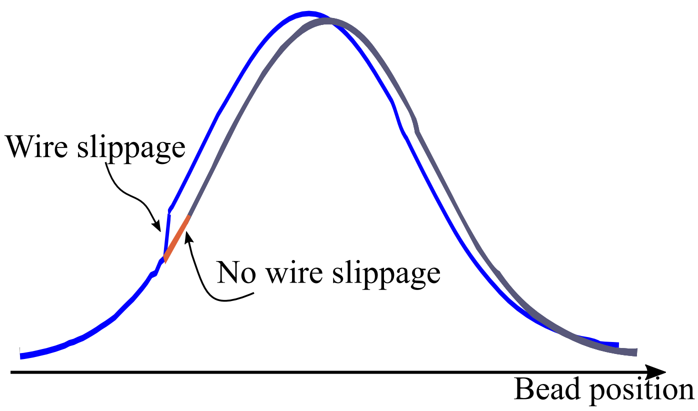

Figure 3.8: The wire slippage effect on the measured phase shift.

The two bead-pull measurement results of the segment1 of Tank1 is shown in Fig. 3.9. In a particular case shown by blue circles, no wire slippage has been seen and the average axial field has been considered as the reference value. In the other measurement shown by red diamonds, the measured axial electric field of the 20^{th} cell is about 9% less than the reference value. This error is created by wire slippage.

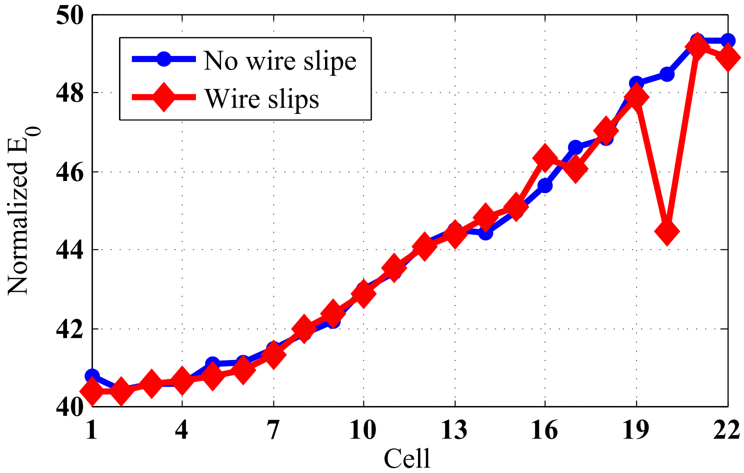

Figure 3.9: The two bead-pull measurement results of the segment1 of the Tank1 with and without slippage in the cell number 20.

3.4.3.2 Bead size

So far, it has been assumed that the electric field is uniform along the bead due to point like bead approximation and the electric field is measured using equation 3.15. But actually, the bead is not infinitesimal. It is possible to have a more uniform electric field over the bead by choosing a smaller bead, but this decreases the signal to noise ratio in measurements. From Slater perturbation theory, the frequency shift is proportional to the change of energy due to the presence of the bead i.e.

$$\Delta f \propto \int_{\text{bead length}} E(l)^2 dl \tag{3.20}$$

In order to study how much the bead length affects the measurement accuracy, the SUPERFISH simulation is performed. To simulate the effect of the bead, first, the axial field distribution is extracted from simulation along the cavity axis and the electric field distribution are converted to frequency shift distribution by using equation 3.20. Then the average axial electric fields are calculated from the frequency shift distribution. Also the real average axial field (for a point-like bead) is extracted from simulation. The results of different bead length is plotted in Fig. 3.10. This calculation is repeated for different bead lengths from 0.2 to 1.4 cm every 0.3 cm. As an instance, the error of average axial field measurement of cell number 39 for different bead length is listed in table 3.1.

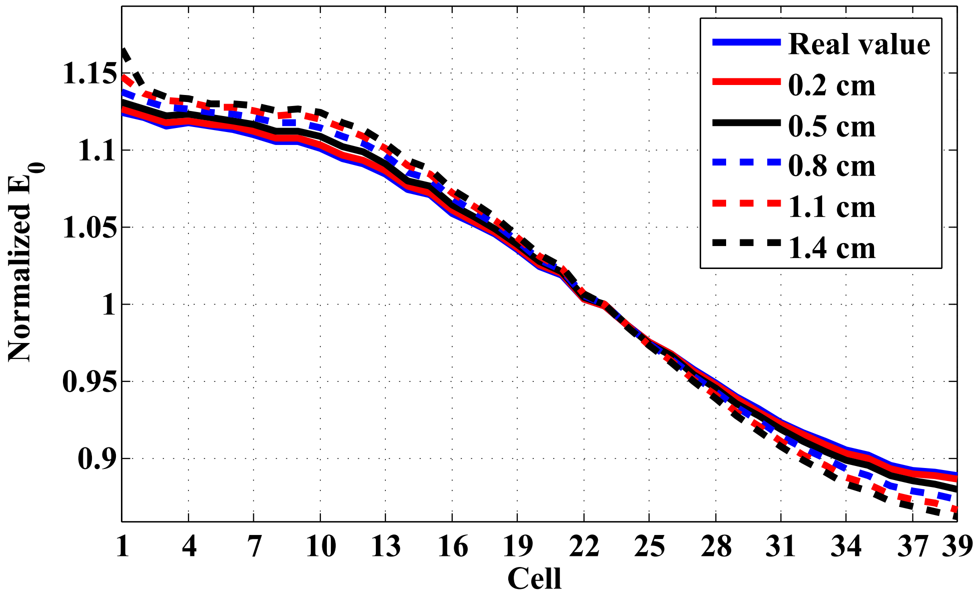

Figure 3.10: Comparison of frequency shift of different bead length using SUPERFISH simulation.

L(cm)	0.2	0.5	0.8	1.1	1.4
Error of E_0 (%)	0.5	1.25	1.9	2.5	3.2

Table 3.1: The error of average axial field measurement of cell number 39 for different bead length.

3.4.3.3 Wire sag

The wire is not weightless and therefore gravitation acts on it. As is shown in Fig 3.11, the wire is sustained by two pulleys and is tensioned by a spring connected to both ends of the wire. Depending on the amount of tension T, wire mass and bead mass, the wire may deflect from the straight line and lead to measuring the off-axis electric field.

The maximum error of measuring off-axis electric field with respect to the nominal fields have been calculated in SUPERFISH. In this calculation, it is assumed that the

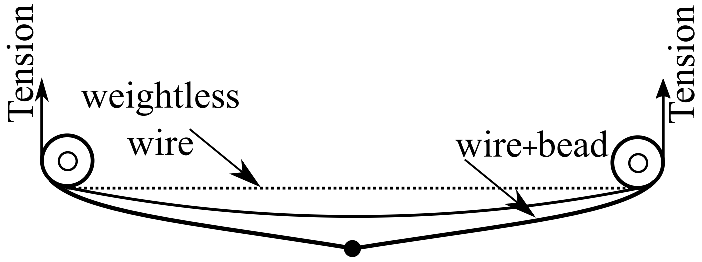

Figure 3.11: Wire sag.

wire has a uniform offset with respect to the cavity axis and the E_{0m}^{offset} are axial field of this case. If the nominal axial field of the m^{th} cell in the middle of DTL without offset be E_{0m}, the relative errors are calculated using $\left|E_{0m}^{\text{offset}} - E_{0m}\right| / E_{0m} \times 100$. According to calculations, the relative error of the m^{th} cell growth quadratically with respect to the offset. Hence, for 0.5 mm and 1 mm displacement of wire, the average field error of the m^{th} cell are bout 0.2% and 0.6%, respectively.

In order to adjust deflection, one should calculate the maximum wire deflection as a function of the tension exerted on both ends of the wire. The deflection of the wire in the absence of the bead can be calculated using the so called Catenary formula [55, 56]. In this analytical relation, it is assumed that the wire mass is distributed homogeneously but in our problem, the density is not homogeneous because of the bead mass. Therefore one should calculate the deflection considering both of wire and bead weight. The maximum wire deflection as a function of the tension is calculated numerically. The results for different wire lengths are plotted in Fig. 3.13. The wire which is used in our measurement was homogeneous with a linear density of λ_{wire}=0.0352 g/m and a bead weight of 0.2 g. The calculation shows that for 4 m and 8 m long cavities, 15 N tension on the wire respectively leads to 0.21 mm and 0.65 mm maximum deflection. By increasing the tension on wire up to 20 N, the maximum deflection of 4 m and 8 m wire are reduced to about 0.14 % and 0.35%.

3.5 Analysis techniques Improvements

The errors on Linac4 DTL bead-pull measurements bench has been discussed. In this section, the two practical and essential upgrades which have been performed on Linac4 DTL measurement system will be discussed in detail.

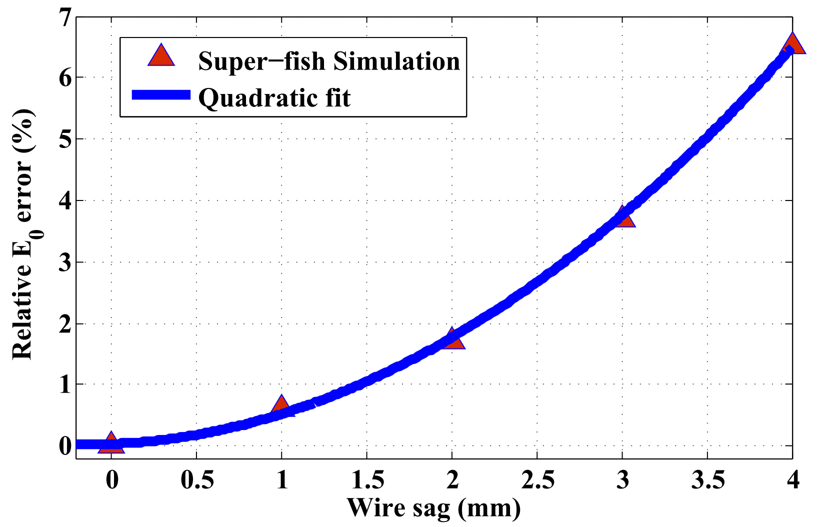

Figure 3.12: Error of measuring off-axis axial field with respect to the nominal fields.

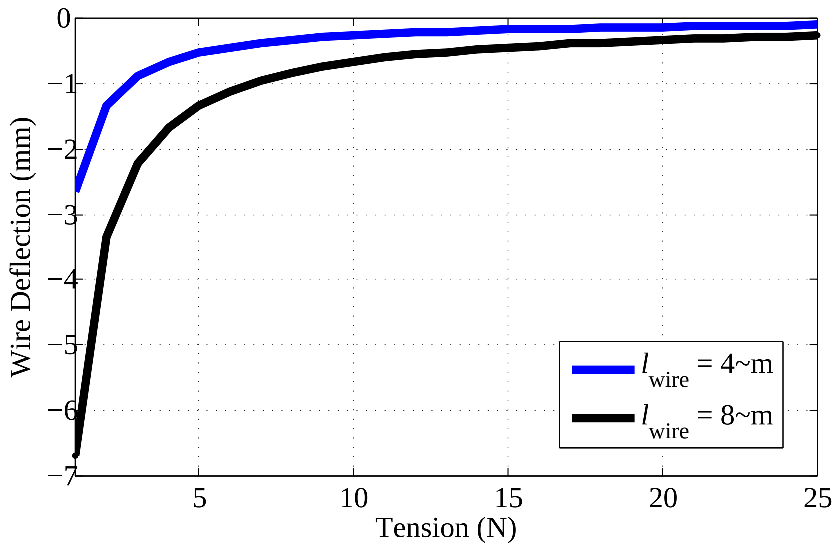

Figure 3.13: The calculated maximum wire deflection of a 4 and 8 meter long wire as function of the tension on both sides of wire.

3.5.1 Environmental effects

Since the electric and magnetic stored energy inside drift tubes are negligible, the resonance frequency shift when the bead is located inside of the drift tube is expected to be zero. But in measurements (see Fig. 3.14), the resonance frequency shift inside drift tubes are not zero. The error of phase shift measurement due to change of the dielectric constant, is quite complex and unpredictable over long periods, but it changes approximately linearly for a short periods of time (around few minute). The measurement time was set at around 4 minutes for Linac4 DTL cavities. In this case, the duration of the bead inside each cell is less than 10 s.

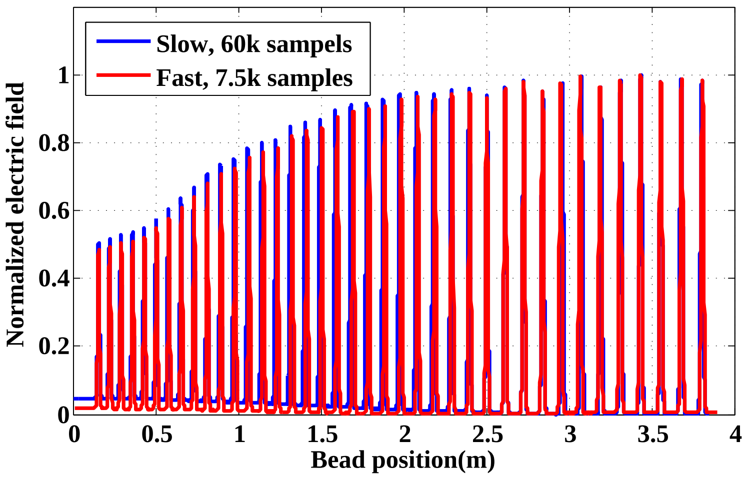

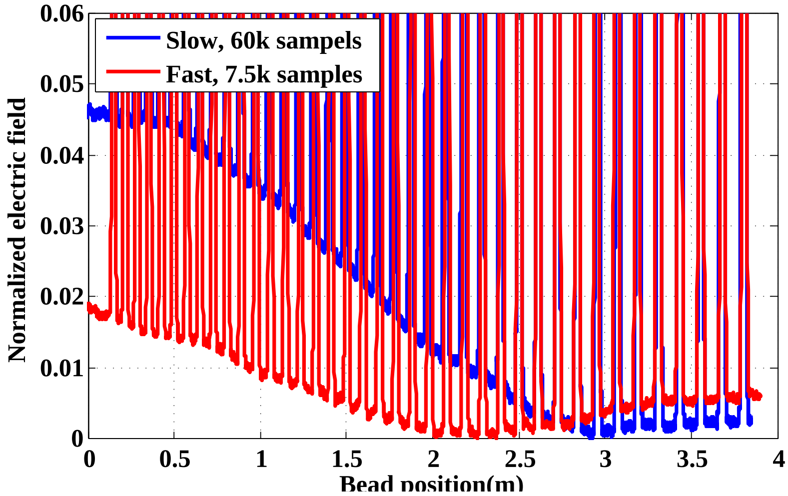

Figure 3.14: Top: A typical electric field measurement result. The measurements are carried out for DTL Tank1 for two different motor speeds at the same sampling time of 8μs. Bottom: Zoom showing of the normalized electric field.

Although the ambient factors may have a serious and detrimental effect on measurements, it is possible to eliminate their effect by upgrading the measurement analysis techniques and performing some numerical post-processing on the results. The systematic errors add a linear term of a_1t+b_1 to the measured phase shift ($\Delta\varphi_{\text{measured}}$). Here, t represents the time or bead position. The a_1 and b_1 are the constants which can be determined by fitting a line which connects the phase value of centers of two next drift tubes. In consequence, the measured phase considering environmental errors for each cell is $\Delta\varphi_{\text{measured}} = \Delta\varphi_{\text{slater}} + (a_1 t + b_1)$. The $\Delta\varphi_{\text{slater}}$ is the phase shift which is come from bead perturbation. So finally, the phase shift due to perturbation is $\Delta\varphi_{\text{slater}} = \Delta\varphi_{\text{measured}} - (a_1 t + b_1)$.

In order to study the efficiency of the post-processing method, the peaks in the measured electric field are extracted from 8 consecutive bead-pull measurements of Tank1. The RSD of the measured peaks is plotted in Fig. 3.15 for two cases: without and with post-processing. Without post-processing, the RSD of peak measurement of different cells are in the range of [0.3, 1.4]%, but after correction, the RSD values are distributed between 0.18% to 0.43%.

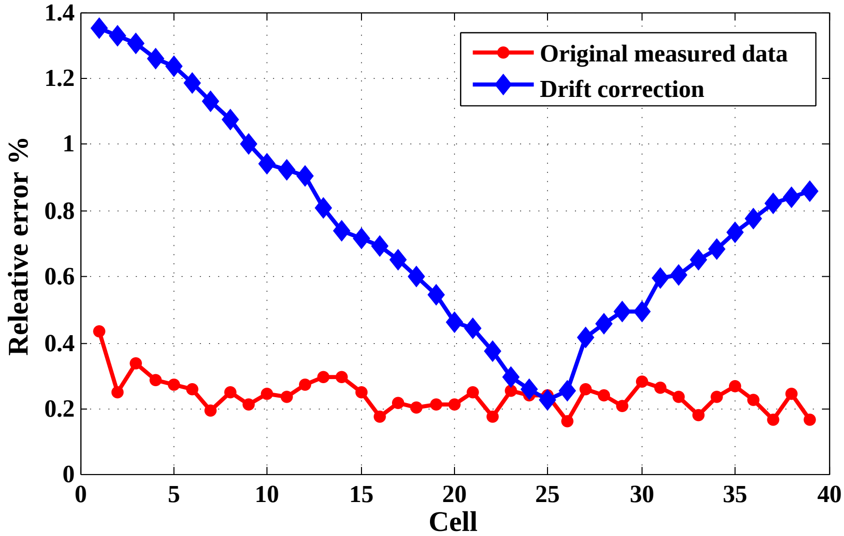

Figure 3.15: Comparison of error in axial field measurements for two cases: without and with post-processing.

3.5.2 The peak field analysis

In the following, an important upgrade of the bead-pull measurement system to extract more precise and accurate axial field value - without direct integrating - is discussed. This method is called “Peak Field Method” [57]. In the following, the theory of this method and its advantages are discussed in detail.

In this technique, the peak field values are extracted from the measured phase shift and the relevant average axial field values are calculated by comparing these values and simulated peak field coefficients. For the case that the bead center is located at the peak of the phase shift, the peak field value is defined as

$$pf_i = \oint_{V_{\text{bead}}} E(z)^2 dz \bigg|_{\text{bead center located at peak of phase shift of the } i^{\text{th}} \text{ cell}}, \tag{3.21}$$

where i is the cell number and V_{bead} is the volume of the bead. Since in our case a cylindrical bead of a thickness of less than 2 mm is used, the integration over the volume reduces to the bead length l_{bead}. For the case of a metallic bead, the peak field value of the i^{th} cell is proportional to the energy difference between unperturbed and perturbed cavity, and consequently it is proportional to the frequency or phase shift of the cavity.

The peak field coefficients are defined as

$$\text{p.f.c}_{\text{i}} = \frac{\int_{\text{z}_{\text{peak}}-(\text{l}_{\text{bead}}/2)}^{\text{z}_{\text{peak}}+(\text{l}_{\text{bead}}/2)} \text{E}^2(\text{z})\text{dz}}{\left(\int_0^{\text{L}_{\text{cell}}} \text{E}(\text{z})\text{dz}\right)^2}. \tag{3.22}$$

The peak field coefficients depend on the drift tube shape, the gap length and the bead length. Any other perturbation from cavity walls by slug tuners or the vacuum port or the power coupler has no effect on these coefficients. In order to verify the independency of peak field coefficients to cylindrical wall perturbation, SUPERFISH simulations are used. A tuning ring at the middle of DTL Tank1 is simulated (Fig. 3.16). The p.f.c values of a 7 mm bead length are calculated for different penetration of this tuning ring. For instance, the variation of the p.f.c value of the 7^{th} cell is plotted in Fig. 3.17. According to this investigation, the p.f.c stays the same regardless of the penetration of tuners. Therefore, taking the p.f.c value of the i^{th} cell with cell length L_i, one can measure the peak field using equation 3.21 and the axial field can be extracted using equation 3.22, i.e.:

$$E_{0i}^2 = \frac{pf_i}{\text{p.f.c.}_{\text{i}} \times \text{L}_{\text{cell}}^2}. \tag{3.23}$$

In Fig. 3.18, the measured axial field obtained by direct integration, is compared to peak field method. The average axial field obtained by peak field and direct integration are plotted for the same cavity. In this plot, the error-bars indicate two of standard deviations of measurement i.e. 2σ. The RSD of measured axial fields obtained by direct integration and peak field method are listed in Table 3.2. Using direct integration, the RSD of measured values for different cells except the end cells are varied between 0.37% and 1.78%. The RSD values of measured axial fields obtained by peak field method are between 0.06% and 0.18%.

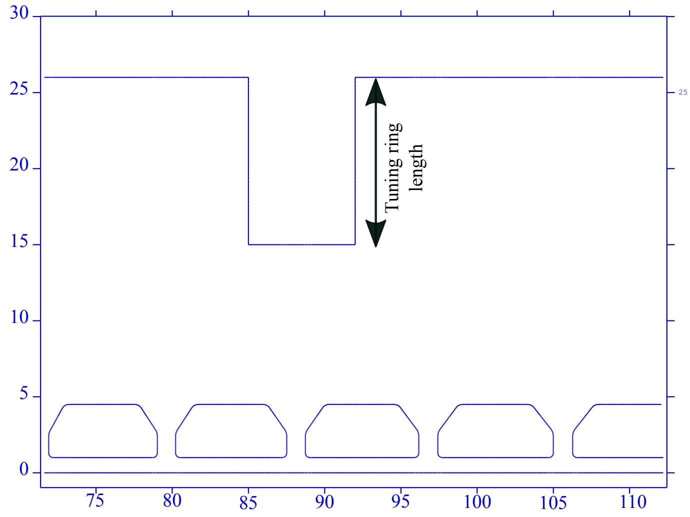

Figure 3.16: Simulated geometry of a tuning ring to study the effect of perturbation on peak fields.

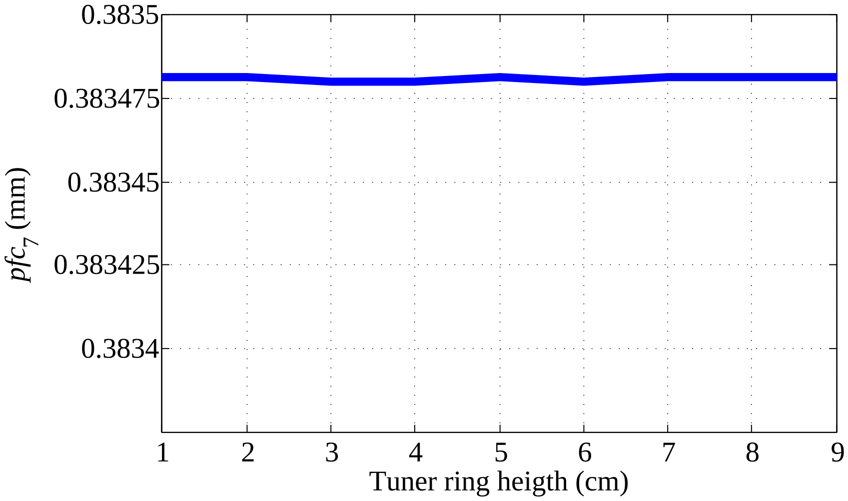

Figure 3.17: The peak field value of 7 cell of DTL Tank1 as function of tuner ring height.

The advantage of the peak field analysis technique in comparison to the direct integration are

1. The effect of bead length has been taken into account because the p.f.c values are calculated for the same bead length as used in the measurements.

2. The phase variation rate around the peak is zero so in case of wire slippage around the peak, the measured peak field is close to the real peak value.

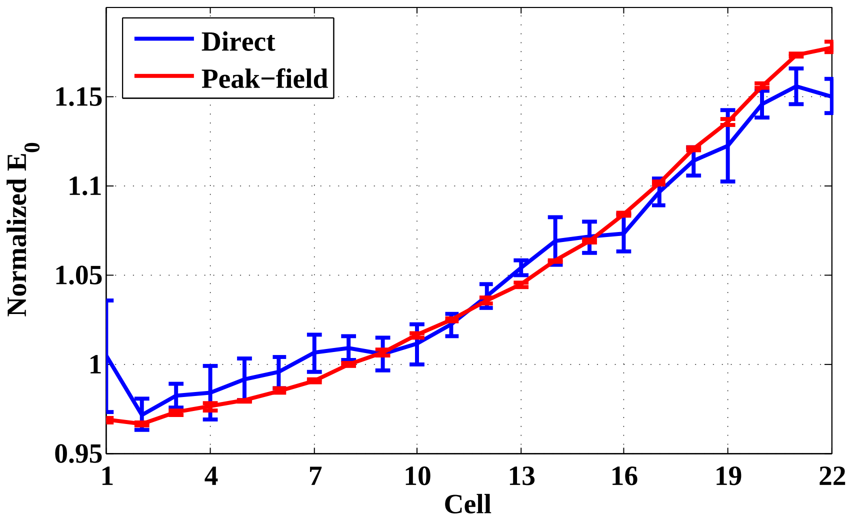

Figure 3.18: Measured axial electric field obtained using the peak field and the direct integration technique.

3. The measurement can be performed at a higher speed without any effect on the measurement accuracy of the field.

4. The average RSD value of different cell in measurements obtained by direct integration is about $\pm$ 0.9%. By using peak field technique, the average RSD is decreased down to $\pm$0.1%.

Cell number	RSD% (Direct integration)	RSD% (Peak field method)
1	3.09	0.14
2	0.87	0.09
3	0.67	0.14
4	1.52	0.18
5	1.18	0.06
6	0.88	0.16
7	1.03	0.10
8	0.65	0.10
9	0.90	0.16
10	1.10	0.12
11	0.59	0.07
12	0.65	0.15
13	0.37	0.09
14	1.25	0.06
15	0.81	0.07
16	0.98	0.08
17	0.68	0.09
18	0.69	0.08
19	1.78	0.15
20	0.62	0.09
21	0.86	0.06
22	0.84	0.24
Average	0.90	0.10

Table 3.2: The RSD of measured E_0 obtained with direct integration and peak field method for Linac4 DTL Tank1 segment 1.

Chapter 4

Stabilization theory

4.1 Importance of stabilization

In real cavities, there are always different kinds of perturbations that may influence the cavity parameters from the design values. Among these perturbations, manufacturing errors cannot be simulated in the design stage. Also, because of variation in cell length, DTL needs to be simulated in total not in cells. Therefore, optimization of a whole DTL using 3D simulations is not quick and straightforward. Hence, it is interesting to learn how one can stabilize the axial field with respect to the unknown distributed bunch of perturbations instead of treating them individually.

In order to make a cavity less sensitive to errors, one should first study the effect of perturbations on the axial field and the frequency of structure. Also a method to measure the stability levels of the structure with respect to errors needs to be defined. The final step is to investigate how the stability level of a DTL can be improved. The main goal of this chapter is to study the theory of axial field stabilization in detail.

4.1.1 Perturbation effects on axial field

To study the effect of tuning errors on the axial electric fields and resonant frequencies of a DTL structure, the DTL is modeled by a system of lumped circuit elements. Although such a model is not able to describe all physical aspects of the DTL structure, it is possible to find values of the equivalent circuit elements such that the calculated voltages and frequencies using the models behave as if they were in a real DTL cavity [58–60]. The model can also provide the analytical basis to study physics of electromagnetic waves in DTLs and one can study the behavior of axial field qualitatively under different situation. In the present work, the circuit model is used to investigate how perturbations affect axial fields of a DTL structure. Also, the circuit model is used to figure out how to minimize axial electric fields sensitivity against perturbation errors.

Let us consider the circuit representation of two sequential cells, as shown in Fig 4.1. The C_n represent the capacitance between drift tubes and L_n represent the inductance of the n^{th} cell. The C'_n is the capacitance between drift tube outer surface and cavity cylindrical wall and L'_n is the inductance of supporting stem. For the sake of simplicity in writing of equations, the series inductance and capacitance of an accelerating cell is replaced by a box of equivalent impedance of Z_n and the equivalent admittance of all of the coupling elements is considered as Y_n. Therefore, the Z_n and Y_n are equal to $j\omega L_n + (j\omega C_n)^{-1}$ and $(j\omega L'_n)^{-1} + j\omega C'{}_n$, respectively.

Since in the absence of perturbations, the structure resonates at the same frequency equal to the individual cells natural frequency i.e. $\omega = \omega_{0n}$, both of Z_n and Z_{n+1} are zero. Consequently the voltage difference between accelerating cells, i.e. $\Delta V = V_n - V_{n+1}$ is zero and the electromagnetic energy doesn't flow between cells.

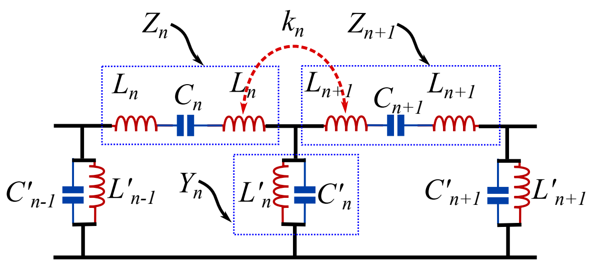

Figure 4.1: An equivalent representation of two neighboring cell of a DTL cavity. Instead of inductance and capacitance, the circuit can be studied in terms of equivalent cell impedance Z_n and coupling admittance Y_n.

Presence of tuning errors on the n^{th} cell changes the cell capacitance and inductance of that cell in addition to changing the cavity's TM_{010} frequency so that $\omega \neq \omega_{on}$ and consequently the $Z_n(\omega_{on})$ is not zero anymore. As a consequence, the current flows between cells. Part of the current divides at the node that connects impedance Z_n and coupling admittance Y_n. The current division is repeated in every cell and this leads to a tilt in the current profile along the structure.

The equivalent circuit of a DTL cavity consisting N cells is shown in Fig. 4.2. The structure is electrically shorted at both ends to consider effect of end covers. In order to study the effect of perturbation on the axial field, a structure with 20 identical cells is studied numerically by solving an eigenvalue system of equations. The details of calculations will be discussed in 4.1.2. Here, the stems are ignored to simplify the calculations. C_n, C'_n and ω_n have been considered 2.3×10^{-9} F, 4.44×10^{-12} F and 352 MHz, respectively. According to calculations (Fig. 4.3), the magnitude of normalized axial fields are 1 for all cells in the absence of perturbations which is expected because of zero voltage over the coupling admittance. Then the capacitance of the first or the last cell are perturbed artificially by about 0.1 % of its value. As is shown in Fig 4.3, part of the current goes through the coupling admittances Y_n in each cell due to perturbations and a tilt appears in axial electric fields.

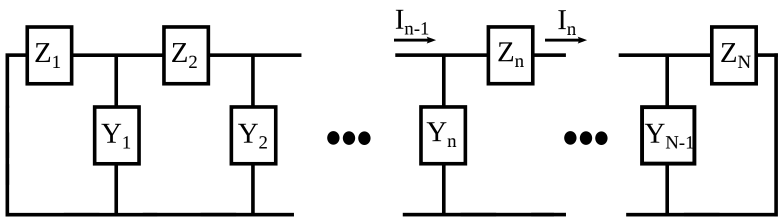

Figure 4.2: Circuit model representation of a whole DTL cavity containing N cells. The first and last cells are electrically shorted to consider the effect of metallic end covers.

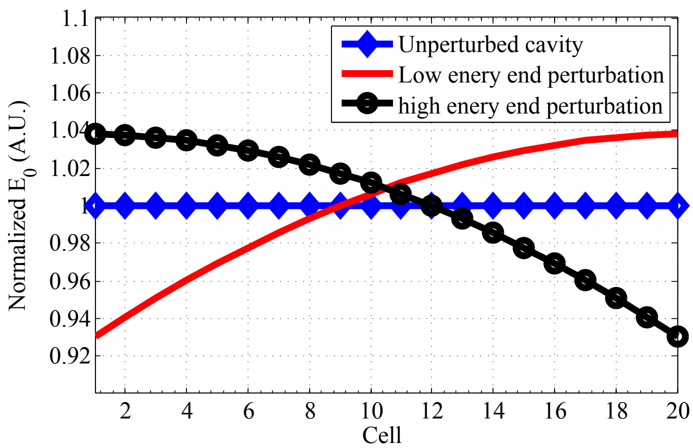

Figure 4.3: The calculated axial field in the absence and presence of perturbation. The calculation shows that perturbing each end of cavity leads to a considerable tilt in the axial field.

4.1.2 Equivalent circuit model representation

To understand the physics and behavior of axial field along the longitudinal axis of the cavity, it is worthwhile writing out the Kirchhoff equations in terms of lumped circuit elements (Fig.4.1). Since the accelerating voltage in each cell (V_n) is equal to a voltage over a capacitor, in the model the voltage can be written in terms of current, i.e. $i_n = j\omega C_n V_n$. Therefore we have

$$\left(j\omega L_n + \frac{1}{j\omega C_n}\right)i_n + \frac{i_n - i_{n+1}}{j\omega C'_n} - \frac{i_{n-1} - i_n}{j\omega C'_{n-1}} + j\omega M_{n-1} i_{n-1} + j\omega M_{n+1} i_{n+1} = 0,' \tag{4.1}$$

where M_n represents the mutual inductance and could be written as $M_n = k_n\sqrt{L_n L_{n+1}}$. By multiplying both sides of equation 4.1 by $j\omega C_n$ and moving the terms containing ω to the right hand side, we obtain

$$\left(1 + R_{n(n-1)} + R_{nn}\right)i_n - R_{nn} i_{n+1} - R_{n(n-1)} i_{n-1} = -\omega^2\left(\frac{1}{\omega_r^2} i_n + M_{n-1} C_n i_{n-1} + M_n C_n i_{n+1}\right), \tag{4.2}$$

where $R_{ij} = C_i / C'_j$. All of the cells are designed to work at the same frequency of ω_r, therefore $\omega_r^{-2} = C_n L_n$. The dependency of cell inductance and inverse of capacitance to the cell length have been plotted in Fig. 4.4. It is obvious from the figure that both quantities vary linearly. The capacitance has an inverse relation with cell length i.e. $C_n \propto 1/l_n^c$. In the same way, one can show that the cell inductance is proportional to the cell length i.e. $L_n \propto l_n^c$ and consequently the $L_{n+1} = L_n \frac{l_{n+1}^c}{l_n^c}$. Applying these results and inserting $M_n = k_n\sqrt{L_n L_{n+1}}$ into equation 4.2 yields

$$\left(1 + R_{n(n-1)} + R_{nn}\right)i_n - R_{nn} i_{n+1} - R_{n(n-1)} i_{n-1} = -\omega^2\left(\frac{1}{\omega_r^2} i_n + k_n L_n C_n\sqrt{\frac{l_{n-1}^c}{l_n^c}}\, i_{n-1} + k_{n+1} C_n L_n\sqrt{\frac{l_{n+1}^c}{l_n^c}}\, i_{n+1}\right). \tag{4.3}$$

In our case for DTL Tank1, the $\sqrt{\frac{l_{n-1}^c}{l_n^c}}$ and $\sqrt{\frac{l_{n+1}^c}{l_n^c}}$ values for all cells are distributed less than ± 0.2 % around 1 and in consequence these terms can be approximated by 1. Rewriting the equation 4.3 with $\omega_r^{-2} = C_n L_n = C_{n+1} L_{n+1}$ yields

$$\left(1 + R_{n(n-1)} + R_{nn}\right)i_n - R_{nn} i_{n+1} - R_{n(n-1)} i_{n-1} = -\frac{\omega^2}{\omega_r^2}\left(i_n + k_n i_{n-1} + k_{n+1} i_{n+1}\right). \tag{4.4}$$

Writing the equation 4.4 for all cells yields a generalized eigenvalue system of equations with eigenvalues ω/ω_0. Each of these excited frequencies ω represents a different mode number. For an N cell structure, the N different TM_{01p} modes can be excited.

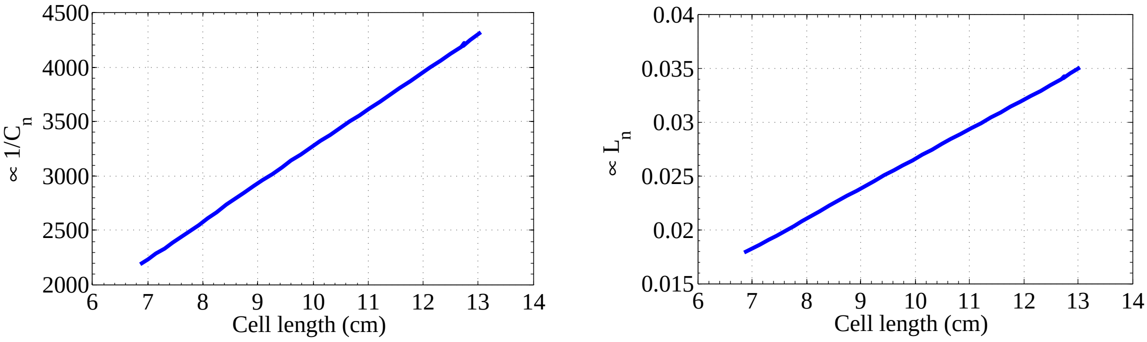

Figure 4.4: The calculated L_p and C_p values versus the cell length. The calculation is done based on SUPERFISH simulation results. It is seen that L_n and C_n have a linear and inverse relationship with cell length.

The first mode $p = 0$ has the lowest excited frequency of ω_0 and the average axial field in all cells is constant i.e. $i_n = i_1$. Applying the constant average axial field in the equation 4.4 yields the $\omega_r^2 = \omega_0^2(1 + k_n + k_{n+1})$. As was discussed, the first and last cells are shorted by metallic covers; therefore R_{10} and R_{NN} are zero. The charges induced on the first drift tube lead to form image charges on the other side of the first metallic cover. Therefore, one can consider an image cell connected to the first accelerating cell with the same current as the first cell. In consequence, the mutual coupling exists between the inductance of image cell and first cell. The same argument is valid for the last cell and $i_N = i_{N+1}$. Finally, the matrix equation representing the cavity is equation 4.5. This equation is a generalized eigenvalue system with the generalized eigenvalues of $(\omega/\omega_0)^2$ and generalized eigenvectors of I.

This generalized eigenvalue problem can be solved numerically. The R_{ij} and k_i are the unknown parameters that should be determined. These unknowns can be found by comparing simulation or measurement results with circuit model output. In Fig. 4.5, the simulated and calculated dispersion curve is plotted for $C'_n = 4.38$ pF and $k = 0$. The C_n values are found by calculating the stored energy and the cell voltage from SUPERFISH results.

The simulated and calculated axial electric field pattern of Tank1 is plotted for the first two modes in Fig. 4.6. It is seen that in the lowest mode, i.e. TM_{010}-mode, both of calculated and measured fields coincide. In the absence of perturbation, the resonance frequency of the cavity is equal to the natural frequency of individual cells. In the equivalent circuit, the stored electric energy in capacitor C_n is totally converted to the magnetic energy in inductance L_n and no part of it can go out of

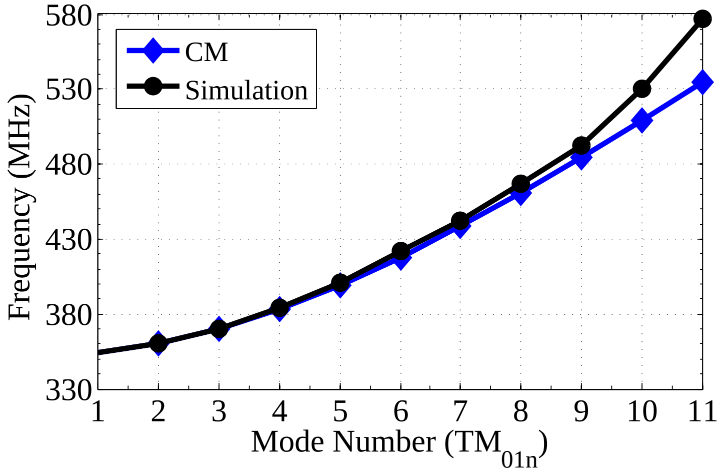

Figure 4.5: Frequency dispersion curve compression of calculated results (by circuit model considering constant C' and $k = 0$) and simulated results (black dot). The calculated and simulated results are in agreement just up to the 7th mode.

the cell impedance. Consequently, the current in coupling branches of circuit model is zero. Unlike the TM_{010}-mode, the circuit model output for the axial field of the TM_{011}-mode does not match with the simulated one. According to Fig. 4.6, the zero of the axial field takes place around the 23th cell in simulated results while it is around the 22th cell in the calculated results. Also, the calculated axial field amplitudes are not consistent with the the simulated values. For the example the error of calculated average axial field of the last cell is 16%.

$$
\begin{bmatrix}
1+R_{11} & -R_{11} & 0 & \dots & 0 \\
-R_{21} & 1+R_{21}+R_{22} & -R_{22} & \dots & 0 \\
\vdots & \vdots & \vdots & \ddots & \vdots \\
0 & \dots & -R_{(N-2)(N-3)} & 1+R_{(N-1)(N-2)}+R_{(N-1)(N-2)} & -R_{(N-1)(N-2)} \\
0 & \dots & 0 & -R_{N(N-1)} & 1+R_{N(N-1)}
\end{bmatrix}
\begin{bmatrix} i_1 \\ i_2 \\ \vdots \\ i_{N-1} \\ i_N \end{bmatrix}
= \frac{\omega^2}{\omega_0^2}
\begin{bmatrix}
\frac{1+k_0}{1+k_0+k_1} & \frac{k_1}{1+k_0+k_1} & 0 & \dots & 0 \\
\frac{k_1}{1+k_1+k_2} & \frac{1}{1+k_1+k_2} & \frac{k_2}{1+k_1+k_2} & \dots & 0 \\
\vdots & \vdots & \vdots & \ddots & \vdots \\
0 & \dots & \frac{k_{N-2}}{1+k_{N-1}+k_{N-2}} & \frac{1}{1+k_{N-1}+k_{N-2}} & \frac{k_{N-1}}{1+k_{N-2}+k_{N-1}} \\
0 & \dots & 0 & \frac{k_{N-1}}{1+k_{N-1}+k_N} & \frac{1+k_{N+1}}{1+k_{N-1}+k_N}
\end{bmatrix}
\begin{bmatrix} i_1 \\ i_2 \\ \vdots \\ i_{N-1} \\ i_N \end{bmatrix}
\tag{4.5}
$$

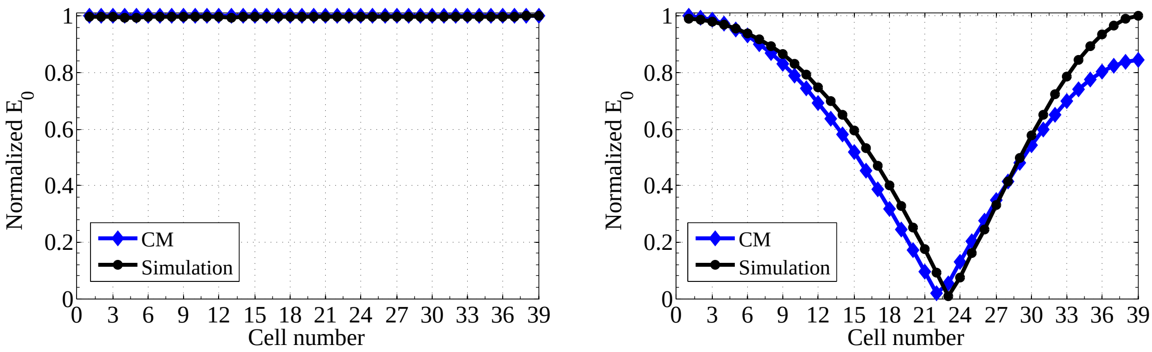

Figure 4.6: Comparison of simulated and calculated average axial field considering a constant C' for all cells.

The coupling capacitance of each cell can be approximated by a simple coaxial cable [61]. The capacitance of coaxial cable is

$$C_{coax} = \left(\frac{2\pi\epsilon_0\epsilon_r}{\ln(r_2/r_1)}\right)l_{coax}, \tag{4.6}$$

where the l_{coax} is the length of cable and ϵ_r is the relative dielectric constant. The inner and outer radius are r_1 and r_2, respectively. The coupling capacitance increases linearly as the coaxial length increases. Therefore the calculations should be done considering non-uniform coupling capacitances. With analogy to the simple coaxial cable, C' is considered as a linear function of the cell length, i.e. $C' = (al_n + b)C_1$. Where l_n is the length of n^{th} cell and C_1 is the capacitance of the first cell. a and b are the parameters that should be determined by comparing simulated and calculated axial fields of the TM_{011}-mode. For Tank1, C_1, a and b are 4.56 pF, 1.22 and -1, respectively. By applying this correction on C', the calculated axial fields of the TM_{011}-mode is plotted in Fig 4.7 (black triangles). The solid red line in the figure represents the simulated result. According to these results, by applying the length dependent C', the calculated axial field of the TM_{011}-mode coincides with the simulated one.

As is shown in the Fig 4.7, the calculated axial field of the higher order modes using a circuit model deviates from the simulated one. As an example for the Seventeenth cell, the error of calculated average axial field are 9% and 43% for the TM_{015}-mode and TM_{017}-mode, respectively. In the dispersion curve shown in Fig. 4.8, it is seen that the calculated dispersion curve (blue diamonds) coincides with the simulated results up to around n=7. From the Fig. 4.8, the calculated frequencies of the last four modes i.e. TM_{018}, TM_{019}, $TM_{01(10)}$ and $TM_{01(11)}$ are respectively 2.0%, 2.2%, 4.0% and 8.0% different respect to the simulation.

So far, the circuit model calculation is done without considering the mutual inductance between accelerating cells. By considering a mutual inductance coefficient of $k = 0.058$, the error of the calculated frequencies for the TM_{018}, TM_{019}, $TM_{01(10)}$ and $TM_{01(11)}$ modes are 0.1%, 0.2%, 1.9% and 5.4%, respectively. Therefore by considering the contribution of mutual inductance, the circuit model can predict the higher order mode frequencies up to the ninth mode. Furthermore, as is shown in Fig. 4.7, the calculated axial fields (blue dot) are closer to the simulated results even up to the TM_{017}. Again for the seventieth cell and by considering the mutual inductance, the error of calculated average axial field is around 1.5% and 8% for the TM_{015}-mode and TM_{017}-mode, respectively.

4.2 Tilt-sensitivity measurements

The tilt-sensitivity (TS) is a parameter that determines the sensitivity level of the axial field in a perturbed DTL cavity. The TS is

$$TS_n = \frac{1}{\Delta f}(E_{0n}^{he} - E_{0n}^{le}). \tag{4.7}$$

Where E_{0n}^{he} and E_{0n}^{le} refer to axial field values of the n^{th} cell in the case of perturbing at the high and low energy end respectively. The TS returns the sensitivity level of each cell individually and makes it possible to investigate the axial electric field stability of each cell individually. Also it is shown experimentally that the TS varies linearly as perturbation amount changes [62]. The other characteristic of TS is that it describes the sensitivity level per unit of frequency perturbation and it is easier to compare sensitivity level of different perturbation.

For the simple 20 cells structure that discussed in 4.1.1, the TS and its derivative are plotted in Fig 4.9. As is shown in the figure, the derivative of TS is constant and consequently the sensitivity level for all cells are the same.

It is worthwhile to note that the procedure of TS measurements in the present work is slightly different than the traditional one. In the traditional approach, the TS is measured by counter-perturbing the cavity on either end. First the resonant frequency is lowered by Δf by decreasing the first cell's gap length. Afterwards, the resonant frequency is restored to the initial value by adjusting the gap at the other end of the tank. The electric fields along the axis are measured by the bead-pull method and this measured axial field is marked as E_n^{le}. Repeating the same

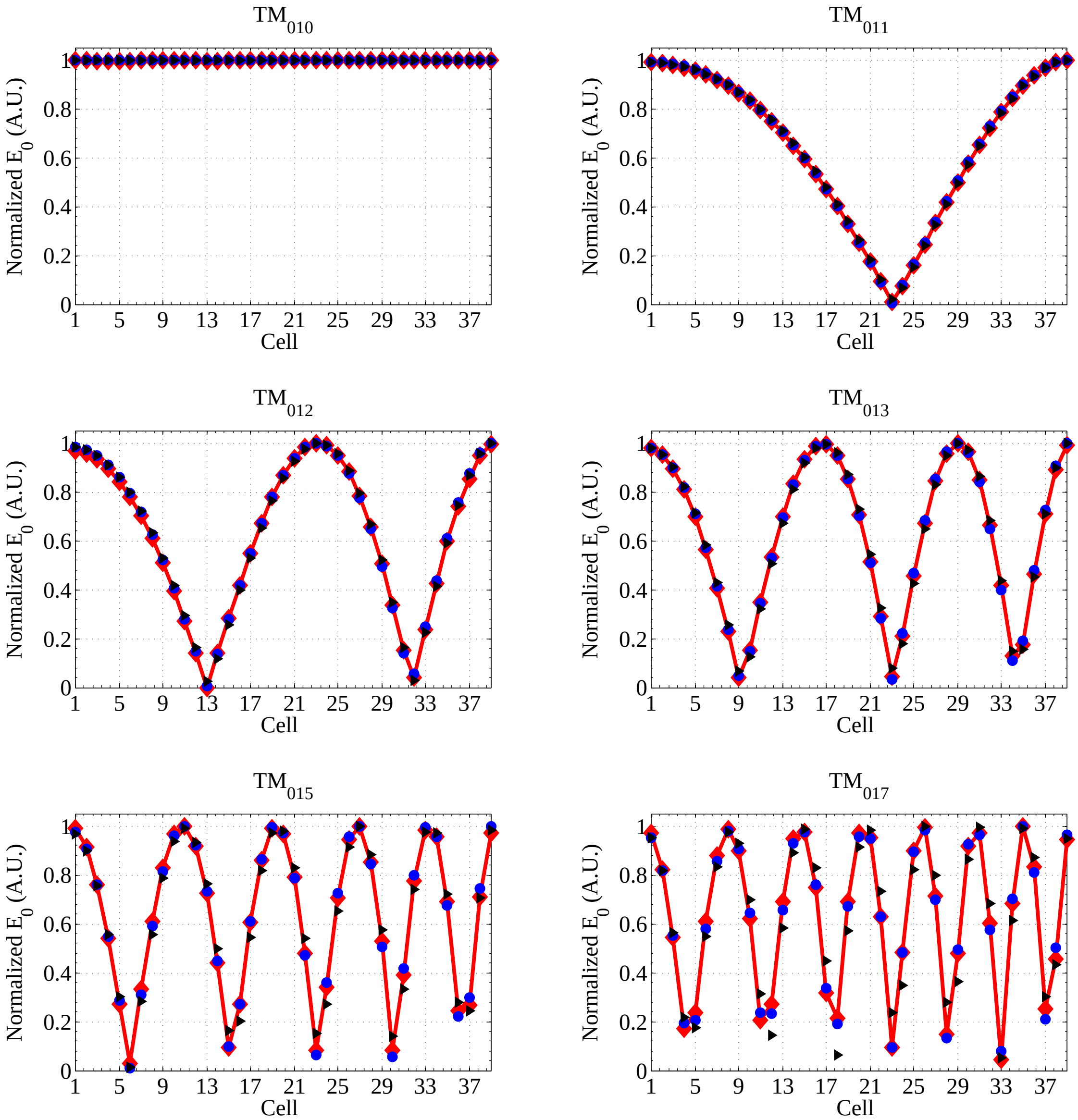

Figure 4.7: The comparison of simulated axial field (red line) and calculated results considering the increasing cell length effect on C' (black triangles) and the first mutual inductance (blue dot) up to seventh mode. The calculations show that by considering the increasing cell length effect on C', the axial fields of TM_{011} are fitted with simulated values.

procedure starting from the high energy end yields the E_n^{he}. Subtracting the fields of these two measurements divided by frequency perturbation Δf yields the TS value.

In the modified technique, the initial resonance frequency should be adjusted so that TM_{010}-mode frequency gets slightly higher than the operation frequency ω_{op}. Then the DTL is perturbed to the ω_{op} by perturbing one of the end gaps. Here, the

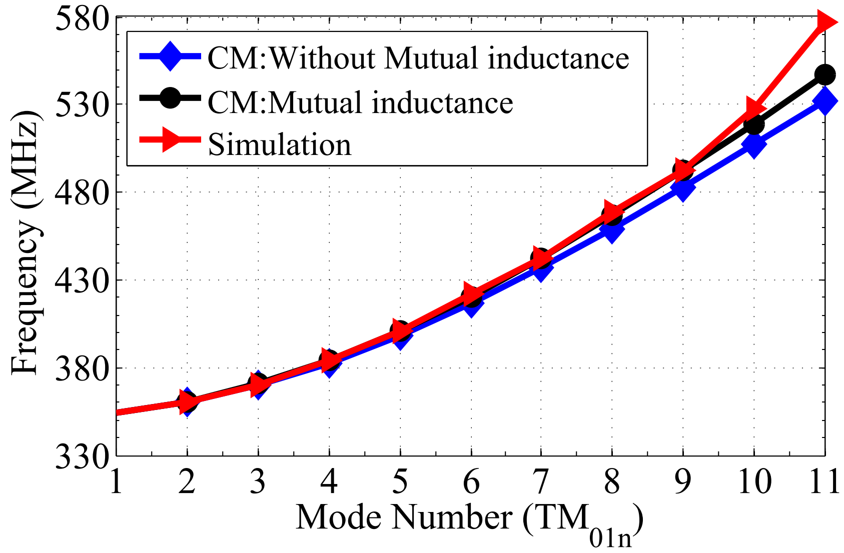

Figure 4.8: The comparison of simulated dispersion curve (solid red line) and calculated results considering the increasing cell length effect on C' and first mutual inductance up to the first 10 modes.

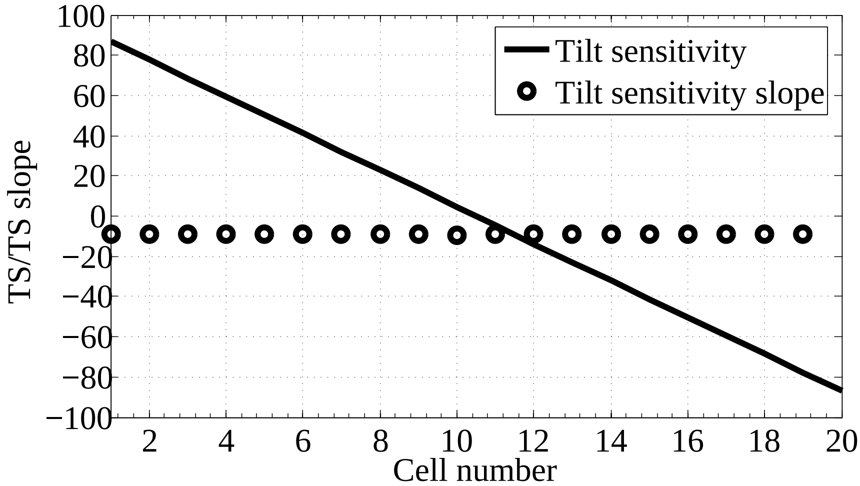

Figure 4.9: The typical tilt-sensitivity of calculated axial field of Fig. 4.3 with 20 identical cells. The dot represents the slope of tilt-sensitivity. As it is expected in this case of same cells structure, all cells have the same sensitivity level.

modified TS approach is used intentionally rather the traditional one because of two reasons. The first is that in the traditional definition, especial mechanical means are needed to change the ends gaps whereas in the modified definition, a simple hollow metallic pipe is used to perturb the first and the last gaps. The second one is that in the traditional measurements, the frequency should be adjusted four times for each

TS measurements, but in the modified approach it is reduced to two adjustments and this leads to a decrease in measurement time.

In order to verify consistency of the modified and traditional TS procedure, SUPERFISH simulation of DTL Tank1 is used. In the traditional case, the resonant frequency of the accelerating mode is 350.123 MHz and the cavity is perturbed from either side by about 110 kHz and then the frequency is restored to the initial value by counter perturbing the opposite end cell. To calculate the TS using the modified technique, the cavity is initially perturbed to 350.233 and then by perturbing the gap of the first cell, the frequency returns to 350.123 MHz. The TS measured by both procedures are shown in 4.10. Though the perturbations are different in each procedure, the simulation results reveal that the TS of both cases are in good agreement provided the TSs are measured at the same frequency, for example in this simulation 352.123 MHz. In the present work, the modified approach is used to measure the TS.

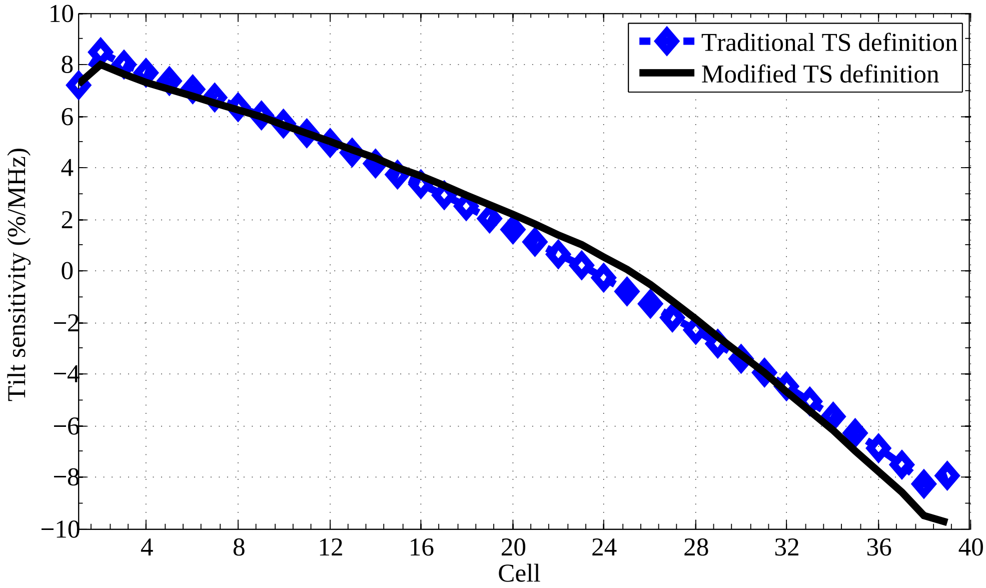

Figure 4.10: Comparison of traditional and modified procedures of tilt-sensitivity measurements using SUPERFISH simulations.

4.3 Theory of stabilization

It has been discussed that the susceptibility of the axial field to perturbation errors may seriously affect beam quality. The susceptibility of the axial field is a consequence of coupling between cells. This coupling consists of a capacitor C'_n and an inductor L'_n in parallel. The C'_n and L'_n depend on the geometry and the resonance frequency of the structure. From the equivalent circuit model, the axial field sensitivity reduces as coupling admittance $Y_n(C'_n, L'_n)$ tend to zero. In DTL cavities, instead of changing the C'_n and L'_n, some extra coupling elements can be added to the coupling admittance to adjust it. In this case, the additional elements are chosen so that the Y'_n gets zero. In the present work, the prime index is used to distinguish between the pure cell admittance without extra coupling elements Y_n and with extra coupling elements Y'_n.

The concept of axial field sensitivity of an accelerating cavities can be expressed in terms of a chain of coupled resonators (Fig. 4.11). In terminology, such coupled structures are known as the alternating or bi-periodic structure [63, 64].

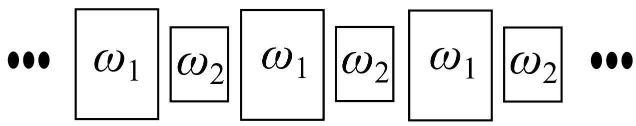

Figure 4.11: A schematic view of Bi-periodic structure

Generally speaking, a single cell of DTL can be modeled as series impedances Z_n coupled with the parallel admittance of Y_n. For sake of simplicity in calculations, let us assume an array of infinite number of identical accelerating cells. The current and voltage at each node can be considered using Floquet theorem as is shown in Fig. 4.12. Then the voltage equation can be written as follows

$$V_0 \exp(-j\phi) - V_0 = ZI_0, \tag{4.8}$$

$$I_0 - I_0 \exp(j\phi) = YV_0. \tag{4.9}$$

These two equations can be merged by eliminating the V_0/I_0 and therefore it yields

$$(\exp(j\phi) - 1)(\exp(-j\phi) - 1) = -YZ \rightarrow$$
$$4(\sin^2(\phi/2)) = -YZ.$$

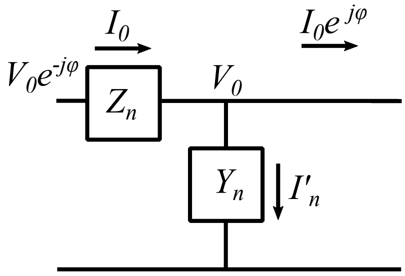

Figure 4.12: The current and voltage at each node of a periodic structure.

For the case without stem, $Y = j\omega C'$ and $Z = (j\omega C)^{-1}(1-(\omega/\omega_0)^2)$. In consequence, the equation 4.10 can be written as

$$4\sin^2(\phi/2) = -\frac{C'}{C}(1-(\omega/\omega_0)^2) \tag{4.10}$$

By considering C/C'= {0.5, 1.0 and 2.0 } and ω_0=352.2 MHz, the dispersion curves of the whole structure are plotted in Fig. 4.13. By increasing the ratio of C/C', the resonance frequency of the π-mode increases from 600 to 1050 MHz.

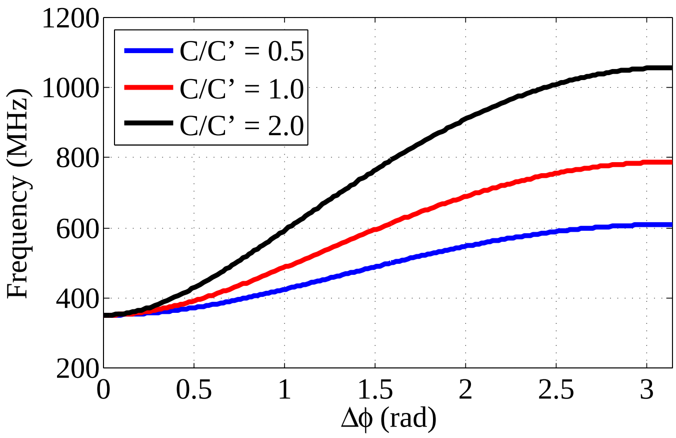

Figure 4.13: The calculated dispersion curves of an arbitrary single-stem structure using equation 4.10 and for three different coupling values (C/C').

In the realistic case, drift tubes are held by stems. Considering an stem for each drift tube, a parallel inductance is formed between drift tube and cavity wall, therefore the $Y = j\omega C' + (1/j\omega L')$. Here, the coupling admittance can be considered as a second resonator which resonates at $\omega' = 1/(C'L')$. By applying the new Y into the equation 4.10, the new relation between phase difference and excited resonance frequency is obtained

$$4\sin^2(\phi/2) = -\frac{1}{\omega^2 L'C}(1-(\omega/\omega_0)^2)(1-(\omega/\omega')^2) \tag{4.11}$$

The dispersion curve of a typical infinite DTL structure with identical cells and a single stem per drift tube is calculated using equation 4.11 (Fig. 4.14). In these calculations, the ω_0, ω' and $L'C$ are assumed 352.2 MHz, 180 MHz and 1.5×10^{-3} s^2 respectively. Here, the stems and TM_{010} pass-band are separated at $\Delta\phi = 0$ with a relatively wide stop-band of 170 MHz and the group velocity of TM_{010} modes is zero.

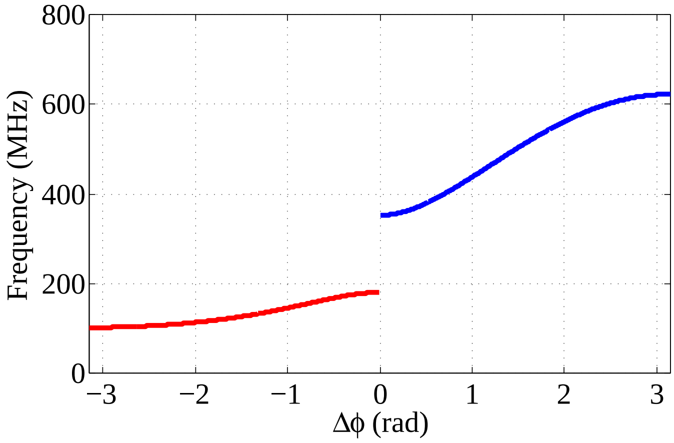

Figure 4.14: A calculated dispersion curve of an arbitrary multiplestem structure using equation 4.12.

Using circuit model analysis, it is possible to show that by adjusting the coupled resonator, the axial field sensitivity with respect to the tuning errors increases. The stability increases when the group velocity of the TM_{010}-mode increases from zero and the stop-band decreases [63]. The two techniques to improve axial field stability of a DTL cavity are mounting multiplestems and post-couplers. The schematic side view of one, two, three stems and the post-coupled structure are shown in Fig. 4.15. The first proposal of using multiplestems has been introduced by S. Giordano in 1966 [65] and the idea of stabilizing axial field using post-coupler has been presented in 1967 by Swenson et al. [66]. In the following, the physical concept of these two approaches are discussed in detail but the main focus of next chapters is on post-couplers because all Linac4 DTL structures is equipped with them.

4.3.1 Multiplestem structures

The equivalent circuit of single and double stems structures are shown in Fig. 4.16. In case of a single stem, the coupling capacitance C' is in parallel with inductance of the supporting stem L' so that they resonate at $\omega' = (L'C')^{-1/2}$. The resonance frequency of a single stem is far away from the natural frequency of the accelerating

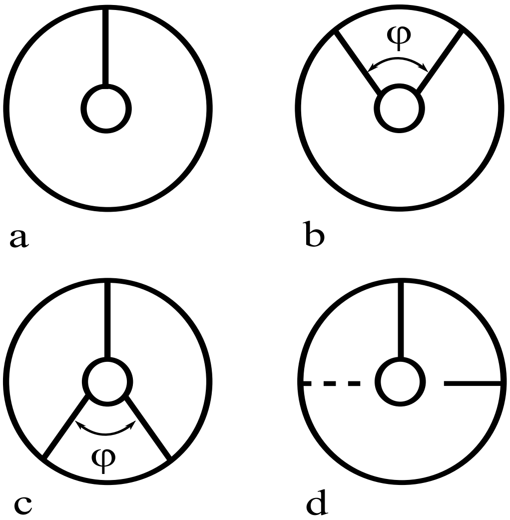

Figure 4.15: The side view of DTL cavity equipped with a) one stem, b) two stems, c) three stems and d) The side view of a post coupled structure. Since the adjacent post-coupler azimuthal direction alternates 180 degrees, the left hand side post-coupler is shown using dashed line.

cell. For example, the stems of the BNL DTL resonate at around 300 MHz while the intrinsic resonance frequency of the accelerating cells is about 850 MHz [67]. The equivalent impedance of a single stem is

$$Y' = \frac{1}{Z'} = \left(j\omega C' + \frac{1}{j\omega L'} \right) = j\omega C' \left(1 - \frac{\omega'^2}{\omega^2} \right) \tag{4.12}$$

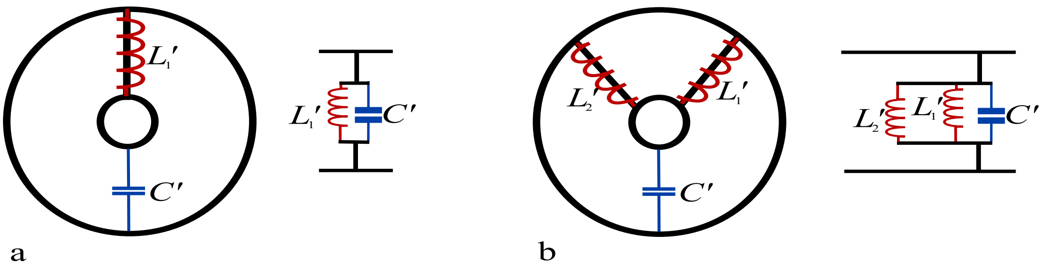

Figure 4.16: The side view and equivalent circuit model of single stem and double stems DTL.

C' depends on the geometry of the structure and it is assumed that mounting extra stems, slightly perturbs the electromagnetic field inside the cell. Stems have not particular influence on C'. As the second stem is installed, an additional inductance L_2' adds to the coupling admittance (Fig. 4.16) and consequently the equivalent inductance is

$$L'_{eq} = \frac{L'_1 L'_2}{L'_1 + L'_2} \tag{4.13}$$

Assume that both stems have the same thickness and the same inductance i.e. $L'_1 = L'_2$, then the equation 4.13 indicates that the equivalent inductance in the case of double stems is always lower than a single stem. Therefore, the resonance frequency of coupling admittance increases. The dispersion curve of N_s stems structure are calculated using equation 4.10. The input parameters are chosen as it was in the last example. The equivalent inductance L'_{eq} and ω'_{eq} are L'/N_s and $\omega'\sqrt{N_s}$. The calculation results are brought in Fig. 4.17. In the figure, having two stems reduces the stop-band to around 100 MHz but the group velocity remain zero. As shown in the figure, the stop-band is around 30 MHz for the case of a three stems structure. Finally, in this particular case of a four stem structure, the stems and TM pass-band confluences and the group velocity of the accelerating mode is increased. Mutual coupling between multiplestems is ignored in this calculations.

This behavior of muliplestems pass-bands is seen experimentally. The measured dispersion curve of the BNL DTL structure reported by [65], is shown in Fig 4.18. According to the measurement results, by increasing number of stems, the stem pass-band goes toward higher frequencies. Also in the figure, the group velocity of the TM_{010} is increased as the stem count is increased and therefore a better stabilization is expected.

Although it is possible to reduce the axial field sensitivity by mounting multiplestems in the structure, there are critical disadvantages that make multiplestems inefficient. For instance, the experimental data shows that the energy loss in multiplestems structures is not negligible [68]. Furthermore the mechanical complexity of such structures is another practical issue. Because of increasing cell length, the local multiplestems resonance frequency decreases from the low energy end to the high energy end of the DTL, so one should compensate the local frequency by regulating the stem diameters. Such consideration and difficulties lead the Los Alamos group to invent post-couplers.

4.3.2 Post-couplers

Post-coupler is the the cylindrical rod which can be used to stabilize axial field. Post-couplers are mounted in the cylindrical wall of a DTL and are extended toward the drift tube without touching the drift tube surface. In order to widen the post-coupler pass-band, the post-couplers alternate 180° azimuthally every drift tube as is shown

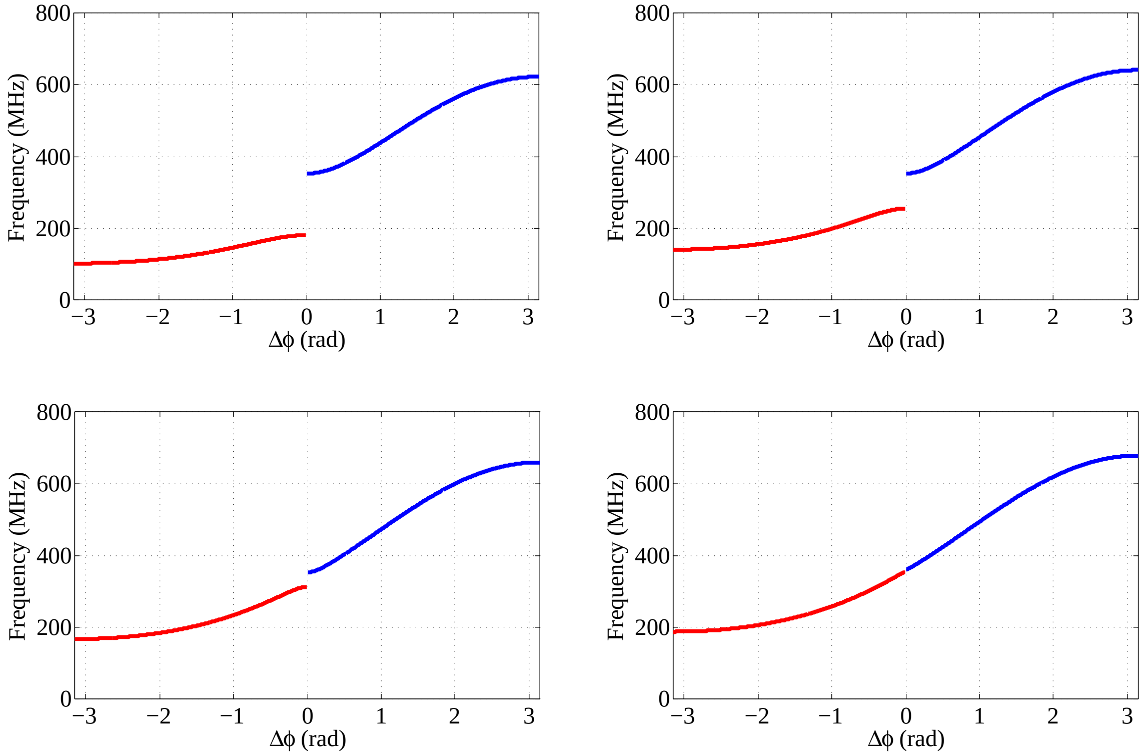

Figure 4.17: The calculated dispersion curves of an arbitrary multiplestem structure using equation 4.12. As is seen, in the case of a single stem (Top left plot) accelerating and stems pass-band are separated with a remarkable stop-band. This stop-band is reduced by considering 2 stems (Top right) and 3 stems (Bottom left plot). Finally the confluence with non-zero group velocity is seen for case of 4 stems (Bottom right plot).

in Fig. 4.19. Like the multiplestem structure, the post-coupler has no effect on unperturbed TM_{010}'s axial fields and they get excited only in case of having perturbations.

The coupling between posts is not as strong as it is in the case of multiplestems and this fact could be seen by comparing the group velocity of a multiplestem structure with a post-coupled structure. For instance, the dispersion curve of 92.7 MeV Los Alamos proton DTL equipped with four stems at confluence and 55 MeV post-coupled structure is plotted in Fig. 4.20. From the figure, the group velocity v_g of TM_{010} mode is $0.35c$ while it is $0.09c$ for post-coupled structure. However, even in post-coupled structure, the group velocity is still large enough to have a good axial field stability [68].

In contrast to the multiplestem structures, the manufacturing of post-couplers is simpler than of multiplestems structure and less power is wasted on their surfaces.

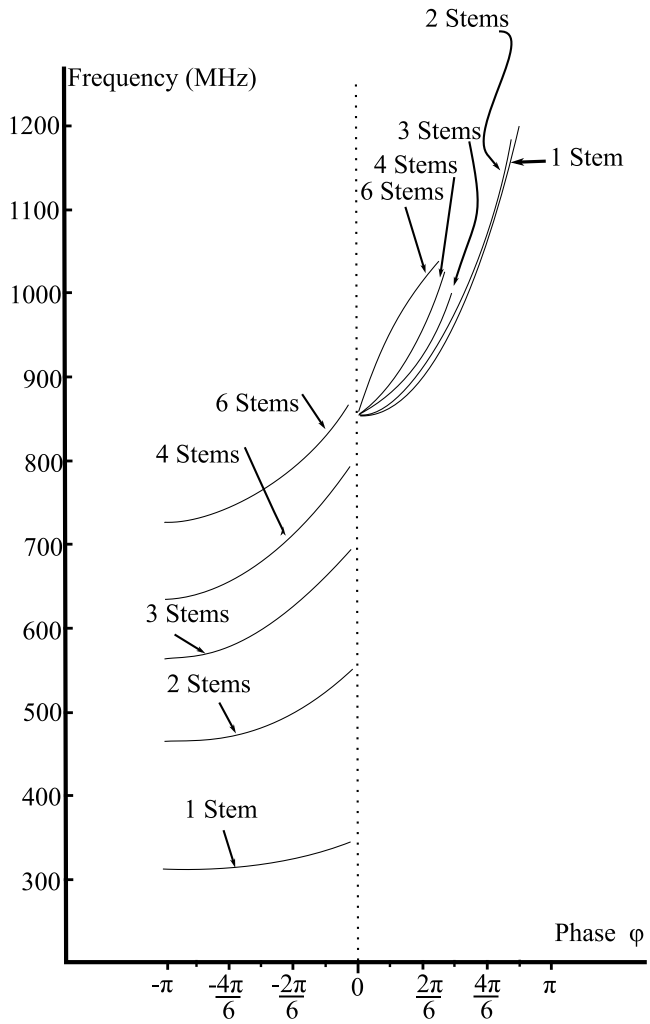

Figure 4.18: The measured dispersion curve of BNL multiplestem DTL structure. It is clear from the figure, the stems pass-band resonant frequency increases as the number of stems increases and lower axial field sensitivity with respect to error is expected [65].

This is due to the fact that usually the post-coupler thickness is smaller than a single stem. As discussed, the stem thickness should be adjusted as cell length increases to maintain the local stem resonant frequency constant. For a post-coupled structure, in addition to changing the thickness, it is possible to adjust the post-coupler length to achieve the desired stabilized condition. In consequence it is more convenient to adjust a post-coupler compared to the multiplestem cavity.

The equivalent circuit model representation of a post-coupled structure (Fig. 4.21) is proposed by Nishikava [65]. Here the post-coupler can be modeled by a series

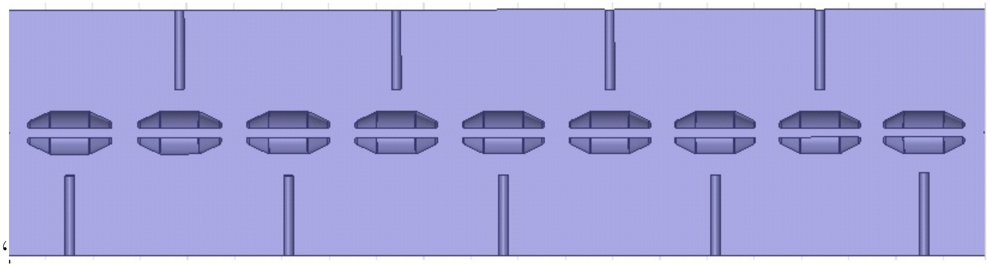

Figure 4.19: A equatorial plane view of post-coupled structure.

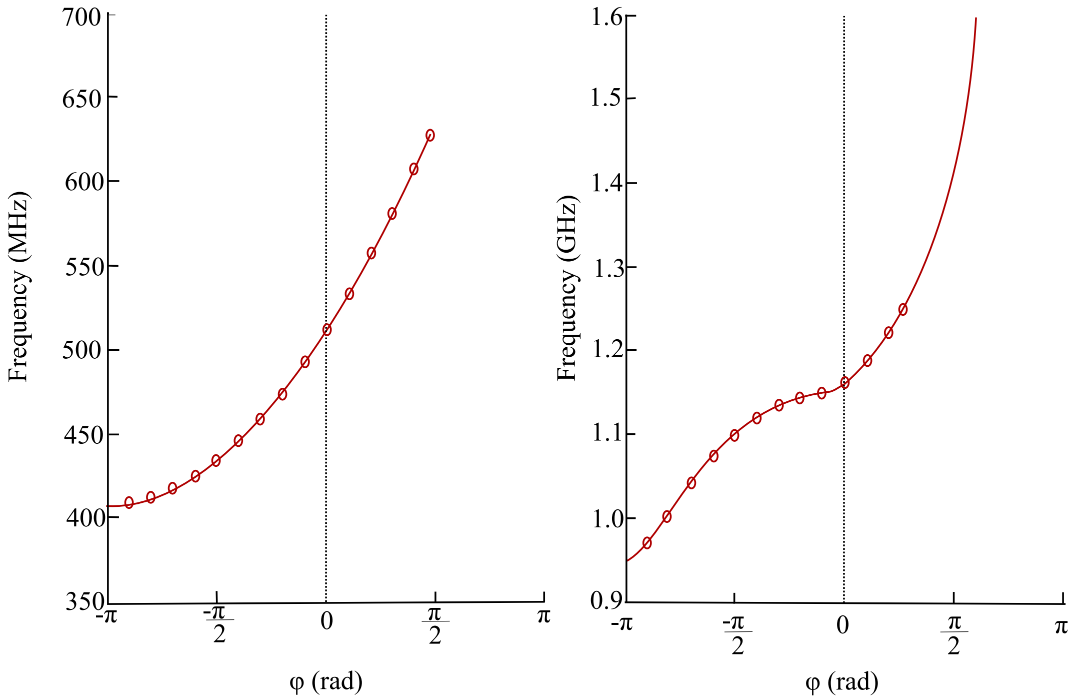

Figure 4.20: Comparison of dispersion curve of 92.7 MeV Los Alamos proton DTL equipped with 4 stems at confluence and a 55 MeV post-coupled structure [68].

capacitance C'' and inductance L''. In the present work, it is assumed that the L'' and C'' depend on the geometry of the post-coupler and the mutual inductance of the two next post-couplers is negligible. Therefore, by changing the post-coupler length, one can adjust the C'', L'' and ω''. It had shown in previous work that the post-couplers have a negligible effect on the nominal accelerating field and the TM_{010} frequency shift of DTL due to presence of a post-coupler can be approximated by using Slater perturbation theorem. Note that when the post-coupler pass-band crosses the

TM-mode pass-band, the resonance frequency shift can not be approximated by using Slater perturbation theorem [59].

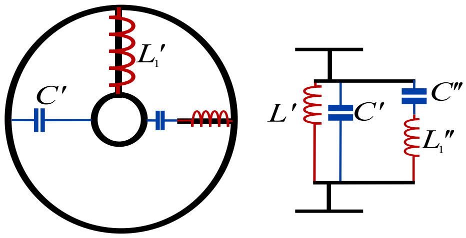

Figure 4.21: A shematic front view of a post coupled structure and the equivalent circuit representation of coupling admitance Y_n.

Chapter 5

Post-coupler stabilization strategies

5.1 Introduction

At the beginning of this chapter, the recent procedure on DTL stabilization by using post-coupler will be reviewed briefly and the assumptions and practical limitations of these DTL stabilization strategies will be reviewed. After this review, a new stabilization strategy is defined analytically by using equivalent circuit model. Finally, the post-coupler characteristic and electromagnetic field distribution in DTL cavities are studied by the mean of 3D simulations.

5.2 Recent stabilization procedures

5.2.1 Distortion parameter

The distortion parameter is a parameter which describes the stability level of an entire DTL structure. This parameter is defined as

$$D_x = \sum_{n=1}^{N} E_n^p - E_n^u, \tag{5.1}$$

where E_n^p is the perturbed normalized average axial field and E_n^u is the unperturbed normalized average axial field of the n^{th} cell. x represents the length of post-couplers, and N is the total cell number. The perturbation is applied from one side of DTL cavity and the resonance frequency of the cavity is restored to the unperturbed resonance frequency by counter-perturbing the other sides. The minimum of D_x corresponds to higher field stability with respect to perturbation.

D_x measurements have been used to stabilize DTL cavities in several projects for example [69–72]. In these works, lengths of all post-couplers are varied uniformly in each step and the D_x is calculated from the measured axial field. These measurement returns a post-coupler length with better field stability than the case of no post-couplers. For example, the measured distortion parameters on a nine cells DTL Tank of Kyoto University [73] is shown in Fig. 5.1. According to this result, minimum distortion is achieved when the post-coupler length is around 14.5 cm. However to have the best stabilization, the post-coupler lengths are certainly not equal, and they should vary to compensate the effect of increasing cell length. In the mentioned reports [69–72], there is not enough information about the procedure of the further adjustment. One possible method is to adjust post-couplers by trial and error and minimizing D_x. This procedure usually requires a considerable amount of time.

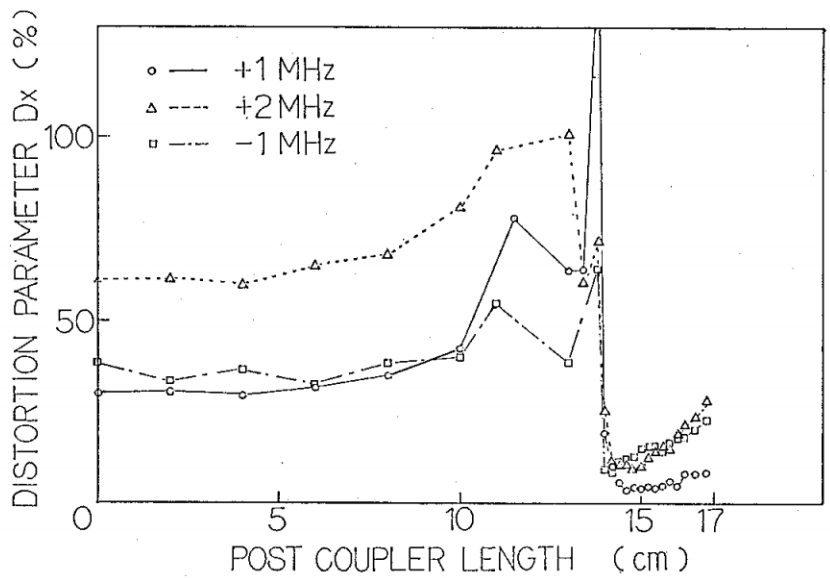

Figure 5.1: The measured distortion parameters on a nine cells DTL Tank of Kyoto University [73].

5.2.2 Tilt-sensitivity

In the previous chapter, it was discussed that the TS optimization is another method to measure axial field stability level of DTL cavities. The zero slope of TS represents the best adjustment of post-couplers. Like the distortion parameter, this method is used for DTL stabilization in the different project [57, 74].

The one practical procedure here is based on finding the proper initial length using dispersion curve and afterwards try lots of random solutions around the initial length to find out the most stable axial field.

5.2.3 Circuit model analysis

In 1985, Machida et al. performed analytical calculations to understand the post-coupler behavior. Their investigation deduces a tilt parameter T which expresses the level of axial field instability in DTL. Lower T leads to better stabilization. The calculated T for three cells DTL is

$$T \propto \frac{k_0 + 1}{Z'_n}, \tag{5.2}$$

where $k_0 = M_0/L_0$ and Z'_n is the impedance of the coupling elements. L_0 and M_0 are the self and mutual inductance of the accelerating cell [70]. Their paper provided a good explanation about some physics of stabilization but the further investigation stopped.

5.2.4 Uniform post-coupler resonant frequency method

In 1990, a strategy to find out the proper post-coupler length is reported by Natio et al. for a 432 MHz cold model DTL of the Japanese Hadron Project injector [69]. Their proposal was to set post-couplers at the same length L_i so that the post-coupler passband goes down with respect to the TM passband. Then by moving just the i^{th} post-coupler, they found the length at which that post-coupler was at resonance. By repeating this procedure for different initial length L_i, they made a table of post-couplers resonance length as a function of its initial length. Using this information, they calculated the length of each post-coupler so that the resonance frequency of all post-couplers were the same. Using this approach, they reduced the non-stabilized $D_x = 3.6 \times 10^{-3}$ by a factor of 2.4. In their paper, it is mentioned that with increasing the total number of post-couplers, the minimum distortion parameters gets even higher and the stability of average axial field with respect to perturbation decreases. In the next chapter, it will be discussed that increasing the number of post-couplers increases the stability of average axial electric field with respect to the perturbation.

5.2.5 Fitting the frequency dispersion

The recent technique for DTL stabilization is reported in 2012 by F.Grespan [75]. In this technique, the capacitances and resonance frequencies of accelerating cells are obtained directly using SUPERFISH simulations. In the next step, the coupling capacitance is calculated by fitting the calculated dispersion curve with the experimental one. Then, by comparing the calculated and the measured post-coupler pass-band, the C'', L'' and the mutual coupling between post-couplers is obtained. By knowing the value of circuit elements, it is possible to calculate TS as a function of post-couplers length and these calculations yield the optimum post-coupler length.

In this work, it is assumed that the cells are identical and consequently all C' are equal. This approximation is made to reduce the complexity of finding C' of increasing cell length structure. A second approximation is that the resonant characteristic of all coupling admittance with same length are equal. In this procedure, the circuit model returns an approximate initial length for all post-couplers. In consequence, the further adjustment is needed to improve axial field stability. TS before stabilization was reported in the range of [-0.2,+0.2] MHz^{-1}. By using this procedure, the TS of CERN Linac4 cold model was reduced down to [-0.05,+0.1] MHz^{-1}.

5.3 Post-coupler analysis using circuit model

The effect of perturbations on the non-stabilized field was discussed in section 4.1.1 and it was shown how perturbations create a tilt in the axial field. Furthermore, recent attempts on DTLs stabilization were discussed at the beginning of the present chapter. In this section, the physical concepts of axial field stabilization by using post-couplers will be studied in detail by using equivalent circuit model.

5.3.1 The tilt-sensitivity slope definition

The equivalent circuit for DTLs (Fig. 4.21) can be written in terms of a coupling admittance $Y'_n(\omega, C'_n, L'_n, L''_n, C''_n)$ and the circuit representation of each accelerating cell can be written in terms of an equivalent impedance $Z_n(\omega, L_n, C_n)$. Here C_n, L_n, C'_n and L'_n depend on the structure geometry, drift tube shape and gap length. On the other hand, it has been discussed that the L''_n and C''_n magnitudes depend on the post-coupler length l''_n. The cell impedance and coupling admittance of the n^{th} cell are

$$Z_n = j\omega L_n + \frac{1}{j\omega C_n} \tag{5.3}$$

$$Y'_n = j\omega C'_n + \frac{1}{j\omega L'_n} + \frac{j\omega C''_n}{1 - \omega^2 L''_n C''_n} \tag{5.4}$$

By applying Kirchhoff's voltage law to the equivalent circuit that is terminated by a short circuit at either end and ignoring the cell inductance L_n, the following set of equations can be derived (Fig. 4.2)

$$
\begin{aligned}
&Z_1 I_1 + \frac{I_1 - I_2}{Y_1'} = 0 \\
&\qquad\vdots \\
&Z_n I_n + \frac{I_n - I_{n+1}}{Y_n'} - \frac{I_{n-1} - I_n}{Y_{n-1}'} = 0 \\
&Z_{n+1} I_{n+1} + \frac{I_{n+1} - I_{n+2}}{Y_{n+1}'} - \frac{I_n - I_{n+1}}{Y_n'} = 0 \\
&\qquad\vdots \\
&Z_N I_N - \frac{I_{N-1} - I_N}{Y_{N-1}'} = 0.
\end{aligned}
\tag{5.5}
$$

The series of equation 5.5 describe the axial field and resonance frequencies of a DTL structure. It is not convenient to study the whole structure considering all of the higher order modes using these equations because in this case all of the circuit elements magnitudes should be determined precisely at the beginning and this requires spending times. Instead, it is more convenient to study the structure locally at a single operation mode. Since the axial field sensitivity to the perturbation is of interest in our measurements, the TS measurement could be good criteria to start. Note that the TS is defined in equation 4.7. Also, the index le is used to describe the axial fields in the case that the first gap at the low-energy end is perturbed. Similarly he refers to the case of perturbing the high-energy end. Also note that it is essential that the perturbation measurements are undertaken at the same operating frequency i.e. $\omega^{he} = \omega^{le} = \omega_{op}$.

Rewriting Kirchhoff's voltage law for the n^{th} cell (5.5) for the case of high-energy end perturbation and the $(n+1)^{\text{th}}$ cell for low-energy end perturbation, moving terms of Y_n' to the right-hand side, and adding these two equations yields

$$
Z_n I_n^{he} + Z_{n+1} I_{n+1}^{le} - \frac{I_{n-1}^{he} - I_n^{he}}{Y_{n-1}'} + \frac{I_{n+1}^{le} - I_{n+2}^{le}}{Y_{n+1}'} = -\frac{I_n^{he} - I_{n+1}^{he} - I_n^{le} + I_{n+1}^{le}}{Y_n'}. \tag{5.6}
$$

For the following, consider that the axial field are measured for different penetration of the n^{th} post-coupler and that moving post-couplers has negligible effect on C_n, and L_n, while C_n'' and thus the coupling admittance Y_n' is a function of l_n''. Since the frequency is kept constant at $\omega = \omega_{op}$, perturbing the high-energy end changes Z_N while the rest of the circuit elements do not change.

As can be derived recursively from the system of equations (5.5), regardless of Y'_n, the current ratios I_n^{he}/I_1^{he} and I_{n-1}^{he}/I_1^{he} are independent of the perturbation. When the reference current I_1^{he} is kept constant over all measurements, on the left-hand side thus $Z_n I_n^{he} - (I_{n-1}^{he} - I_n^{he})/Y'_{n-1} = \text{const}$. In the same way, for a low-energy end perturbation, when I_N^{le} is kept constant, also $Z_{n+1} I_{n+1}^{le} - (I_{n+2}^{le} - I_{n+1}^{le})/Y'_{n+1} = \text{const}$. The left-hand side of equation (5.6) therefore remains constant regardless of the n^{th} post-coupler length and the numerator of the right-hand side becomes proportional to the admittance Y'_n

$$I_n^{le} - I_n^{he} - I_{n+1}^{le} + I_{n+1}^{he} \propto Y'_n. \tag{5.7}$$

Substituting the normalized average axial field $E_{0n} = U_n/l_n/\bar{E}_0$ in the gap with the normalization $\bar{E}_0 = U_{tot}/l_{tot} = \sum_n E_{0n} l_n / \sum_n l_n$ is applied into equation 5.7. Introducing this reference via the relation $I_n = j\omega C_n U_n$ in (5.7), and rewriting it in terms of TS_n (4.7) yields

$$C_{n+1} l_{n+1} \,\text{TS}_{n+1} - C_n l_n \,\text{TS}_n \propto Y'_n \tag{5.8}$$

With the stored energy $U_n^2 C_n/2$ approximately proportional to the cell length l_n, and with the accelerating gradient $E_{0n} = U_n/l_n/\bar{E}_0$ constant over all cells of a DTL as usually the case, $C_n l_n \approx \text{const}$ over all cells. Simplifying (7) with this approximation gives

$$\Delta\text{TS}_n = \text{TS}_{n+1} - \text{TS}_n \propto Y'_n. \tag{5.9}$$

The new parameter ΔTS_n when divided either by the length of the structure or the number of cells between the two TS values, can be understood as the local tilt-sensitivity slope (TS′). Writing out Y'_n, the TS′ can now be analyzed in more details

$$\text{TS}'_n \propto \left(j\omega C'_n + \frac{1}{j\omega L'_n} \right) + \frac{j\omega C''_n}{1 - \omega^2 L''_n C''_n}. \tag{5.10}$$

Moving post-couplers has a negligible effect on the electromagnetic field distribution in the rest of the cell. Therefore variation of C'_n and L'_n is negligible and since the resonance frequency is always kept at ω_{op}, the terms in parentheses are approximately constant. It is discussed that 3D simulations show that the inductance of the post-coupler L''_n is approximately constant for the different post-coupler/DT gap. The capacitance C''_n of the post-coupler depends strongly on the gap $g_n = R_c - R_d - l''_n$ between the post-coupler tip and drift tube surface with R_c and R_d the cavity and drift tube diameters respectively. Since the post-coupler diameter is considerably smaller than the wavelength, one can apply a quasi-static approximation. 3D simulations indicate that the capacitance C'' behaves in a similar way as a two plate capacitor does, i.e. $C''_n = \epsilon_0 A/g_n$ where A is an equivalent post-coupler tip area. Applying these approximations to equation (5.10), the TS′ can be fitted by the following function

$$\mathrm{TS}'_n = \alpha_n + \beta_n \frac{1}{l''_n - l^r_n}. \tag{5.11}$$

with the fitting parameters α_n and β_n, where l''_n is the post-coupler length and $l^r_n = R_c - R_d - (\epsilon_0 A \omega^2 L''_n)$ is a reference length for the post-coupler. Since the frequency is kept constant, the reference is approximately constant.

5.4 Post-coupler study using 3D simulations

5.4.1 Tilt-sensitivity slope studies

In this section, the HFSS simulation [76] is used to verify the TS′ behaviors for a single post-coupler and to study how electromagnetic fields change around the post-coupler as its length changes. A structure with the eight identical cells equipped with seven post-couplers is simulated. The cell length is 88 mm and all post-couplers are initially set at 187 mm. Since we want to compare the electromagnetic field and the stability level of unperturbed and perturbed cases, the same cell structure is chosen. This simplification helps to avoid the perturbation come from non-identical cell mismatch but generally, it has no effect on the TS′ behaviors.

The frequency shift of TM_{010} and the TS′ variation as a function of the fourth post-coupler length are plotted in Fig. 5.2. The fourth post-coupler is varied from 155 mm to 200 mm while other post-couplers are kept at 187 mm. Moving the post-coupler leads to a change in the TM_{010} modal resonant frequency. As is shown in the Figure, the frequency shift is infinite at a length of $l_r = 170$ mm. Generally speaking, in a cavity equipped with N post-couplers, the post-coupler passband consists in N post-coupler modes. As the post-couplers are outside, the post-coupler modes resonate at a higher frequency with respect to the TM_{010} mode. Increasing the post-coupler lengths, the post-coupler passband moves toward lower frequencies. As one of the post-coupler mode confluences with the TM_{010}-mode, the TM_{010} resonance frequency changes suddenly. Further increasing the post-coupler length, the post-coupler mode goes to a lower frequencies than the TM_{010} mode and resonant frequency of the accelerating mode returns around its initial value.

The dependency of TS′ of the fourth cell on the post-coupler length is plotted in Fig. 5.2. Initially, when the length of the post-coupler 4 is 155 mm, TS′ has a positive value about 0.6%/MHz. By increasing the length of post-coupler, the TS′ increases exponentially. At the length of l_r, the TS′ has a pole at which the TS′ changes suddenly from positive to negative infinite values. At this length, the post-coupler is in resonance. The TS'_n value indicates how much the axial field is stabilized locally around the n^{th} cell. According to the figure, the TS and TS′ have a non-linear dependency with the post-coupler length. The best local stabilization corresponds to zero of TS′ and bigger magnitude of TS′ leads to a higher sensitivity to tuning errors. Adjusting post-coupler to the lengths longer than l_r leads to higher TS′. The best local stabilization is around 187 mm.

The simulation results are fit well by equation 5.11. Here, the l_r could be determined from the TM_{010} frequency shift measurements. The α_n and β_n are the fitting constants that need to be calculated. Comparing simulated TS'_n of two different post-coupler lengths, one can find the α_n and β_n coefficients. By knowing these values one can quickly calculate the post-coupler length at which $\mathrm{TS}' = 0$. Assume that the TS′ is measured for two different post-coupler lengths of l''^{1}_n and l''^{2}_n which correspond to $\mathrm{TS}'^{(1)}_n$ and $\mathrm{TS}'^{(2)}_n$. In this case, the α_n and β_n can be found as following

$$\begin{bmatrix} \alpha_n \\ \beta_n \end{bmatrix} = \begin{bmatrix} 1 & (l''^{1}_n - l^{r}_n)^{-1} \\ 1 & (l''^{2}_n - l^{r}_n)^{-1} \end{bmatrix}^{-1} \begin{bmatrix} \mathrm{TS}'^{(1)}_n \\ \mathrm{TS}'^{(2)}_n \end{bmatrix}. \tag{5.12}$$

After finding the α_n and β_n, one can calculate the best post-coupler length by finding the root of equation 5.11.

5.4.2 Calculating circuit element values of a post-coupler

The L'' and C'' are extracted by using HFSS simulations. Instead of using the indirect approach of fitting of the dispersion curve [75], the L'' and C'' are calculated directly. Here, a structure with four identical cells equipped with a post-coupler every drift tube is simulated. The reason for choosing the identical cells is to reduce the tuning errors from matching different cells. Otherwise, the calculation can be repeated for any DTL structure. Stems are ignored to reduce the simulation time. In the absence of stems, the cavity has a symmetry plane and one can simulate half of the cavity (Fig. 5.3). A total stored electric energy U_e and magnetic energy U_m of the post-couplers is assumed to be within a cylindrical volume of 4 cm in radius around post-coupler.

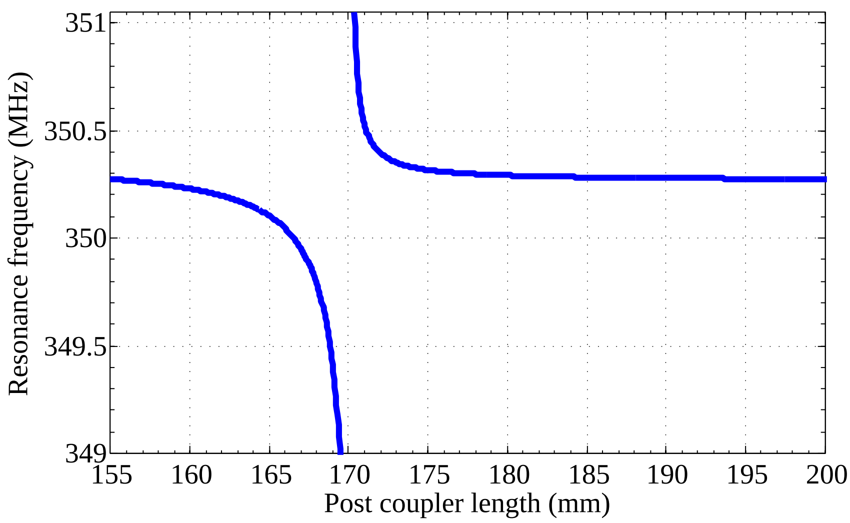

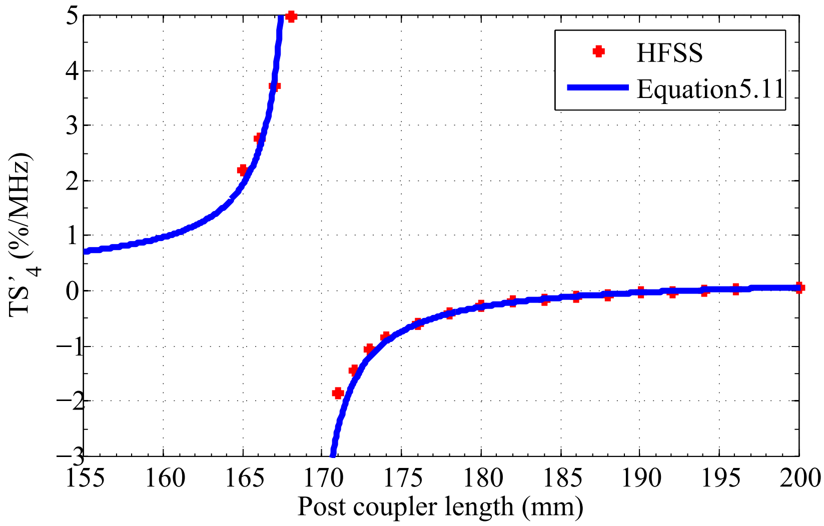

Figure 5.2: Top: The TM_{010} resonant frequency variation as a function of fourth post-coupler length. Bottom: The simulated TS′ (dotted) can fit the equation 5.11.

The electric and magnetic energy of post-coupler can be calculated using [33]

$$U_e = \frac{\epsilon_0}{4} \int_v E^*.E dv, \tag{5.13}$$

$$U_m = \frac{\mu_0}{4} \int_v H^*.H dv, \tag{5.14}$$

and knowing the stored energy, it is possible to calculate the C'' and L'' using

$$C'' = \frac{4U_e}{V_r^2}, \tag{5.15}$$

$$L'' = \frac{4U_m}{I_r^2}, \tag{5.16}$$

where V_r and I_r are the reference voltage and current respectively.

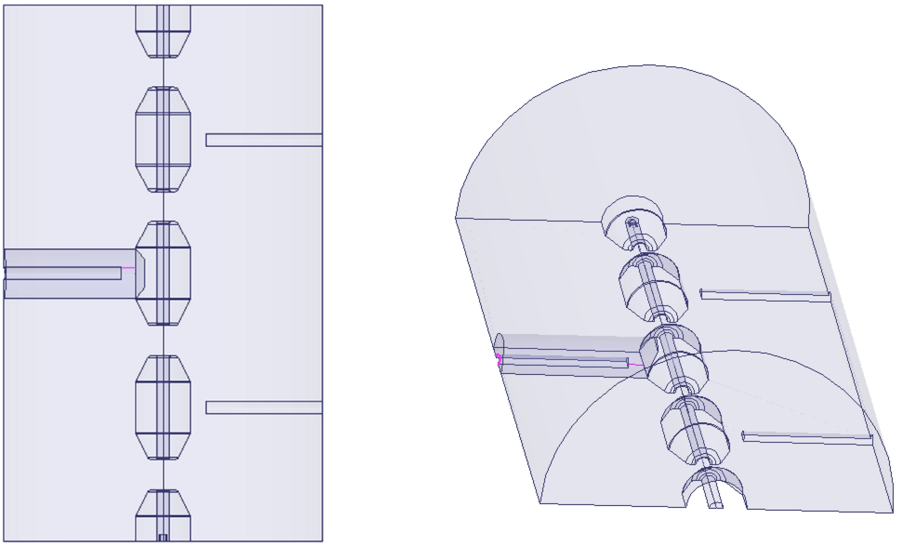

Figure 5.3: The simulated four gaps DTL.

The L'' and C'' of the second post-coupler is calculated as function of the post-coupler/DT gap length g and the results are plotted in Fig. 5.4. Here all post-coupler/DT gaps are set at 3 cm except the second one which is varied between 5 cm and 14 cm. The calculated values of C'' shows that equivalent capacitance behaves similar to a simple two plate capacitor i.e. $C'' \propto g^{-1}$. The L'' is around 9.4 μH. The variation of the natural resonance frequency of a single post-coupler is plotted in Fig. 5.5. Apparently from the figure, natural resonance frequency of the post-coupler increases as gap length increases.

5.4.3 Electric field distribution around a post-coupler at resonance

In Fig. 5.6, the axial view of the electric field for the eight cells structure is plotted. The simulations are done for two different post-coupler lengths. In the first figure, the fourth post-coupler is set at l_r and in the bottom that post-coupler is set at the stabilize length of 187 mm. Other post-couplers are adjusted at 187 mm. Here the same

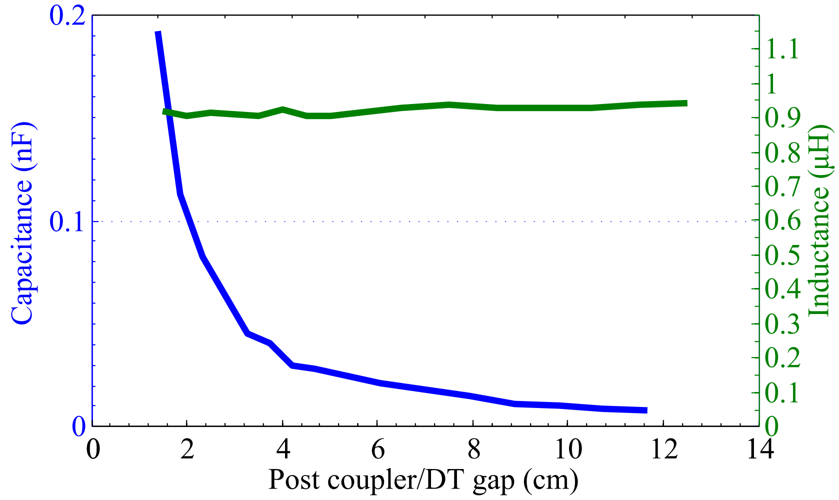

Figure 5.4: The variation of capacitance and inductance of a post-coupler with respect to its length.

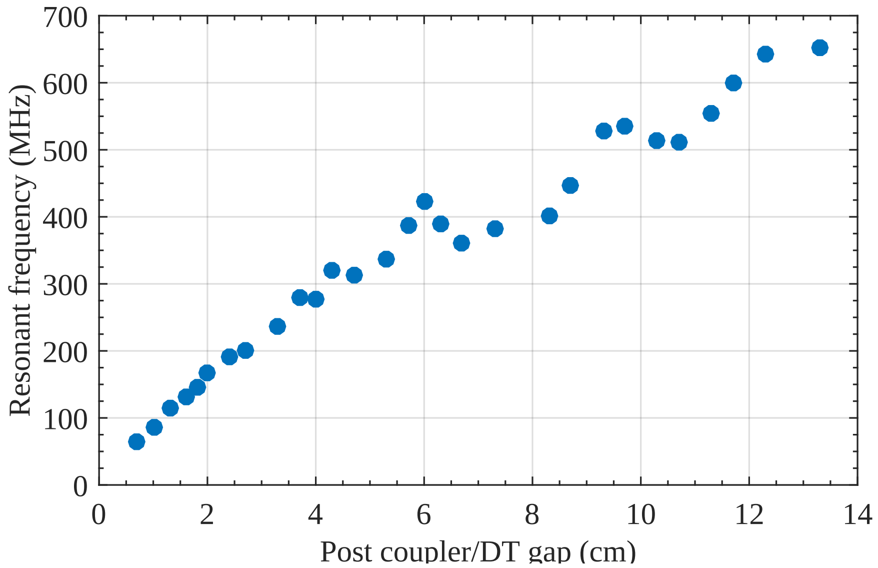

Figure 5.5: The simulated resonance frequency of fourth post-coupler.

perturbation is applied to both cases. Apparently, when the gap between post-coupler 4 and drift tube is 187 mm, post-couplers compensate the effect of perturbations and the electromagnetic field is mostly stored between the drift tubs. When a post-coupler is set to its resonance length, as is shown for post-coupler 4, a considerable amount of electric field gets concentrated at that post-coupler. From the plots, one can deduce that fields between drift tubes on the right-hand side of the excited post-coupler 4 are close to zero and thus the voltage between the drift tube and the tank wall at the excited post-coupler is close to zero as well. In consequence, the coupling admittance must be $Y'_4 = \infty$ and the post-coupler thus is proved to be in resonance.

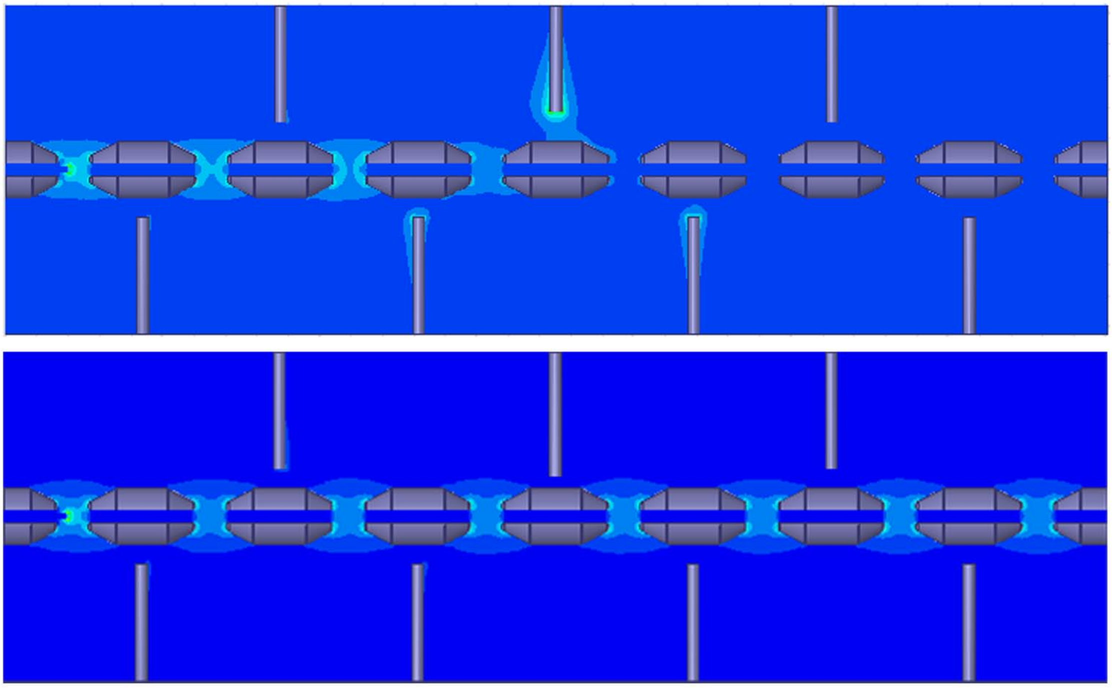

Figure 5.6: The axial view of the excited electric field in 8 structure Top: The fourth post-coupler is set at l_r. Here the fourth coupling admittance gets infinite. Bottom: The fourth post-coupler is set at 187 mm.

5.4.4 Effect of post-coupler radius on tilt-sensitivity slope

The post-couplers of Linac4 DTLs are cylindrical rods with the radius of 10 mm. In order to study the effect of different post-coupler radius on stabilization, 3D HFSS simulation has been performed. In the Fig. 5.7, the post-couplers radius is varied between 4 and 16 mm for the same cell structure and TS′ are calculated for different penetration length. These calculations show that by reducing the post-coupler radius, the stabilization takes place at longer post-coupler length. From the figure, it is seen that the resonance length of post-coupler has a non-linear dependency with respect to the post-coupler radius.

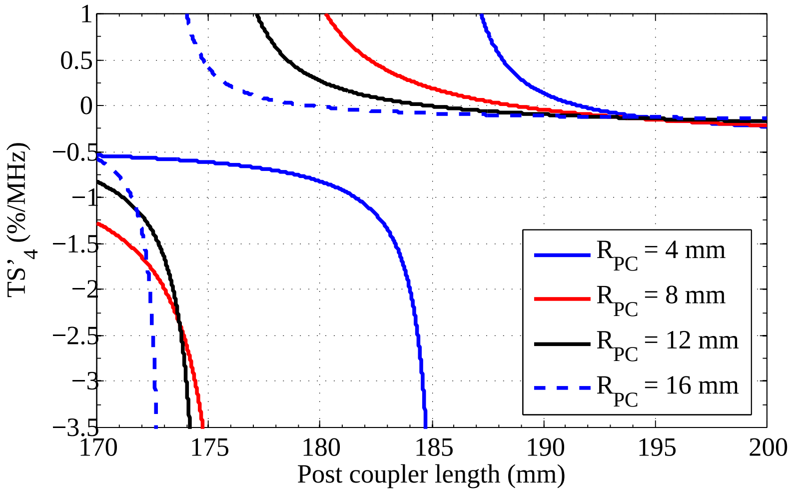

Figure 5.7: The variation of TS′ of 4$^{\text{th}}$ cell with respect to the post-coupler thickness. From figure, it is seen that thicker post-coupler stabilize structure at lower length.

5.4.5 Higher order modes in a post-coupled structure

It was discussed that in a DTL structure, the electromagnetic field can be excited at different eigenfrequencies. In order to measure the frequency dispersion curve of the structure, it is important to know the shape of the axial field in each of these modes. Hence, the axial electric field distribution is studied in the different modes using 3D HFSS simulations. A four-meter post-coupled structure containing 20 identical cell is considered. All post-couplers have been adjusted to 185 mm. The normalized axial fields of TM higher order modes are plotted in Fig. 5.8. Also, the axial field distribution of the last four post-coupler modes are plotted in Fig. 5.9. For an structure with identical cells, it is seen that there is a similarity between the axial fields of post-coupler and higher order accelerating modes.

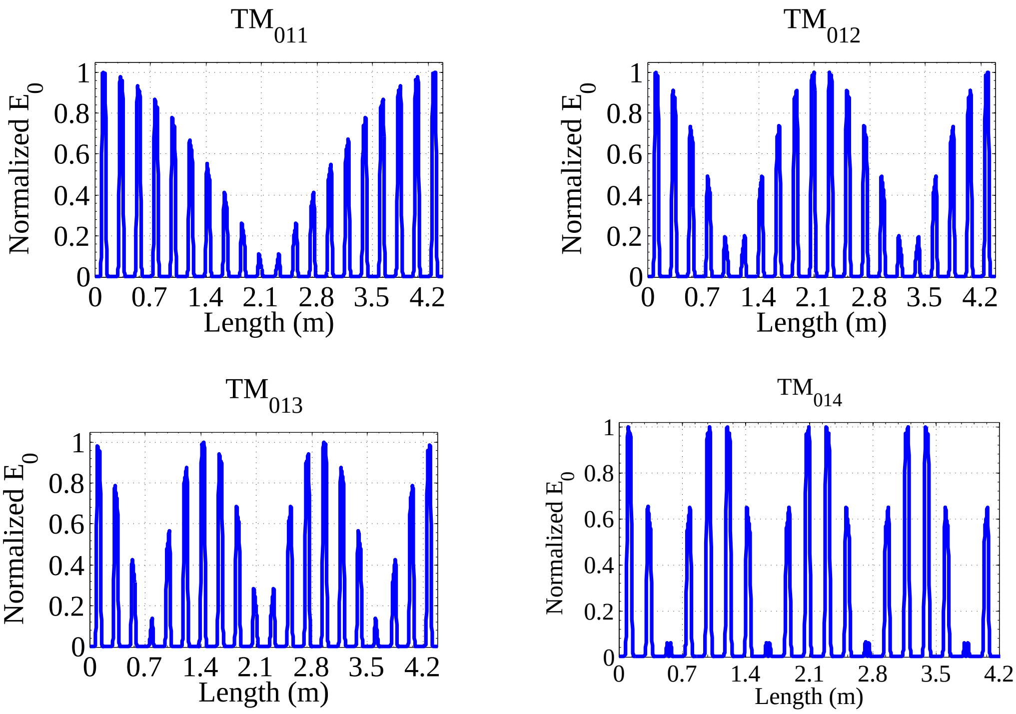

Figure 5.8: Simulated axial field of higher order accelerating modes in a DTL structure with identical 20 cells.

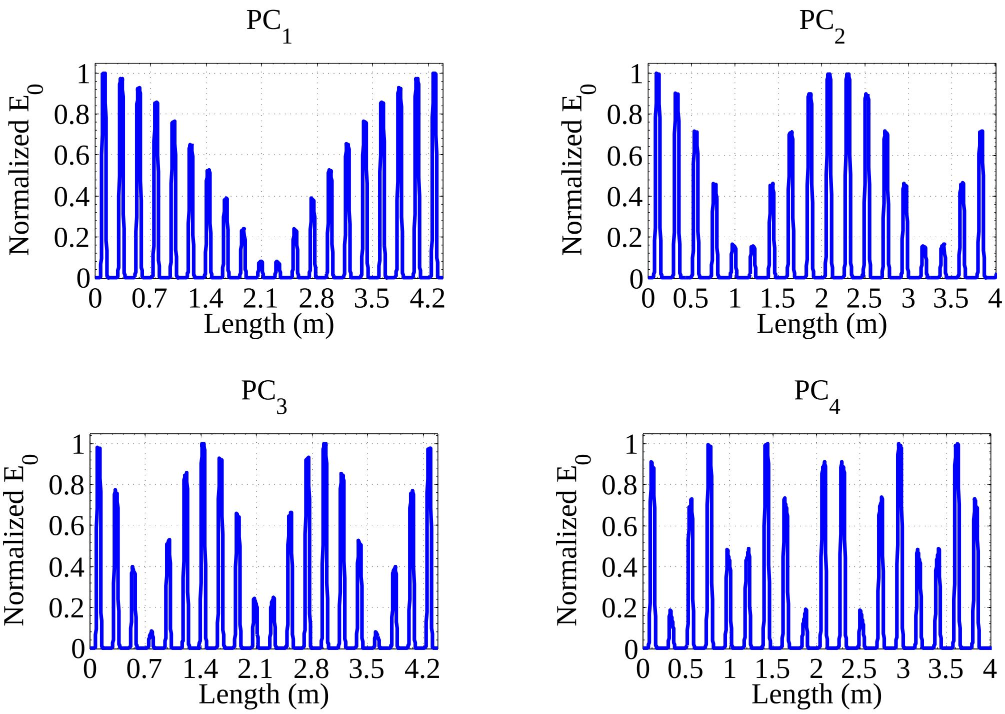

Figure 5.9: The axial field distribution of the last four post-coupler modes.

5.5 Symmetric and asymmetric post-couplers configuration

Let us assume an N same cells structure with a post-coupler per cell. The axial fields of this structure can be stabilized by adjusting all post-coupler at the same length of l''_{sym}. In this case the post-coupler distribution is symmetric in both side of cavity and each post-coupler completely compensate the C' and L'. In symmetric configuration of post-couplers, all coupling admittance is completely compensated by post-couplers and the current is not divided between cells (Fig. 5.10). The other scenario to stabilize structure is to compensate the Y'_{even} partly with one post-coupler and compensate more the Y'_{odd} by using the next post-coupler. This configuration of post-coupler lengths is asymmetric (Fig. 5.10). Since in asymmetric post-coupler configuration, the coupling admittance is not zero, part of current is divided. The next post-coupler is adjusted so that the current before of Y'_{even} and after Y'_{odd} be the same.

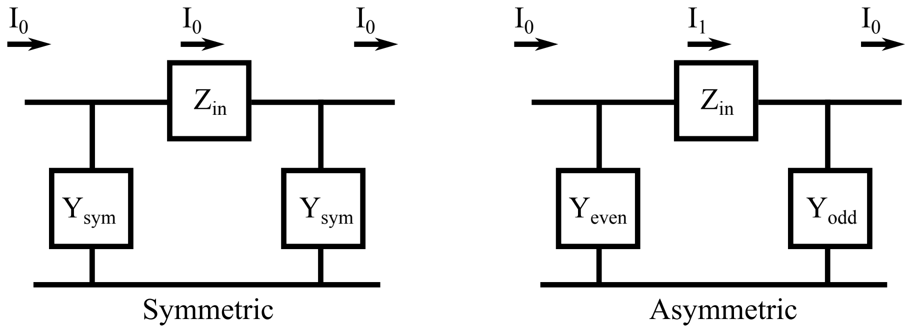

Figure 5.10: The symmetric and asymmetric configuration of post-couplers.

In both of symmetric and asymmetric configurations, one can assume that post-coupler has a negligible effect on C' and conesequently C' is approximately constant. Also to simplify the calculations, stems are ignored. For the symmetric configuration, the admittance Y' (equation 5.4) is zero. Therefore

$$j\omega C' + \frac{j\omega C''_{sym}}{1 - \omega^2 L''_{sym} C''_{sym}} = 0. \tag{5.17}$$

The admittance of post-couplers in the asymmetric configuration is not zero. One post-coupler compensates by amount of $j\omega b$ less than symmetric case and the next post-coupler compensates $j\omega b$ more than symmetric case. Therefore the admittance can be written as follow

$$Y'_{even} = j\omega C' + \frac{j\omega C''_{even}}{1 - \omega^2 L''_{even} C''_{even}} = -j\omega b, \tag{5.18}$$

$$Y'_{odd} = j\omega C' + \frac{j\omega C''_{odd}}{1 - \omega^2 L''_{odd} C''_{odd}} = j\omega b. \tag{5.19}$$

Assume that the post-coupler inductances of all cases are the same. Also the C$''$ is depend on the length of post-coupler. Defining the effective coupling capacitance as $C'^{eff}_{even} = C' + b$ and $C'^{eff}_{odd} = C' - b$ yields

$$\frac{C'}{C''_{sym}} - \omega^2 L'' C' + 1 = 0 \tag{5.20}$$

$$\frac{C'^{eff}_{odd}}{C''_{odd}} - \omega^2 L'' C'^{eff}_{odd} + 1 = 0 \tag{5.21}$$

$$\frac{C'^{eff}_{even}}{C''_{even}} - \omega^2 L'' C'^{eff}_{even} + 1 = 0 \tag{5.22}$$

From equations 5.20 and 5.21

$$C'^{eff}_{odd}\left(\frac{1}{C''_{odd}} - \frac{1}{C''_{sym}}\right) + b\left(\frac{1}{C''_{sym}} + \omega^2 L''\right) = 0, \tag{5.23}$$

and from equations 5.20 and 5.22

$$C'^{eff}_{even}\left(\frac{1}{C''_{even}} - \frac{1}{C''_{sym}}\right) - b\left(\frac{1}{C''_{sym}} + \omega^2 L''\right) = 0, \tag{5.24}$$

Adding equations 5.23 and 5.24 yields

$$C'^{eff}_{odd}\left(\frac{1}{C''_{odd}} - \frac{1}{C''_{sym}}\right) + C'^{eff}_{even}\left(\frac{1}{C''_{even}} - \frac{1}{C''_{sym}}\right) = 0. \tag{5.25}$$

The capacitance of post-couplers is proportional to the inverse of the gap g'', i.e. $C'' = \epsilon A/g''$, where A is the area of post-coupler tip. For a DTL cavity with radius of r_c and the drift tube radius of r_d, the gap length is $g'' = r_c - r_d - l''$. Therefore equation 5.25 can be written as

$$\frac{C'^{eff}_{even}}{C'^{eff}_{odd}} = \left(\frac{l''_{odd} - l''_{sym}}{l''_{sym} - l''_{even}}\right). \tag{5.26}$$

The left hand side of this equation can be written

$$\frac{C'^{eff}_{even}}{C'^{eff}_{odd}} = \frac{C'^{eff}_{even}}{C''_{even}} \frac{C''_{even}}{C''_{odd}} \frac{C''_{odd}}{C'^{eff}_{odd}}. \tag{5.27}$$

From equations 5.18 and 5.19 and by considering the resonance length of post-coupler $l^r = \omega^2 \epsilon A L''$, one can show

$$\frac{C'_{even}}{C''_{even}} = \frac{l''_{even}}{l^{r-even} - l''_{even}}, \tag{5.28}$$

$$\frac{C'_{odd}}{C''_{odd}} = \frac{l''_{odd}}{l^{r-odd} - l''_{odd}}. \tag{5.29}$$

Therefore, rewriting the equation 5.27 using 5.28 and 5.29 yields

$$\begin{aligned} \frac{C'^{eff}_{even}}{C'^{eff}_{odd}} &= \frac{\frac{\epsilon A}{l''^{even}}}{\frac{\epsilon A}{l''^{odd}}} \frac{l''^{even}}{l^{r-even} - l''^{even}} \frac{l^{r-odd} - l''^{odd}}{l''^{odd}} \\ &= \frac{l^{r-odd} - l''^{odd}}{l^{r-even} - l''^{even}}. \end{aligned} \tag{5.30}$$

Finally using equations 5.25 and 5.30, the relation between symmetric and asymmetric post-coupler lengths are

$$l''^{sym} = \frac{l''^{odd}_n (l^{r-even}_n - l''^{even}_n) + l''^{even}_n (l^{r-odd}_n - l''^{odd}_n)}{l^{r-even}_n - l''^{even}_n + l^{r-odd}_n - l''^{odd}_n} \tag{5.31}$$

In order to verify the equation 5.31, 3D simulation of an 8 cells structure is used. In this simulations, the odd post-couplers initially were set at 180 mm. Then by moving even post-couplers, the best stabilization is seen when even post-coupler are set at 194 mm (Fig. 5.11). In this case, the simulated resonant length of odd and even post-coupler are 165 and 172 mm respectively. The TS of this case is plotted in Fig. 5.12. As is seen from the figure, The TS slope alternate from positive to negative slope every two cells. This is due to the fact that one the post-couplers does not compensate axial field errors completely and therefore its next post-coupler should compensate more. Applying the asymmetric post-couplers length into the equation 5.31, the calculated symmetric length is 185.68 mm. 3D simulations show that the symmetric post-coupler length is around 186.00 mm. The calulated post-coupler length is about 0.17% different from the simulated post-coupler length.

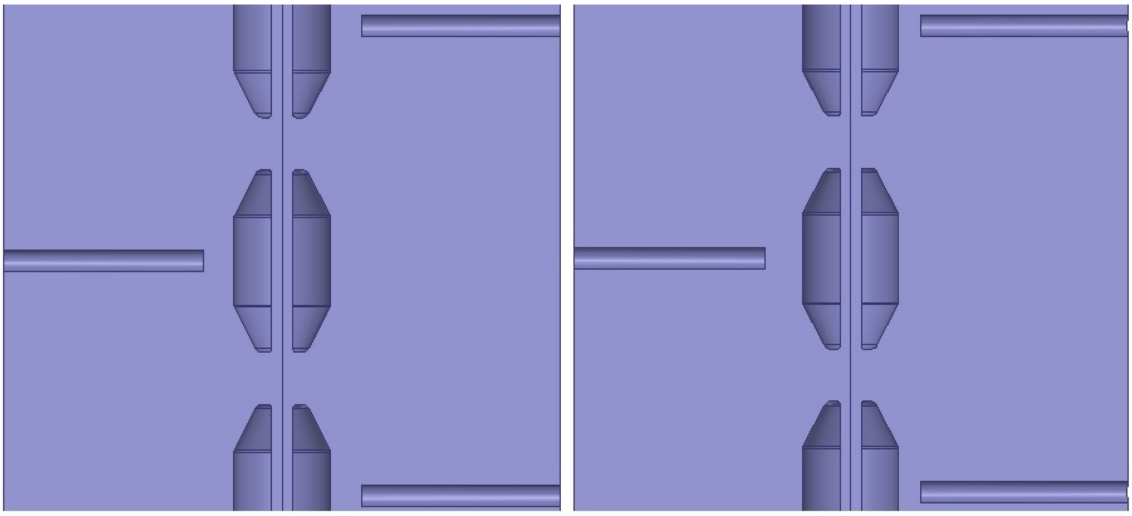

Figure 5.11: A symmetric(Left) and Asymmetric(Right) post-couplers arangment

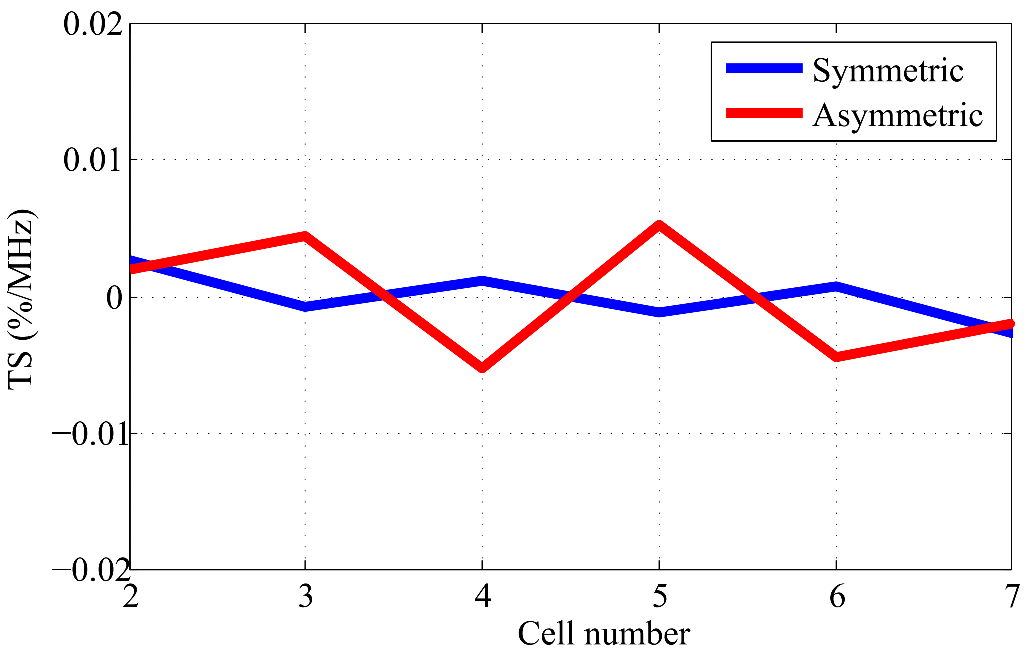

Figure 5.12: Comparison between TS of asymmetric and symmetric post-couplers. In symmetric distribution of post couplers, TS has smoother variation than asymmetric one. This is due the fact that one post-coupler is under-compensated and the other one is over-compensated.

Chapter 6

Experimental results

6.1 Introduction

In the previous chapter, the theory of the new procedure to adjust post-couplers is established and it has been verified using 3D simulations. In the present chapter, this procedure is studied on real DTL cavities. These measurements are performed on the CERN Linac4 DTL cavities (Tank1, Tank2 and Tank3).

All of the Linac4 DTL cavities operate at 352.2 MHz for the acceleration of H^- ion-beams from 3 to 50 MeV. Tank1 is a 3.9 m long structure and it consists of 39 cells. The cell length increases from 68 to 143 mm. The total 12 slug tuners are distributed along the structure and 12 post-couplers are used to stabilize axial field (a post-coupler every three cells). Tank2 is 7.34 meter long cavity and consists of 42 cells [77]. In this structure, the cell length increases from 137 to 210 mm. Post-couplers are distributed every two drift tubes and the 20 slug tuners are distributed horizontally along the axis of the cavity. Tank3 is a 7.25 meter long structure and consists of 30 cells. The cell length increases from 219 to 263 mm. All drift tubes are equipped with a post-coupler and 17 slug tuners are used to tune the electric field. The inner diameter of Linac4 DTL cavities is about 520 mm and the drift tube diameter is 90 mm [78]. Different views of drift tubes, post-couplers and tuners of Linac4 DTLs are shown in Fig. 6.1. An outside view of Tank1 in its final position in the tunnel is also shown in the bottom right panel.

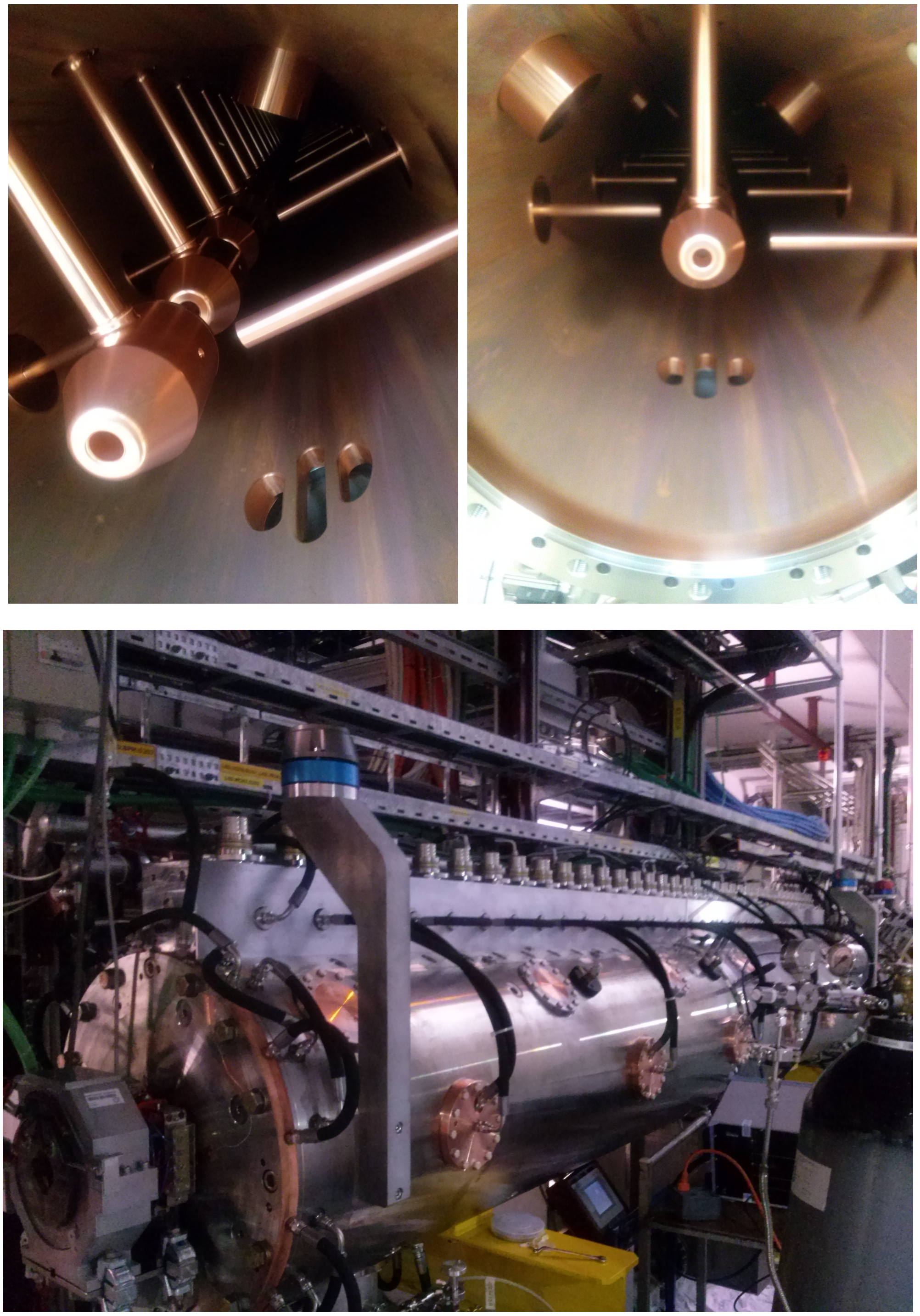

Figure 6.1: Top: Side and front view of CERN's linac4 DTL Tank3 equipped with final post-couplers and tuners. Bottom: A picture of Tank1 installed in the tunnel.

6.2 CERN Linac4 DTL cavities

Between Linac4 DTLs, the stabilization of DTL Tank1 is accomplished using the TS optimization approach and the other tanks are stabilized using TS′ analysis technique. In the following, the procedure of stabilization of these cavities and the experimental RF measurement results are discussed.

6.2.1 Stabilization of Tank1 by tilt-sensitivity optimization

The Linac4 DTL Tank1 is stabilized using the TS optimization method. The details of stabilization is discussed in the following.

In 5.2.2, it is mentioned that before starting TS optimization, all post-couplers are adjusted to an initial length by using dispersion curve. In order to obtain the initial post-coupler length of Tank1, all post-couplers are moved in uniformly from 10 to 200 mm. For each post-coupler length the dispersion curve is measured in a frequency range of [200, 450] MHz. The initial post-couplers is the length at which the spacing of the nearest modes above and below the operating mode is approximately symmetrized [79]. The measured dispersion curve is plotted in Fig. 6.2. In the figure, post-coupler lengths are changed from 174 and 180 mm every 2 mm. For post-couplers length of 174, 176 and 178 mm, the PC_1-mode/TM_{010}-mode frequency difference are about 0.56, 1.89 and 3.10 MHz and TM_{011}-mode/TM_{010}-mode frequency difference are about 5.87, 4.84 and 3.88 MHz. The frequency spacing of TM_{011}-mode/TM_{010}-mode and TM_{010}-mode/PC_1-mode are more symmetric when post coupler lenghts are 178 mm.

The advantage of starting with the initial length is that the final post-coupler lengths are distributed around this initial number and it reduces the number of measurements. By adjusting all post-couplers of Tank1 to the initial length of 178 mm, the TS values have been reduced by a factor of 4 but still TS values are far away from the target values. Therefore, the next step is to stabilize DTL Tank1 within the acceptable limit. In order to compare stability of different post-coupler configurations, numerical value of $ST_t = \max(\mathrm{TS}) - \min(\mathrm{TS})$ is minimized. The TS optimization procedure for the stabilization of DTL Tank1 is

1. The length of few post-coupler are changed and the TS of the new configuration of post-coupler are measured.

2. For the new post-coupler configuration, the ST_t is calculated.

3. The ST_t value of the former post-coupler configuration and the new post-coupler configuration are compared. The post-couplers are adjusted to the configuration with lower ST_t value.

4. The steps 1..3 are repeated for different random configuration of post-couplers untill the ST_t lay within the acceptable limit.

As will be in section 6.2.2.1, the resonant properties of each post-coupler is depend on neighboring post-couplers. Therefore, a big number of TS measurements is required to stabilize the cavity. The DTL Tank1 is stabilized by using around few hundred TS measurements [74]. Each TS measurement consists of two bead-pull measurements, two cavity perturbations and extraction of the axial field from bead-pull results. For Tank1, each TS measurement takes around 20 min, so considerable numbers of days were spent for stabilization of Tank1.

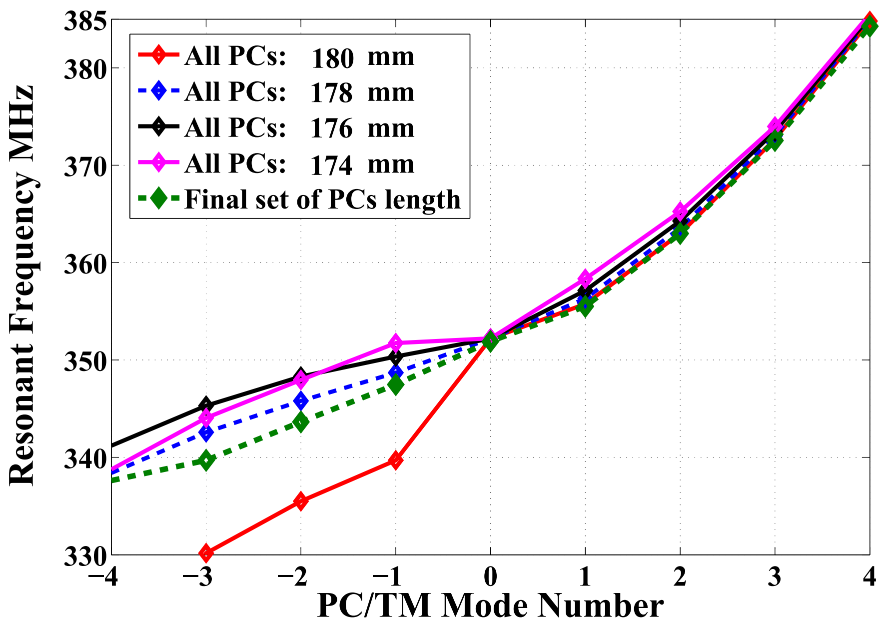

Figure 6.2: The measured dispersion curve of PC_{-p} and TM_{01p} modes for different set of PCs length.

The initial TS values with no post-couplers inside of the DTL Tank1 are distributed within [-65, 70]%/MHz (Fig. 6.3). Finally, the TS of Tank1 is reduced to [-5, 5]%/MHz after adjusting post-couplers. The ST_t is decreased by about14 times with respect to its initial value. The stabilization level of DTL Tank1 is comparable with the stabilization level reported by Billen, et al. on RGDTL [57].

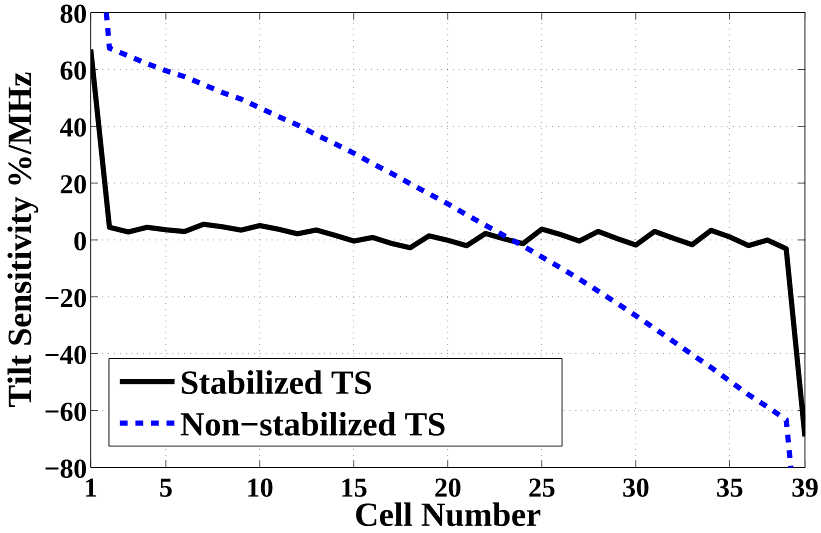

Figure 6.3: Initial and final TS of CERN's Linac4 Tank1.

The final post-coupler lengths are plotted in Fig. 6.14. In Tank1, the lengths of first seven post-couplers are in the range of [181, 185] mm. For the other post-coupler, their lengths decrease so that the difference in length of post-coupler number 7 and 12 is around 20 mm.

The axial field of each resonant mode is compared with the simulation to verify the mode number. The measured phase shift of the first six resonance modes of TM pass-band are plotted in Fig. 6.4. Also, the measured phase shift of the last four post-coupler modes is plotted in 6.5. By comparing the number of zero nodes of measured electric field or phase shift with the simulation, it is possible to recognize the excited mode. Note that the simulated electric field in the previous chapter belong to the identical cell structures but in measurements, the cell length increases with the energy of particles. By the way, the number of zero nodes are the same in both cases.

6.2.2 Stabilization of Tank2 & Tank3

6.2.2.1 Tilt-sensitivity analysis of a single post-coupler

In the previous chapter, the post-coupler adjustment using TS′ analysis technique has been discussed on the basis of the equivalent circuit model and HFSS simulations. In this section, the practical value of the TS′ analysis approach for the stabilization of DTL cavities is demonstrated using the CERN Linac4 DTL Tank2 & Tank3. The dependency of the TS′ of the seventh post-coupler of Tank3 is investigated further. The reader shall note however that all post-couplers without exception show

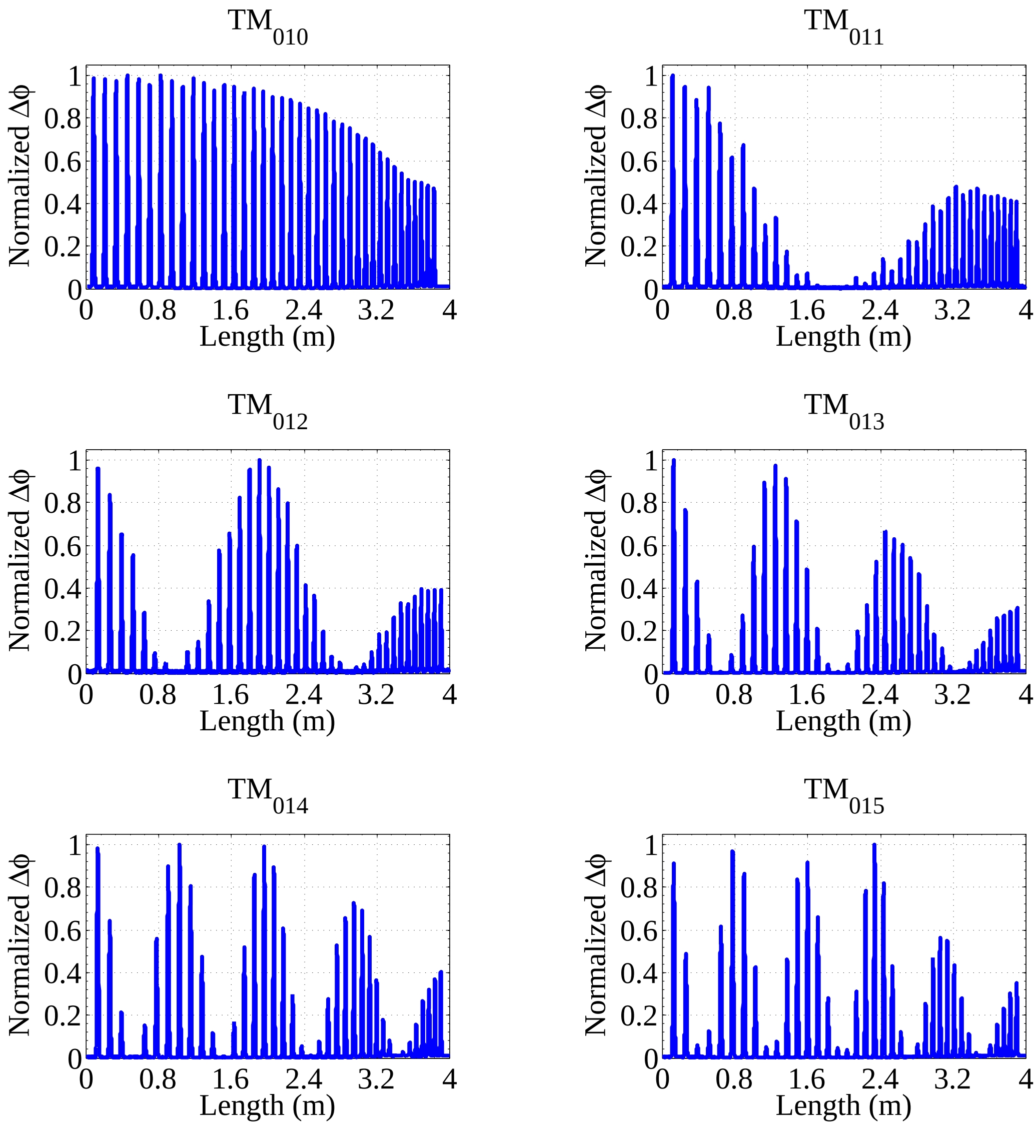

Figure 6.4: The measured phase shift of the first six resonant modes of TM pass-band of tuned and stabilized Tank1.

the same qualitative behavior and varying cell length is not an issue. In the measurements of TS'_7, the post-coupler length is varied between 155 mm and 196 mm, while all other post-couplers are fixed at 186 mm (Fig. 6.6). The results show that the equation 5.11 fits well the measurements. The best stabilization of post-coupler 7 is found at $l''_7 =$ 182 mm. As in the simulations before, the TM_{010} modal resonance frequency has a strong variation at $l^r_7 = 170$ mm as does the TS'_7 (Fig. 6.7). It is thus straightforward to determine l^r_7 by spectral measurements alone.

The TS for different length of post-coupler 7 of 188, 182 and 174 mm are plotted

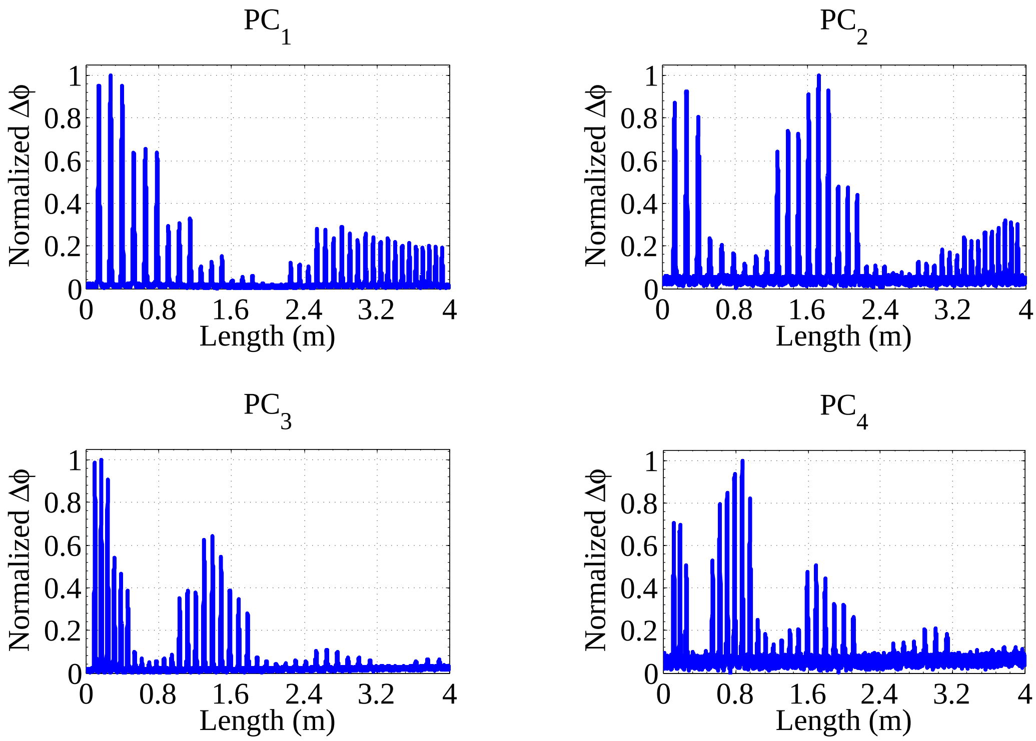

Figure 6.5: The measured phase shift of the last four post-coupler's mode of tuned and stabilized Tank1

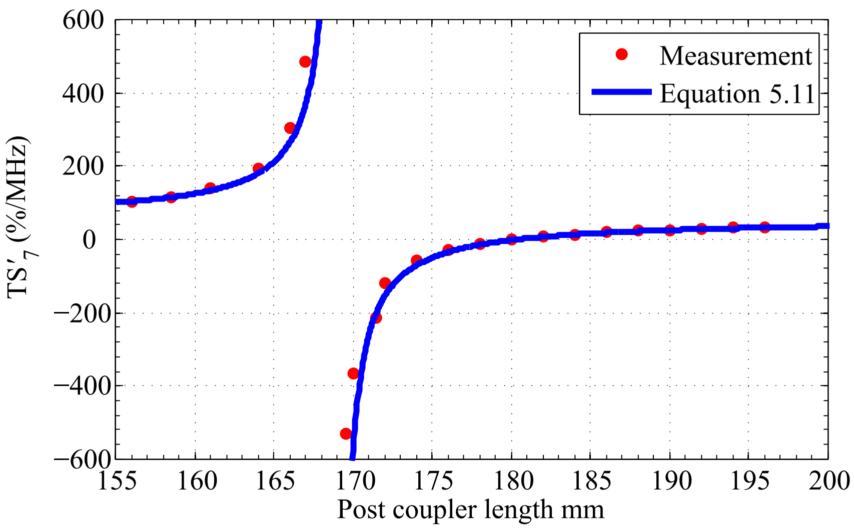

Figure 6.6: The TS'_7 variation as a function of the length of post-coupler 7 l''_7. The TS'_7 behavior is well defined and can be fit using equation (5.11).

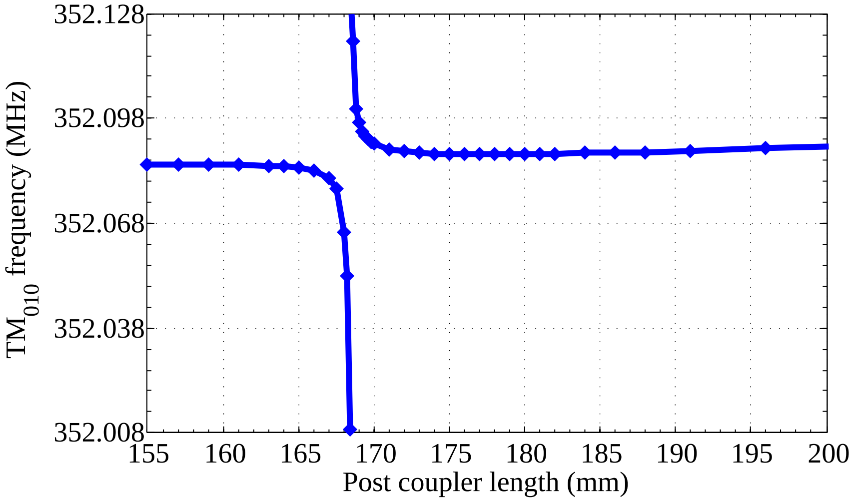

Figure 6.7: The frequency shift of the TM_{010} mode as a function of the length of post-coupler 7 l''_7. It is straightforward to measure l^r_n accurately by varying the post-coupler length and observing the spectrum.

in the Fig. 6.8. The TS has a steep negative slope at l''_7 of 174 mm and its slope is around zero at 182 mm. Finally, positive TS′ is seen at 188 mm. Since this length is far away from resonance, the TS′ is not as big as the case of $l''_7 = 174$ mm. From the figure, it is clear that post-coupler seven does not influence the TS slope of further cells. For example in the figure, the TS′ doesn't change before cell number 5 and after cell number 9 for different post-coupler 7 lengths.

So far, the TS′ has been analyzed under the assumption that just one post-coupler is adjusted in length and all other post-couplers remain at the fixed length. These measurements show that by moving an individual post-coupler, it is possible to stabilize a cavity locally and the TS′ of the other cells remain unchanged.

Since the objective is to stabilize the axial electric field all along the DTL tank, the influence of neighboring post-couplers needs to be taken into account. l^r of post-coupler 27 in Linac4 DTL Tank3 has been measured while just one of its neighbors is adjusted (Fig. 6.9). Moving one of the next neighbor post-couplers (l''_{26} or l''_{28}) changes the reference length for resonance l^r_{27} strongly. This dependency on the next neighbors readily emerges from the Y'_{n-1} and Y'_{n+1} dependencies on the left-hand side of equation (5.6). For the second next neighbors i.e. post-couplers 25 and 29, l''_{25} and l''_{29} have almost no influence and l^r_{27} varies very little regardless of the other post-coupler lengths. From the measurement results, one can thus conclude that the other post-couplers except the nearest neighbors do not affect TS'_n. This finding might

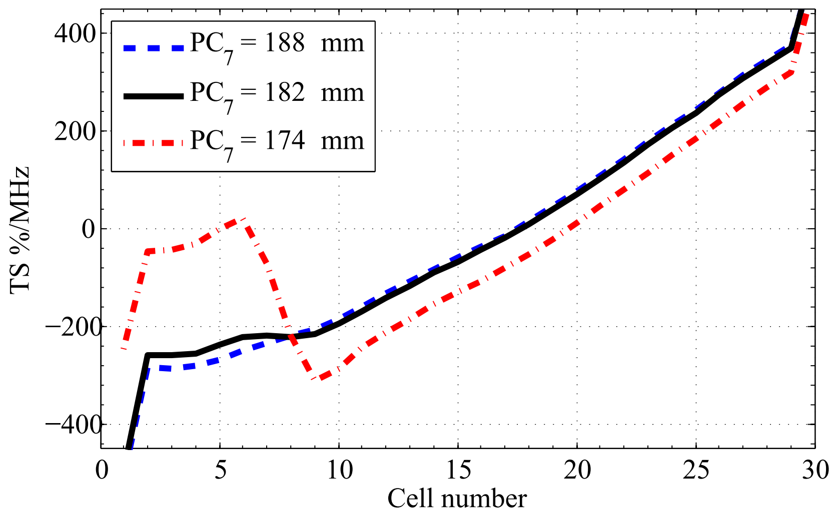

Figure 6.8: The TS for the different position of post-coupler 7 with negative, zero and positive slopes at 174, 182, 188 mm respectively. Clearly, at zero of TS′ the axial field locally stabilized.

be surprising in the light that mutual inductances between post-couplers have been neglected. Taking advantage of the independency from second neighbor post-couplers, it now becomes possible to adjust more than one post-coupler at the same time. This is a valuable ingredient to the stabilization procedure to be discussed later.

Rather the post-couplers dependency on each other, in the following, the influence of tuner movements on TS and TS′ is studied. From 3D simulations, one can see that tuners directly influence the cell inductance L_n, but they have no direct effect on the coupling admittance or the TS. In order to verify this finding, the TS is measured for different sets of tuner penetration (Fig. 6.10). For this analysis, the DTL structure is well stabilized at the operating frequency of ω_{op} = 352.08 MHz in air and the first three measurements are taken at this resonance frequency. All tuners are set at the same length except for one that is used to adjust the frequency to the operating frequency. This measurement is repeated for three different tuners along the structure. Tuner 1 is located at the beginning, tuner 13 somewhere in the middle and tuner 17 at the end of the cavity. Each tuner is moved inwards by around half of its length (80 mm) so that the local perturbation is considerable. As is shown in the figure, the TS does not change when the structure resonance frequency remains constant.

In figure 6.10, also, two cases are shown in which all tuners are moved uniformly from their initial length to a resonance frequency with ±0.02 MHz offset from the target frequency ω_{op}. The change in operating frequency leads to a slope in TS and

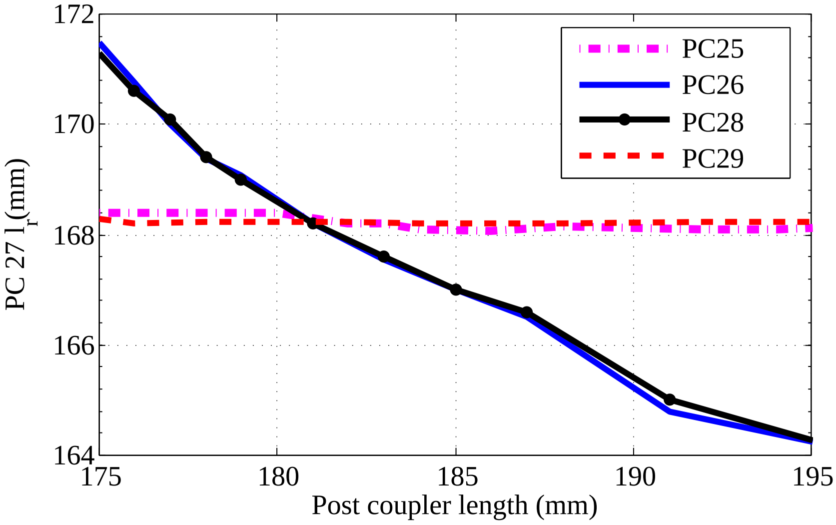

Figure 6.9: The dependency of resonance length l_{27}^r on the neighboring post-couplers. The nearest neighbor post-couplers influence the resonance strongly but from the second nearest neighbors, post-couplers do not affect l_{27}^r. This important result allows for adjustment of every second post-coupler concurrently.

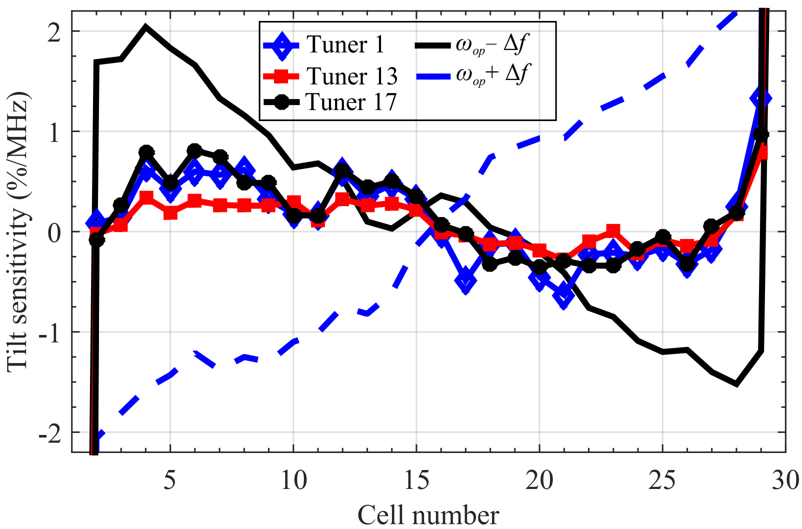

Figure 6.10: Variation of the TS with individual adjustment of tuners 1, 13, and 17. The influence by individual tuners is small while there is a clear dependency on the resonance frequency of the structure.

consequently affects the TS$'$. TS'_n is proportional to Y'_n and the change in operating frequency moves this element off the resonance point $Y'_n = 0$. In conclusion, the cavity needs to be stabilized at the operating frequency first and only then tuned for field flatness.

6.2.2.2 Stabilization procedure

As mentioned earlier, the goal of stabilization is to reduce the sensitivity of the axial accelerating field to perturbations at the operating frequency ω_{op}. It is thus essential that all measurements are undertaken at the operating frequency.

The stabilization procedure is

1. Set all the post-couplers to the same initial length such that the post-coupler passband approximately closes in confluence with the cavity mode passband. Note that this point is reached sufficiently well when the first post-coupler mode is as much in frequency below the TM_{010} mode as the TM_{011} mode is above.

2. Measure the TS and analyze TS'_n for every cell.

3. Set all post-coupler of one cavity side at a new length. The post-couplers of the other cavity side must not change.

4. Measure the TS and analyze the TS'_n.

5. Measure the resonance length l_n^r of all these post-couplers. In this step, the first post-coupler is moved until the post-coupler mode confluences with the TM_{010} mode. Return the post-coupler to the previous length and continue with the next post-coupler on the same side.

6. Calculate α_n and β_n for each post-coupler from two TS measurements (equation 5.11). The post-coupler length for $\text{TS}'_n = 0$ is $l''_n = l_n^r - \beta_n/\alpha_n$.

7. Set all post-couplers to the calculated value and measure the TS again.

8. Repeat steps 3 to 7 for the post-couplers of the other cavity side in order to improve the TS further.

So far, the stabilization procedure of drift tube cavities equipped with a post-coupler at every drift tube has been discussed. As is common practice at the low energy tanks of DTLs however, a post-coupler only every two or three drift tubes is used where the drift tubes are closely spaced for two reasons; First the drift tube spacing might not allow for more post-couplers and secondly roughly speaking each post-coupler is capable of compensating a certain drift tube to cavity capacitance C'_n independent of the number of drift tubes per-unit-length. In this case, the TS′ definition needs to be modified. With T_{pc} being the number of cells per post-coupler and the m^{th} cell located before the n^{th} post-coupler, the general LTSD of n^{th} post-coupler is defined as:

$$\mathrm{TS'_n} = \frac{\mathrm{TS_{m+T_{pc}}} - \mathrm{TS_m}}{\mathrm{T_{pc}}} \tag{6.1}$$

The same stabilization procedure applies to this modified TS′ definition.

The stabilization procedure by RF measurements requires the search of the resonance frequency ω'' of individual post-couplers and fitting the Y' curve. In the case that one considers stabilization by 3D simulations however, searching the resonance of individual post-couplers is not as straightforward. Anyway, it is possible to extract the post-coupler configuration in advance by simulations using this procedure.

In the following, the stabilization results of Tank2 and Tank3 are discussed. Fig. 6.11 shows the measured TS of Tank3 during the stabilization process. The initial measured TS is distributed between ±100%/MHz. The end cell perturbation for the TS measurements is 120 kHz. The global TS of the structure is reduced to ±40%/MHz by adjusting all post-couplers to the initial length of 181 mm (step 1).

As is shown in figure 6.11, just with the evaluation of two TS measurements (step 7), the odd numbered post-couplers are adjusted and the TS is reduced to ±3%/MHz. Repeating steps 1..7, the even-numbered post-couplers are adjusted. The final TS remains within ±1%/MHz in all cells.

The results of stabilization of Linac4 Tank2 is plotted in Fig. 6.12. Since the structure has one post-coupler per two drift tubes, the general form of the TS′ equation (6.1) is used with $T_{PC} = 2$ to calculate the TS'_n values. First by adjusting the post-coupler band for confluence, the TS reduces from ±100%/MHz to ± 40 %/MHz (step 1). Then by adjusting the odd numbered post-couplers, the TS reduces to ±12%/MHz and adjusting the even numbered post-couplers, the TS becomes less than ±5 %/MHz. The reader may note that the absolute stability improvement in Tank2 is less than on Tank3 as there is only one post-coupler every two drift tubes in Tank2. The parameters of the stabilization procedure α, β, and l^r, are shown in Fig. 6.13.

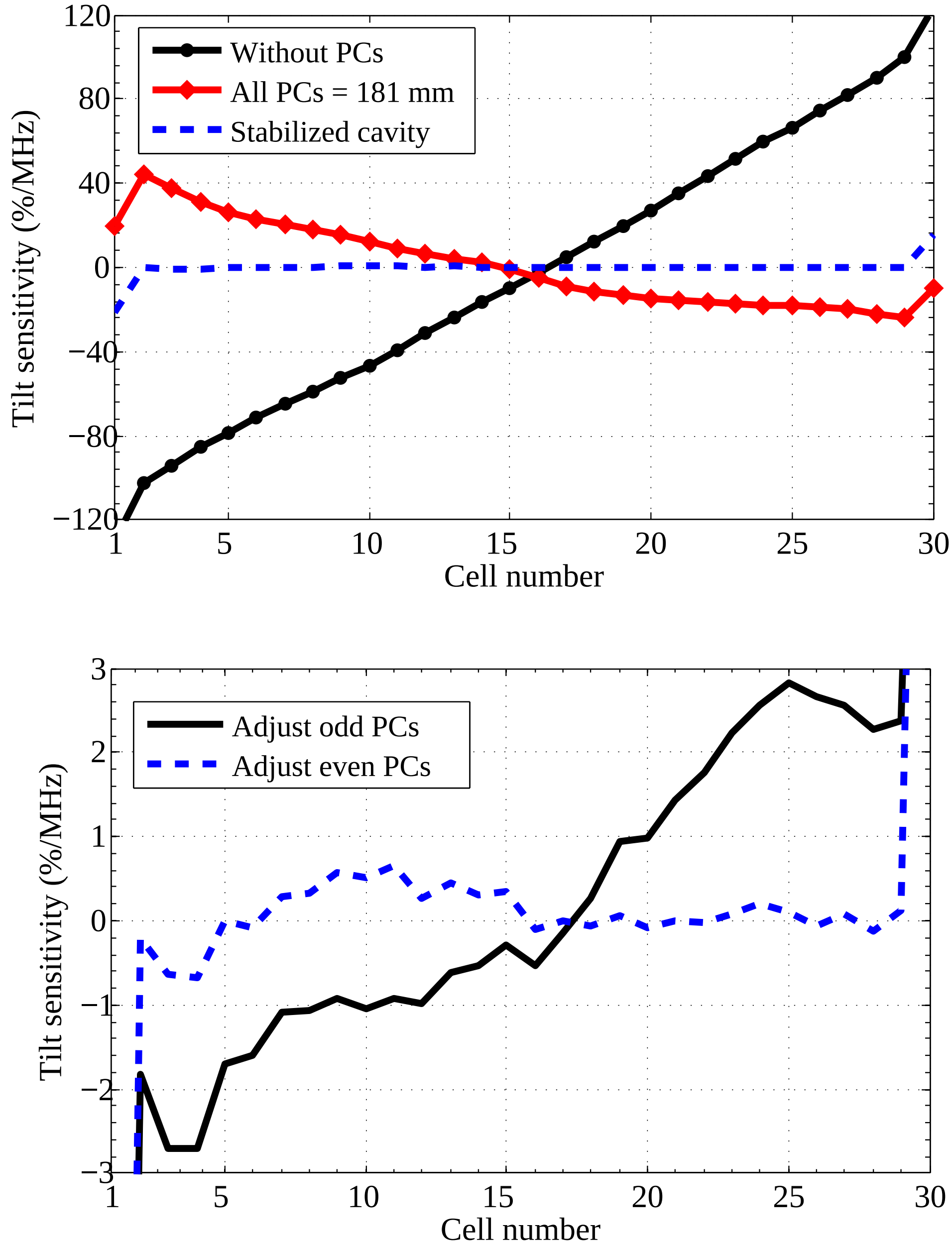

Figure 6.11: Results of the post-coupler optimization for the Linac4 DTL Tank3. The initial TS is reduced by a factor of 100.

6.2.2.3 Symmetric and asymmetric post-coupler configurations

In the procedure presented in 6.2.2.2, the DTL is stabilized by adjusting post-couplers of one side of the cavity while the post-couplers on the other side are fixed in length. Depend on the initial length of post-couplers, different configurations of post-coupler is extracted by the procedure. In consequence the post-coupler configuration usually

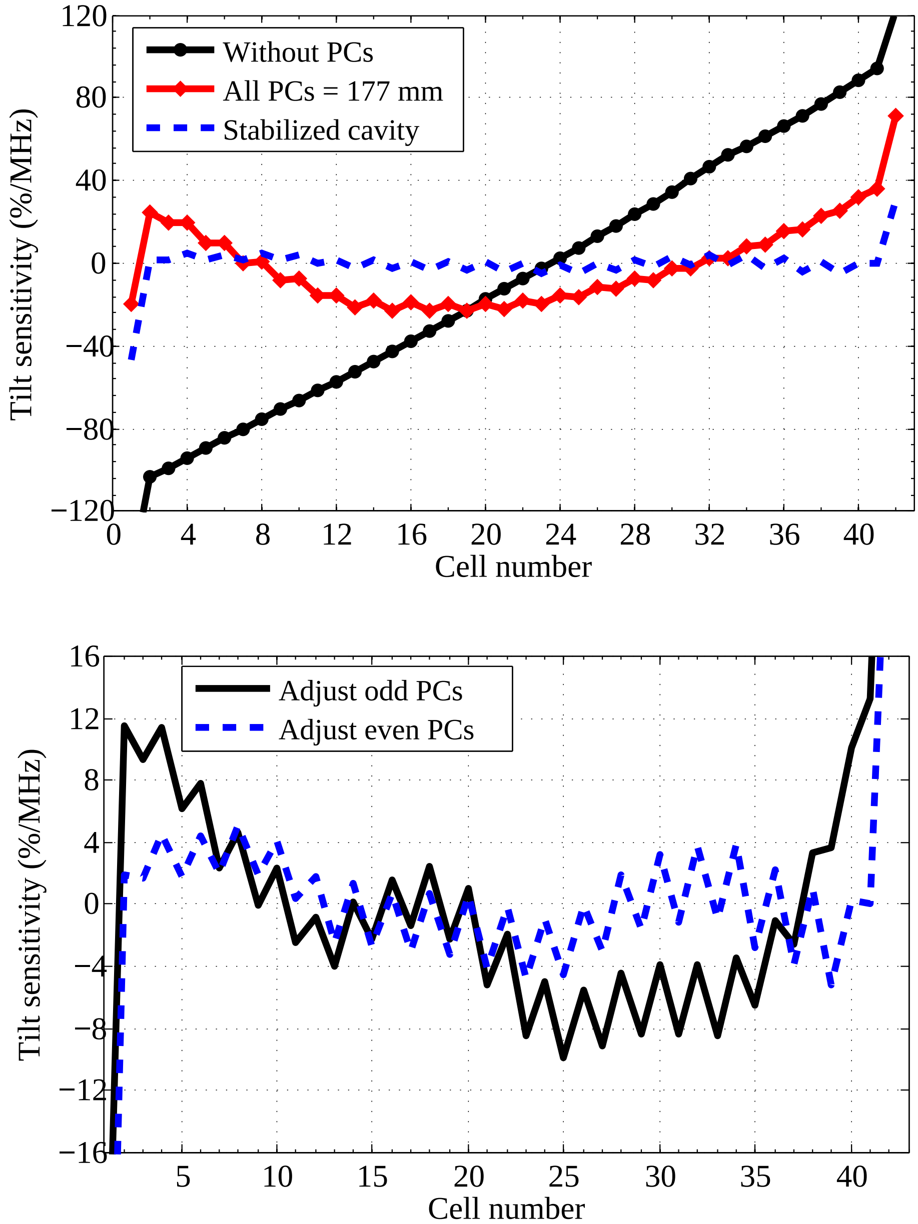

Figure 6.12: Results of the post-coupler optimization for Linac4 Tank2. The initial TS is reduced by a factor of 20.

is not symmetric.

According to the equation 5.31, the symmetric post-coupler length can be calculated from asymmetric post-coupler length. As a consequence, TS values in structure can be further reduced by finding a symmetric configuration. The final TS measurements of Linac4 DTLs show that the current TS values are sufficient and that a slight asymmetry in the post-coupler configuration is not of particular importance.

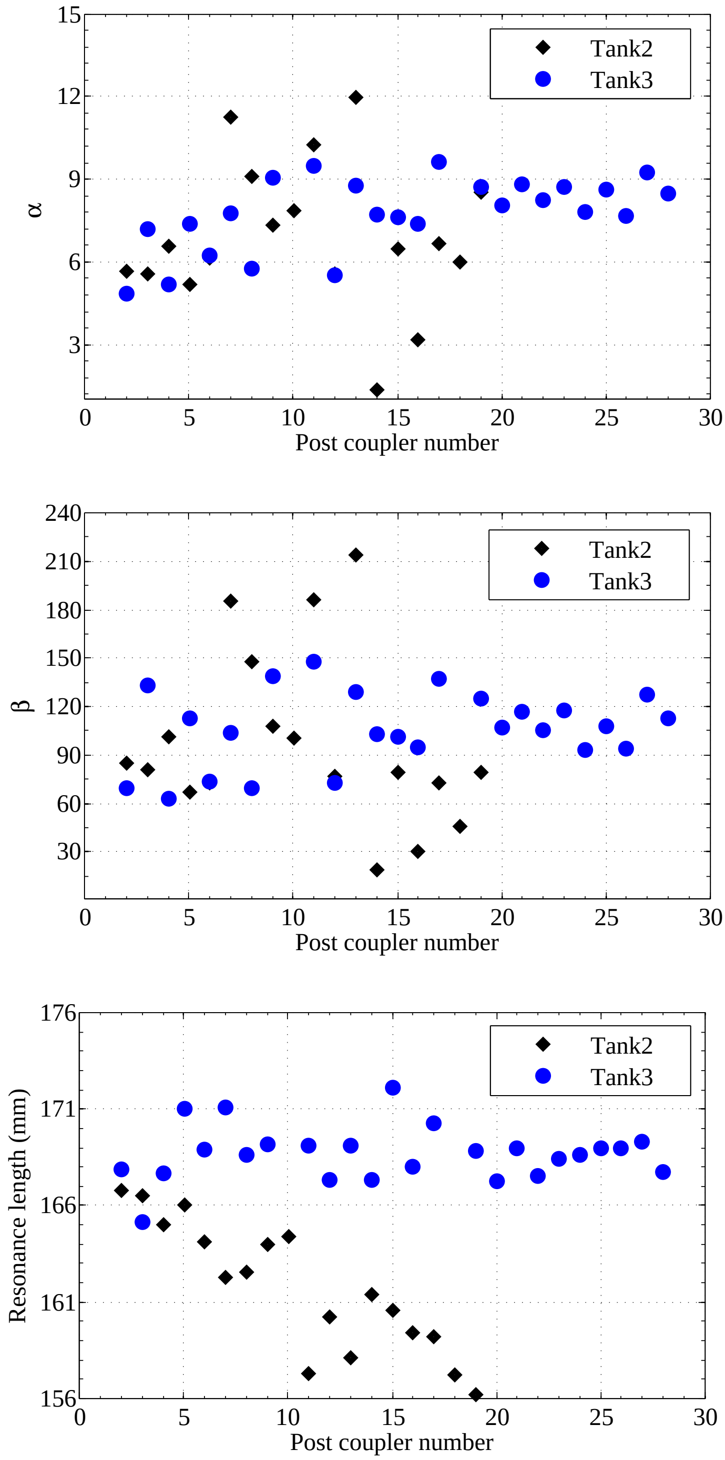

Figure 6.13: Parameters α_n, β_n, and the resonance length l_n^r for all post-couplers of tank 2 and tank 3. Note that the values are measured separately on either side (even or odd numbered post-couplers) and that all parameters depend on the settings of the next neighbor post-couplers.

6.3 Tuning of Linac4 DTL cavities

When the cavity is stabilized, the field flatness improves than non-stabilized cavity. This can be explained by the fact that the coupling admittance of each cell gets close to zero and as a consequence, the propagation of tuning errors along the cavity reduces. However, the stabilization does not eliminate tuning errors of the individual cells and they translate into an error in the axial field amplitude of that cell.

This field error can be compensated by an individual adjustment of slug tuners. At the same time, slug tuners need to tune the cavity to the operating frequency ω_{op}. As the effect of tuners on the axial electric field of individual cells and the resonance frequency of DTL are linearly independent of each other, they can be superposed, and the optimum tuner lengths are found as the solution to a constrained linear least squares problem.

Assume that DTL tank contains a total N_T tuners and a total N gaps. The indices i and j refer to tuner setup number and gap number. The vectors $\mathrm{t}_i^{ini} = [\mathrm{t}_1^{ini}, \mathrm{t}_2^{ini} \cdots \mathrm{t}_{N_T}^{ini}]$ and $\mathrm{E}_j^{ini} = [\mathrm{E}_1^{ini}, \mathrm{E}_2^{ini}, \cdots \mathrm{E}_N^{ini}]$ represent the initial lengths of tuners and the axial field corresponding to the initial tuner setup, respectively. The initial set of tuners is adjusted so that all tuners have identical length and the cavity resonates at ω_{op}. Then the tuning process starts with moving all tuner a few millimeters out with respect to the initial tuner length. Consequently, the frequency shifts slightly about $\Delta\omega$. Afterward, the i^{th} tuner is moved in by amount d_i with respect to the other tuners so that the frequency returns to ω_{op}. By considering $\mathrm{E}_{i,j}^{f}$ as the axial field of new configuration of tuners and using the approximation of linear relationship between axial field of j^{th} gap and i^{th} tuner length, the tuner sensitivity is defined

$$\mathrm{T}_{i,j} = \frac{E_{i,j}^{f} - E_j^{ini}}{d^i} \qquad i = 1 \text{ to } N,\ j = 1 \text{ to } N_T.$$

Then the i^{th} tuner is returned to its initial length and the sensitivity of axial fields with respect to the other tuners are measured using the same procedure.

Having the tuner sensitivity matrix T, it is possible to calculate the electric field variation in j^{th} gap for any arbitrary configuration of tuner length t.

$$\mathrm{T} \cdot \mathrm{t} = \Delta \mathrm{E}. \tag{6.2}$$

Since the flat axial field is of interest, one should find a proper tuner configuration of t so that $\Delta\mathrm{E} = 1 - \mathrm{E}^{\text{ini}}$. Therefore the best tuner set t_{best} is

$$\mathrm{T} \cdot \mathrm{t}_{\text{best}} = 1 - \mathrm{E}^{\text{ini}}, \tag{6.3}$$

The best set of tuner can be found using the algebraic solution

$$\mathrm{t_{best}} = [\mathrm{T^T} \cdot \mathrm{T}]^{-1} \cdot \mathrm{T^T} \cdot [1 - \mathrm{E^{ini}}]. \tag{6.4}$$

The best algebraic solution not always has physical meaning. This is due to the fact that some of these tuners are out of allowed range, i.e., they exceed the distance between drift tube and the cylindrical wall. Instead, one can generate a lot of random tuner configurations and calculate the average axial field of each tuner configuration using equation 6.2.

In the following, the results of tuning of DTL Tank1, Tank2 and Tank3 are discussed. For all cavities, the field flatness must be within ±2 % as required by beam physics [80], and the resonant frequency is set to 352.08 MHz in the air.

The initial non-stabilized axial field of Tank1 without tuners is plotted in Fig. 6.15. After assembly, initial axial field measurements show field flatness of around ±6% and resonance frequency shift of around -1 MHz with respect to the design one. The cavity is equipped with 12 slug tuners to adjust the field flatness and the resonance frequency.

The final tuner length distribution of Tank1 is plotted in Fig. 6.14. It is seen that tuners around the power coupler (tuners 5, 6 and 8) are longer than other tuners and consequently they provide more compensation. Among these three tuners, the tuner number 6 is located above the power coupler. In order to prevent tuner 6 to set too close to drift tube, the post-coupler number 7, which is longitudinally approximately at the same place as Tuner 6, has been modified with a thicker copper cylinder with 50 mm extra length and a tuner diameter. The final axial field of tuned and stabilized Tank1 has been plotted in Fig. 6.15 and it is seen that field flatness is reduced to ±1.3%.

The initial axial fields of Tank2 without stabilization and tuning is also plotted in Fig. 6.15. The initial field flatness is around ±10%. Like Tank1, the power couplers perturb fields strongly and as consequence two peaks are seen in the axial field around gap number 13 and 33 which correspond to the position of power couplers of Tank2. After tuning, the field flatness is ±1.5%. Similarly, the strong perturbations are seen in Tank3 and the initial field flatness is ±13%. By adjustment of tuners and post-couplers as shown in Fig. 6.16, the field flatness reduces down to the ±1.0%.

Let us assume that the tuner sensitivity matrix T and initial average axial field E^{ini} are measured. Then for a tuner configuration of t, the final average axial field E^f can be calculated using $E^f = T \cdot t + E^{ini}$. In order to tune a DTL cavity, one can generate different random tuner configuration using a computer code and calculate the

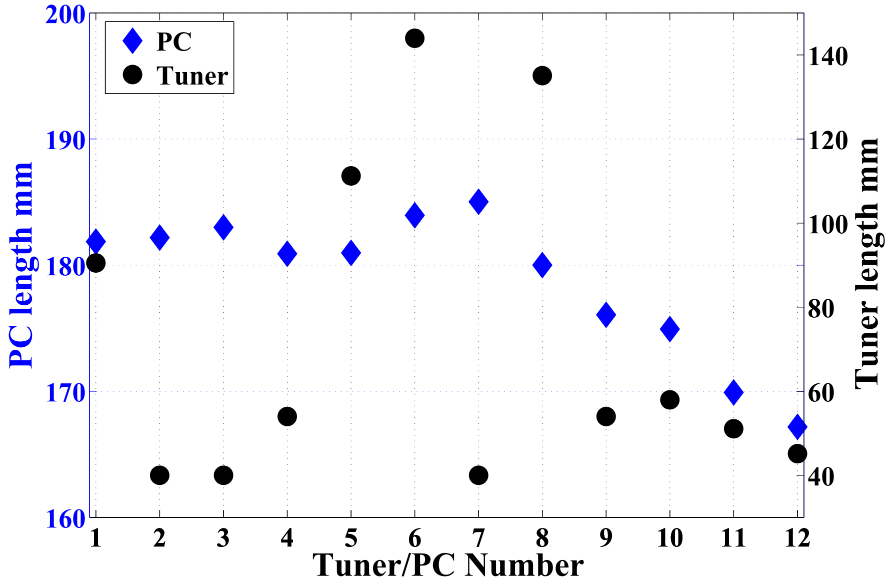

Figure 6.14: The final tuner and post-coupler length distribution of Tank1

field flatness of these configurations. Finally, the tuner configuration with lesser field flatness value is chosen. The advantage of this tuner superposition calculation is that the design parameters are constrained by the tuner range given by the user and this allows limiting the design variable space, fixing lengths for some pre-manufactured pieces. Also, the variation of field flatness when movable tuners are moved can be approximated. The measured and calculated axial field of Tank 1, Tank 2 and Tank 3 is plotted in Fig. 6.17. As is shown in the graphs (Fig. 6.16), the superposition of individual tuner effects, comes very close to the final field measurement and proves the tuning technique. This shows that the assumption of a linear effect of tuners on axial fields is acceptable provided that the TS does not change. After setting all tuners to the calculated values, one can try small changes in the length of some tuners experimentally to search for even flatter field.

6.3.1 Movable tuners

The movable tuners are used to maintain the resonance frequency of a DTL cavity at the operation frequency. In Linac4 DTLs, two tuners are considered as movable tuners. The movable tuner has same radius as fixed tuners but they can be shortened or lengthened during the operation. The frequency shift is approximately about 1 kHz per 1 mm change in the length of a movable tuner.

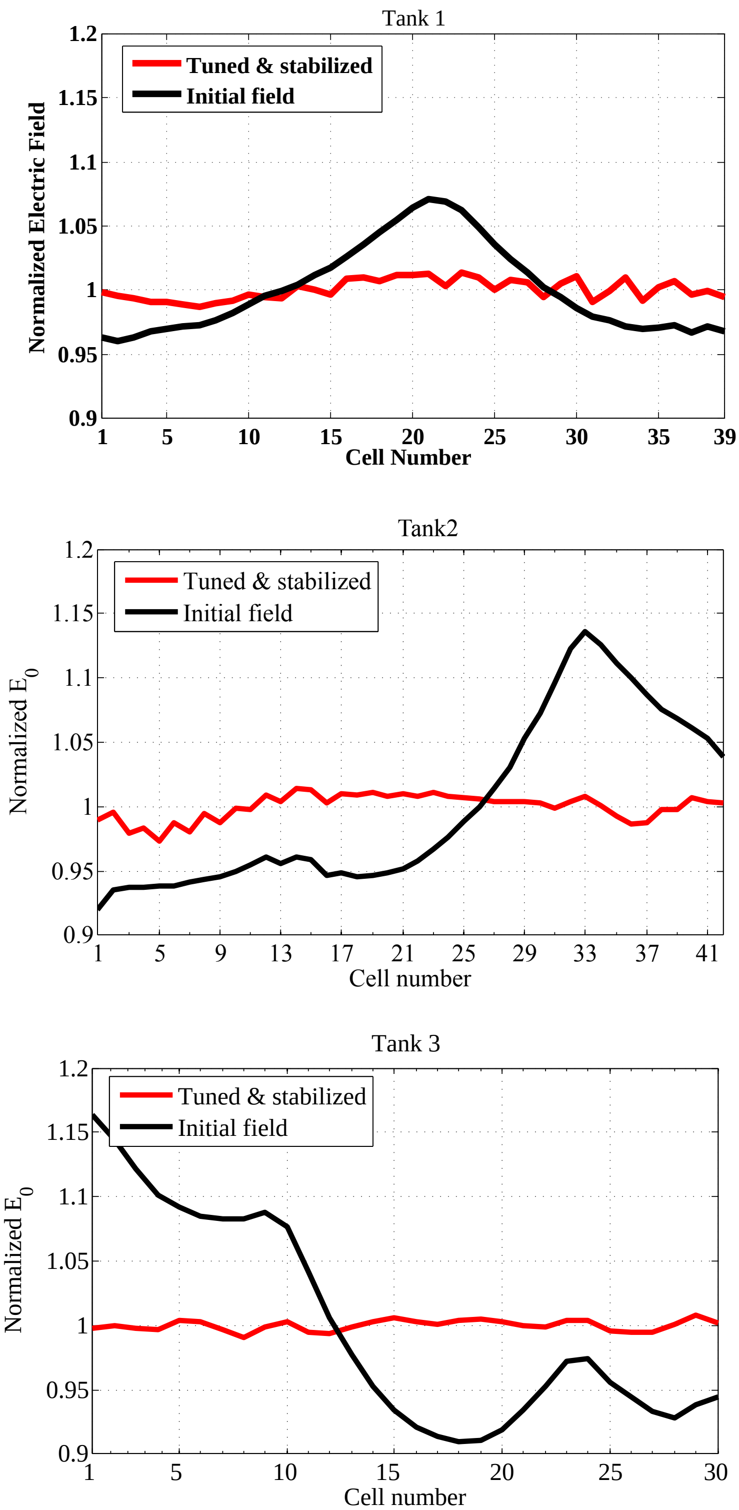

Figure 6.15: The initial axial fields of Tank1, Tank2 and Tank3 Black) Without stabilization and tuning. Red) Tuned and stabilized structure.

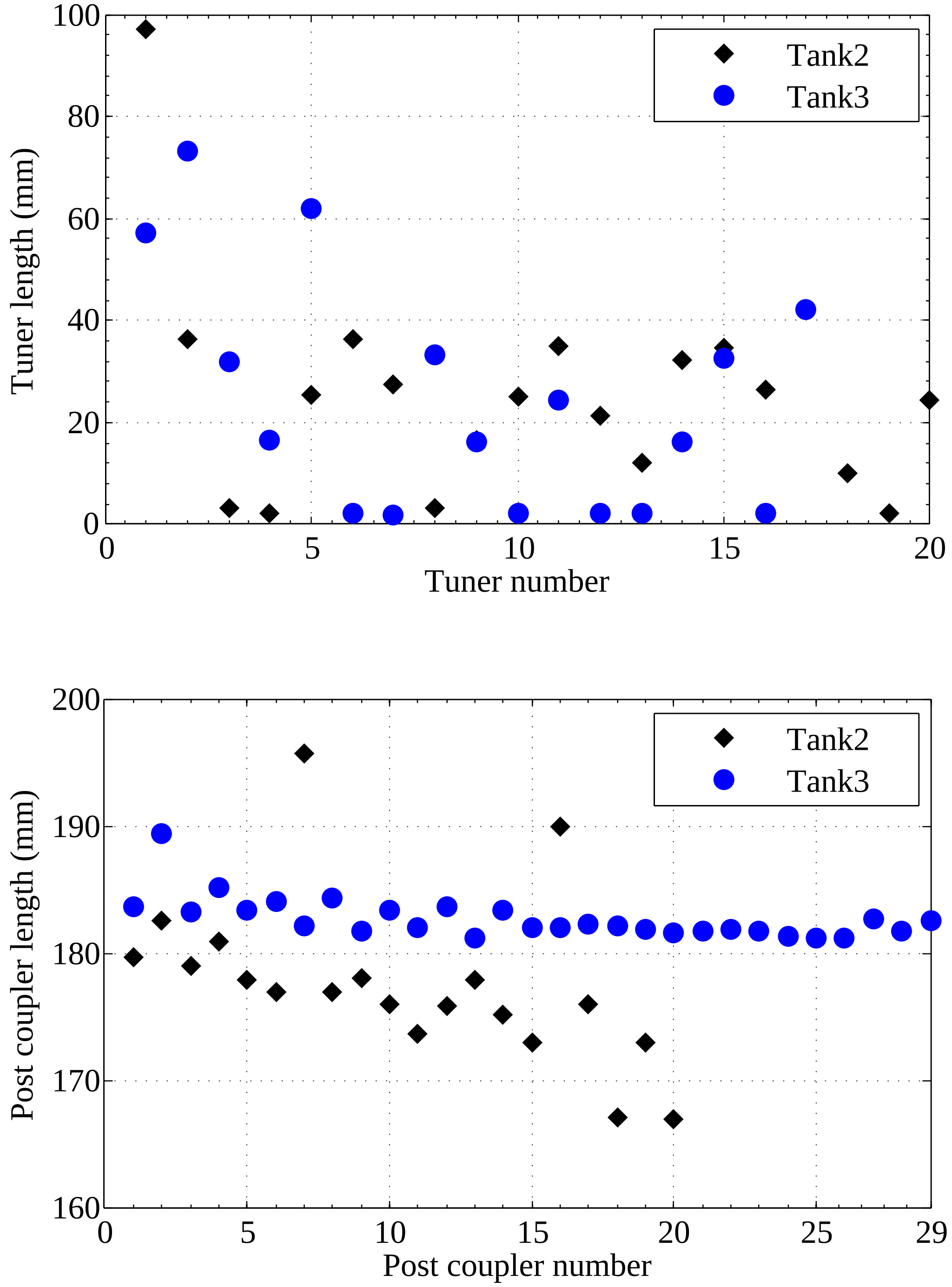

Figure 6.16: Final post-coupler and tuner lengths of Tank 2 and Tank 3

In the DTL Tank1, the tuner number 4 and 9 are the movable tuners. By changing the length of movable tuners from 0 to 50 mm, the field flatness changes between

$\pm1.23\%$ and $\pm1.5\%$. The tuner 5 and tuner 16 are the movable tuners of Tank2. The field flatness for the tuner length between 0 and 35 mm are in range of $[\pm1.8, \pm2.0]\%$ and between 35 mm and 50 mm, the field flatness are between $\pm2.0\%$ and $\pm2.5\%$. Note that the best algebraic field flatness (equation 6.4) for the DTL Tank2 is about $\pm1.5\%$. In the DTL Tank3, the tuner number 4 and 14 are the movable tuners. By changing the length of movable tuners from 0 to 50 mm, the field flatness changes between $\pm0.75\%$ and $\pm1.0\%$.

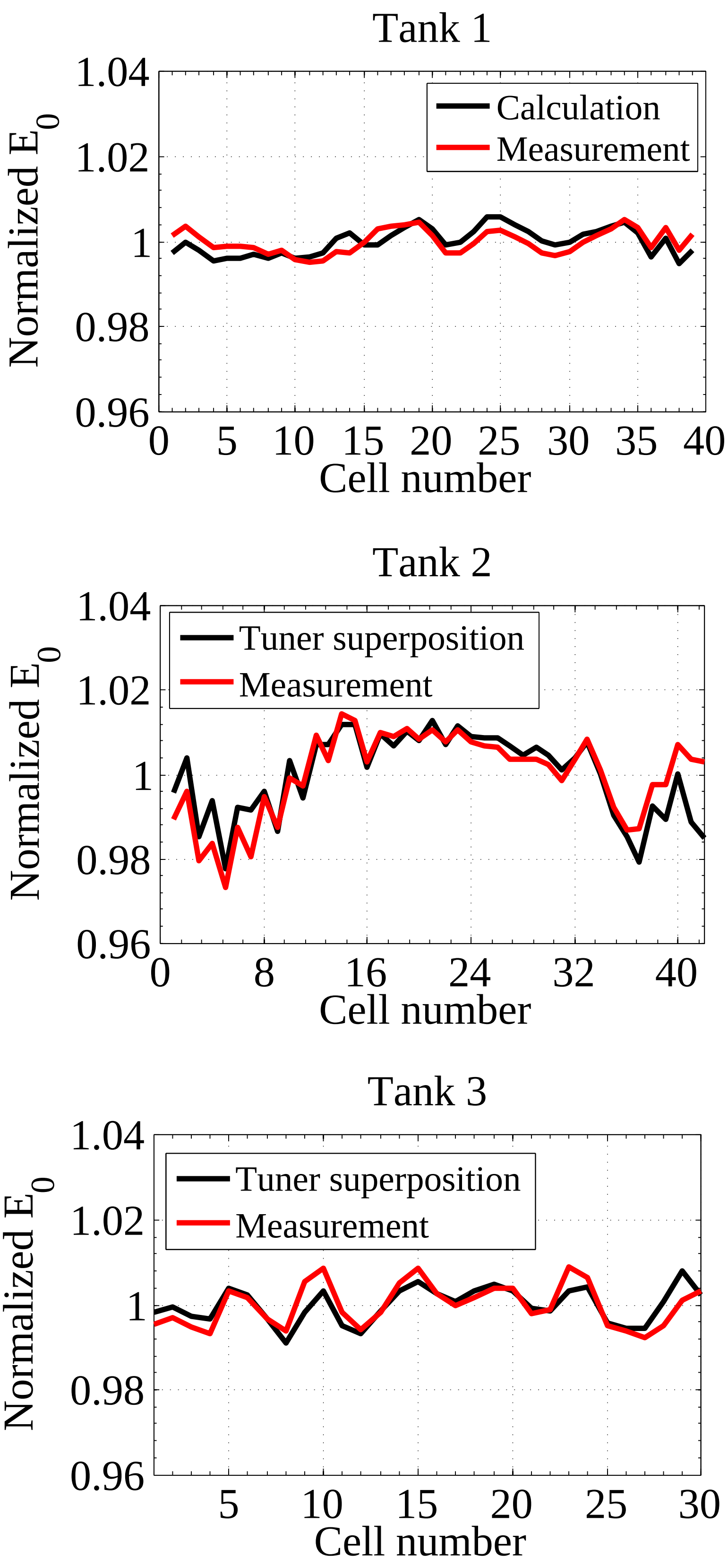

Figure 6.17: The comparison of the measured and calculated axial field of Tank 1, Tank 2 and Tank 3.

Chapter 7

Conclusion

This thesis had discussed the stabilization strategy of DTL cavities. In this chapter, the results that obtained and illustrated in previous chapters are summarized.

For stabilization of a DTL cavity, the electric field distribution along the axis need to be measured. The bead-pull measurements technique is used to measure the electric field distribution. The errors on bead-pull measurements system are studied. Also, details of upgrade that performed on the bead-pull measurement system of Linac4 DTLs have been discussed.

An equivalent circuit model has been used to study the behavior of axial fields in DTL cavities. In the present thesis, to calculate axial electric field of the higher order modes of a DTL structures, a generalized eigensystem is derived and the results have been compared with simulations. The effect of increasing cell length and mutual inductance between cells have been taken into the account in the calculations. Then, the effect of perturbation on axial field of DTL cavities and the TS measurement technique in a DTL have been discussed. Also the modification of traditional TS measurements technique have been discussed. The multiplestems and post-couplers are the common devices to stabilize the DTL structure. The principle of working of these stabilizer devices have been discussed by using circuit model and recent attempts on DTL stabilization by post-coupler have been reviewed.

A straightforward and accurate technique for the stabilization and tuning of DTL tanks has been presented. The criterion of local tilt-sensitivity slope is established as the principal measure for stabilization and it is shown to be proportional to the coupling admittance. The behavior of the local tilt-sensitivity slope is analyzed by 3D HFSS simulations and structure measurements and as an outcome the procedure for tank stabilization is derived. The technique is considerably faster than the tedious iteration approach that has so far been applied to DTL stabilization in that it requires essentially only 4 tilt-sensitivity measurements independent of the structure length, and it provides accurate results. The tuning procedure of CERN's Linac4 DTL structures Tank1, Tank 2 and Tank 3 has been demonstrated.

Appendix A

The Bead pull measurement bench

In the following, the bead-pull measurment bench is discussed. This measurement system is devolped for Linac4 DTLs. The measurement system contains an Agilent E5070A vector network analyser, a DC motor equiped with a encoder, humid and temprature sensors.

In order to automatize the measurement system, to control motor, to pull the bead with a constant velocity, acquire measurement results and the post-processing of the results, I develop a lab-View [81] computer interface. The screenshot of this program is brought in Fig. A.1. The first tab of the program is devoted to ordinary measurement such as S-parameter and phase variation as a function of frequency. In order to perform BM, the phase shift should be measured as a function of time. In our case, a sampling time of 8 ms is of interest, hence, the bead traverses the cavity in about 4 minutes, around 30k phase shift should be recorded. The maximum row of data that can be recorded by built-in function of this version of VNA is limited to maximum 1600 points. Therefore, the second tab of code is dedicated to a routine that measures phase shift without any limitation. In this tab, it is also possible to adjust different parameters such as IF-BW, sampling time, motor speed, power and averaging factor in this tab. The motor is equipped with an encoder to control motor speed smoothly.

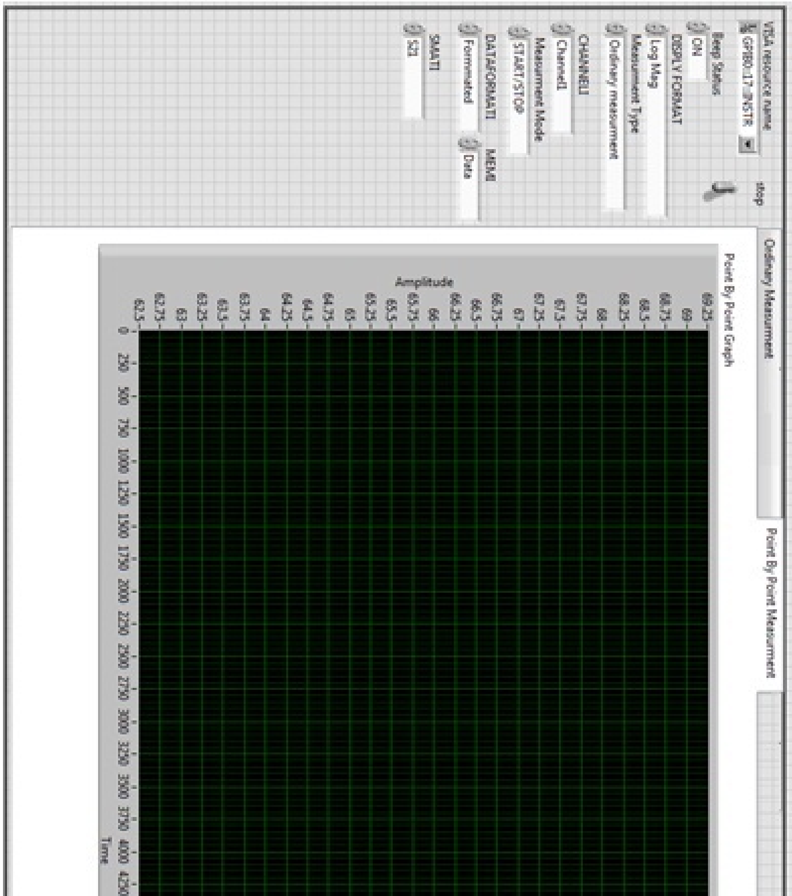

Figure A.1: The screen-shot of Lab-View interface for bead pull measurements.

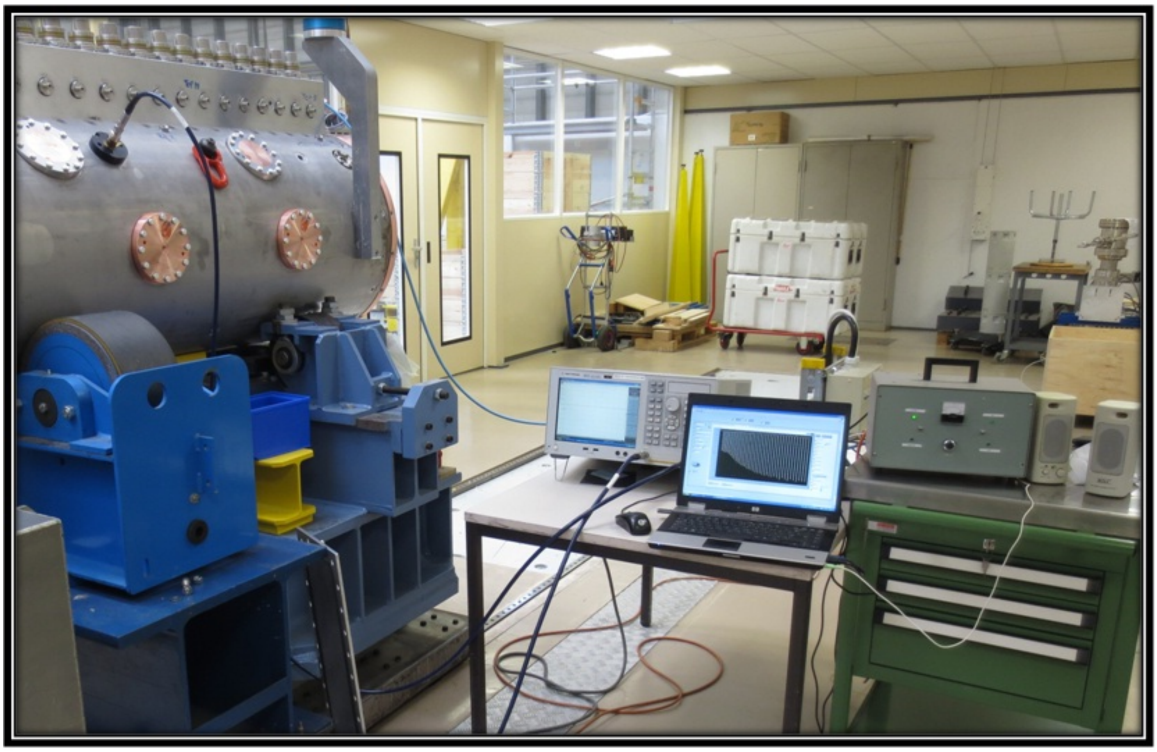

Figure A.2: The bead pull measurements setup at the DTL workshop.

Bibliography

[1] PJ Bryant. A brief history and review of accelerators. 1991.

[2] Luis W Alvarez. *Discovering Alvarez: Selected Works of Luis W. Alvarez with Commentary by His Students and Colleagues*. University of Chicago Press, 1987.

[3] Pierre M Lapostolle. *Proton linear accelerators: a theoretical and historical introduction*. Los Alamos National Laboratory, 1989.

[4] Thomas P. Wangler. *RF Linear Accelerators*. Wiley-VCH, second edition, 2008.

[5] Patrick Petitjean, Vladimir Zharov, Gisbert Glaser, Jacques Richardson, Bruno de Padirac, and Gail Archibald. Sixty years of science at unesco, 1945-2005. *Sixty Years of Science at UNESCO, 1945-2005*, 2006.

[6] Andreas Pritzker. *The Swiss Institute for Nuclear Research SIN*. BoD-Books on Demand, 2014.

[7] Günther Plass. The cern proton synchrotron: 50 years of reliable operation and continued development. In *From the PS to the LHC-50 Years of Nobel Memories in High-Energy Physics*, pages 29–47. Springer, 2012.

[8] Thomas Massam, Th Muller, B Righini, M Schneegans, and Antonino Zichichi. Experimental observation of antideuteron production. *Il Nuovo Cimento A (1965-1970)*, 63(1):10–14, 1965.

[9] Arun Agarwal. *Nobel Prize Winners in Physics*. APH Publishing, 2008.

[10] K Hubner and TM Taylor. The birth and development of the first hadron collider the CERN intersecting storage rings (ISR). Technical report, 2013.

[11] BG Sidharth. *A Century of Ideas: Perspectives from Leading Scientists of the 20th Century. Fundamental Theories of Physics*. Springer, 2008.

[12] Tore Frèangsmyr and A Gösta Ekspong. *Physics: 1981-1990*, volume 6. World Scientific Publishing Company Incorporated, 1993.

[13] Jim Breithaupt. New understanding physics for advanced level. *Physics Education*, 35(5):368, 2000.

[14] John Krige. *History of CERN, III.* Elsevier, 1996.

[15] http://home.cern/about/accelerators/large-electron-positron-collider.

[16] R Garoby. Upgrade issues for the cern accelerator complex. Technical report, 2008.

[17] L Arnaudon, M Magistris, M Paoluzzi, M Hori, D Küchler, P Bourquin, K Hanke, R Wegner, C Rossi, G Bellodi, et al. Linac4 technical design report. Technical report, 2006.

[18] Werner Herr and Bruno Muratori. Concept of luminosity. 2006.

[19] Francesco Grespan. *Study of DTL stabilization with post couplers for the SPES driver LINAC*. PhD thesis, Milan U., 2009.

[20] AM Lombardi, G Bellodi, M Eshraqi, F Gerigk, JB Lallement, S Lanzone, E Sargsyan, R Duperrier, and D Uriot. Beam dynamics in linac4 at cern. *HB2008 Proceedings, Nashville, USA*, 2008.

[21] F Gerigk and R Wegner. Design of the pi-mode structure (pims) for linac4. Technical report, 2009.

[22] D Küchler, R Scrivens, J Peters, and Th Meinschad. 'a RF driven H-source for Linac4. Technical report, 2007.

[23] LM Hein, AM Lombardi, P Posocco, R Scrivens, O Midttun, JB Lallement, and G Bellodi. Linac4 low energy beam measurements. In *Conf. Proc.*, volume 1205201, page THPPP048, 2012.

[24] C Rossi, P Bourquin, JB Lallement, AM Lombardi, S Mathot, M Timmins, G Vandoni, M Vretenar, Switzerland S Cazaux, O Delferriere, et al. The radiofrequency quadrupole accelerator for the linac4. *Linac08, Victoria BC, Canada*, 2008.

[25] M Vretenar, Y Cuvet, G De Michele, F Gerigk, M Pasini, S Ramberger, R Wegner, E Kenjebulatov, A Kryuchkov, E Rotov, et al. Development of a cell-coupled drift tube linac (ccdtl) for linac4. In *this Conference*, 2008.

[26] P Bourquin, R De Morais Amaral, G Favre, F Gerigk, JM Lacroix, T Tardy, M Vretenar, and R Wegner. Development status of the pi-mode accelerating structure (pims) for linac4. *Proc. of Linac2008*, 941, 2008.

[27] F Gerigk, B Riffaud, P Ugena Tirado, S Mathot, M Vretenar, D Pugnat, P Bourquin, G Favre, R Wegner, M Polini, et al. The hot prototype of the pi-mode structure for linac4. Technical report, 2010.

[28] EV Kozyrev. Standing-wave structures. *Frontiers of Accelerator technology*, page 339, 1999.

[29] DH Whittum. Introduction to microwave linacs. In *Techniques and Concepts of High Energy Physics X*, pages 387–486. Springer, 1999.

[30] Frank L Krawczyk, James H Billen, Robert D Ryne, Harunori Takeda, and Lloyd M Young. The los alamos accelerator code group. In *Particle Accelerator Conference, 1995., Proceedings of the 1995*, volume 4, pages 2306–2308. IEEE, 1995.

[31] C Plostinar. Comparative assessment of hippi normal conducting structures. *CARE-Report-2008-071-HIPPI*.

[32] TP Wangler and KR Crandall. Beam halo in proton linac beams. In *Linac 2000 Conference Proceedings, Monterey California*, 2000.

[33] David M Pozar. Microwave engineering 3e, 2005.

[34] Thomas P Wangler. *RF Linear accelerators*. John Wiley & Sons, 2008.

[35] John David Jackson and John D Jackson. *Classical electrodynamics*, volume 3. Wiley New York etc., 1962.

[36] Richard Becker and Fritz Sauter. *Electromagnetic fields and interactions*, volume 1. Courier Corporation, 1964.

[37] Venceslav F Kroupa. *Phase lock loops and frequency synthesis*. John Wiley & Sons, 2003.

[38] Janine Love. *RF Front-End: World Class Designs: World Class Designs*. Newnes, 2009.

[39] Daniel M Dobkin. *RF engineering for wireless networks: hardware, antennas, and propagation*. Newnes, 2011.

[40] TG Jurgens. Equations for bead pull cavity measurements lu-159. *Fermilab-LU-159*, 1990.

[41] Ursula Van Rienen. *Numerical methods in computational electrodynamics: linear systems in practical applications*, volume 12. Springer Science & Business Media, 2012.

[42] R Ainsworth, G Boorman, A Lyapin, S Molloy, Lund AB, Sweden A Garbayo, Eibar AVS, and P Savage. Bead-pull test bench for studying accelerating structures at rhul.

[43] S Ghosh, Sudeshna Seth, Aditya Mandal, and SS Som. Bead-pull measurement using phase-shift technique in multi-cell elliptical cavity. In *Conf. Proc.*, volume 110904, pages 280–282, 2011.

[44] Samy Hanna. *RF linear accelerators for medical and industrial applications*. Artech House.

[45] Jiaru Shi, Alexej Grudiev, and Walter Wuensch. Tuning of x-band traveling-wave accelerating structures. *Nuclear Instruments and Methods in Physics Research Section A: Accelerators, Spectrometers, Detectors and Associated Equipment*, 704:14–18, 2013.

[46] KA Bakshi AV Bakshi UA Bakshi. *Electrical Measurements & Measuring Instruments*. Technical Publications, 2007.

[47] Semyon G Rabinovich. *Measurement errors and uncertainties: theory and practice*. Springer Science & Business Media, 2006.

[48] Margo Hunt, A Mayio, M Brossman, and A Markowitz. The volunteer monitors guide to quality assurance project plans. *US Environmental Protection Agency, Office of Wetlands, Oceans, and Watersheds*, 1996.

[49] Michael Hiebel. Vector network analyzer (VNA) calibration: the basics. *White Paper*, 2008.

[50] Understanding VNA Calibration.

[51] National Instrument. Fundamentals of network analysis.

[52] AN Agilent. 1287-3 applying error correction to network analyzer measurements. *Agilent Technologies, USA*, 2002.

[53] C. G. Montgomery. *Technique of Microwave Measurement*, volume 11. McGraw-Hill, New York, 1947.

[54] LH Ford. The effect of humidity on the calibration of precision air capacitors. *Journal of the Institution of Electrical Engineers-Part II: Power Engineering*, 95(48):709–712, 1948.

[55] D. Bryant. *Engineering Transmission Lines with High Capacity Low Sag ACCC Conductor: ACCC Conductor*. CTC Global Corporation, 2011.

[56] Alen Hatibovic. Derivation of equations for conductor and sag curves of an overhead line based on a given Catenary constant. *Electrical Engineering and Computer Science*, 58(1):23–27, 2014.

[57] James H Billen and Alan H Shapiro. Post coupler stabilization and tuning of a ramped gradient drift tube linac. *CELL*, 7:6, 1989.

[58] John R Reitz, Frederick J Milford, and Robert W Christy. *Foundations of electromagnetic theory*. Addison-Wesley Publishing Company, 2008.

[59] F Grespan, G De Michele, F Gerigk, S Ramberger, et al. The Linac4 DTL prototype: Theoretical model, simulations and low power measurements. 2009.

[60] CY Tan, JS Schmidt, and A Schempp. Simple lumped circuit model applied to field flatness tuning of four-rod radio frequency quadrupoles. *Physical Review Special Topics-Accelerators and Beams*, 17(1):012002, 2014.

[61] Robert E Collin. *Field theory of guided waves*. Wiley-IEEE Press, 1991.

[62] EA Knapp, BC Knapp, and JM Potter. Standing wave high energy linear accelerator structures. *Review of Scientific Instruments*, 39(7):979–991, 1968.

[63] Thomas P. Wangler. *RF linear accelerators*. 2008.

[64] D. Carter. Field Stabilization in Periodic Systems. *eConf*, C680520:579, 1968.

[65] T Nishikawa. Equivalent circuit and dispersion relation for the multistem drift tube structure. 1966.

[66] D. A. Swenson, E. A. Kaapp, J. M. Potter, and E. J. Schneider. Stabilization Of The Drift Tube Linac By Operation In The $\pi/2$ Cavity Mode. In *Proceedings, 6th International Conference on High-Energy Accelerators, HEACC 1967*, pages 167–173, 1967.

[67] S. Giordano. Measurements on the multistem drift tube structure for proton accelerators. 1966.

[68] P.M. Lapostolle and A.L. Septier. *Linear Accelerators. Edited by Pierre M. Lapostolle (And) Albert L. Septier*. 1970.

[69] F NAITO. A tuning method of post couplers for a low β drift tube linac. *Particle Accelerators*, 32:27–32, 1990.

[70] T. Kato S. Machida and S. Fukumoto. Stabilizing characteristics of post-couplers. *IEEE Trans. Nucl. Sci.*, NS-32(5), 1985.

[71] Jens Peters. Rf-tuning of the HERA linac 3 alvarez structures. 1989.

[72] S.O. Schriber J. Ungrin and A.A. Vokes. post-coupler and stem current measurements for high current CW drift-tube linacs. *IEEE Trans. Nucl. Sci.*, NS-30(4), 1983.

[73] Masaru Sawamura and Hidekuni Takekoshi. Field stabilization of the alvarez linac by post coupler. 1985.

[74] MR Khalvati and S Ramberger. Tuning and field stabilization of the CERN Linac4 drift tube linac.

[75] F. Grespan. Equivalent circuit for postcoupler stabilization in a drift tube linac. *Phys. Rev. ST AB*, 12, 2012.

[76] http://www.ansys.com/products/electronics/ansys-hfss.

[77] S. Ramberger et al. CERN Linac4 drift tube linac manufacturing and assembly. In *Proc. of Linac14*, 2014.

[78] S Ramberger, P Bourquin, Y Cuvet, A Dallocchio, G De Michele, F Gerigk, J M Giguet, J B Lallement, A M Lombardi, E Sargsyan, and M Vretenar. Production Design of the Drift Tube Linac for the CERN Linac4. In *Proceedings, 25th International Linear Accelerator Conference, LINAC2010*, 2011.

[79] Alex Chao and Maury Tigner. *Handbook of Accelerator Physics and Engineering.* Word Scientific, third edition, 2006.

[80] G. Bellodi, et al. Alignment and field error tolerance in linac4. *CERN-ATS-Note-2011-021*, 2011.

[81] http://www.ni.com/labview.